Exploration of the Potential of Civil Unmanned Aerial Vehicles Powered by Micro Gas Turbine Propulsion System

Master Thesis

S.M.L. Beuselinck

Delft University of Technology

TU Delft

Challenge the Future

Delft University of Technology

Exploration of the Potential of Civil Unmanned Aerial Vehicles Powered by Micro Gas Turbine Propulsion System

Master Thesis

By

S.M.L. Beuselinck

In partial fulfilment of the requirements for the degree of

Master of Science
in Aerospace Engineering

at the Faculty of Aerospace Engineering,
of the Delft University of Technology,

Kluyverweg 1
2629HS Delft
The Netherlands

Supervisors:	Prof. dr. ir. P. Colonna
	Dr. ir. M. Voskuijl
	Ir. W.P.J. Visser

This thesis is confidential and cannot be made public until May 13, 2015.

An electronic version of this thesis is available at http://repository.tudelft.nl/.
Thesis Registration Number: 029#15#MT#FPP

TU Delft Delft University of Technology

DELFT UNIVERSITY OF TECHNOLOGY
DEPARTMENT OF
FLIGHT PERFORMANCE AND PROPULSION

The undersigned hereby certify that they have read and recommend to the Faculty of Aerospace Engineering of the Delft University of Technology for acceptance a Master thesis entitled "**Exploration of the Potential of Civil Unmanned Aerial vehicles Powered by Micro Gas Turbine Propulsion System**" by **S.L.M. Beuselinck** in partial fulfilment of the requirements for the degree of **Master of Science in Aerospace Engineering**.

Date: May 13, 2015

Head of department: ______________________
Prof. dr. ir. P. Colonna

Supervisor: ______________________
Dr. ir. M. Voskuijl

Supervisor: ______________________
Ir. W.P.J. Visser

Reader: ______________________
Dr. R. Pecnik

Executive Summary

Civil Unmanned Aerial Vehicles (UAVs) are outnumbered compared to the military equivalents. They could however be of great value to various organizations, companies and the general public. They currently seem to be on the verge of a breakthrough. An interesting technology that could help increase the flight performance of civil UAVs is the micro gas turbine technology. This is a promising propulsion system that is being developed at the moment. It could become a solid competitor for other propulsion systems used to power UAVs due to the higher power-to-weight ratio, lower complexity, higher energy density potential and power density advantage. This could fuel the continuous expansion of civil UAVs even more. The objective of this Master thesis is to investigate the difference in flight performance between a UAV powered by a reciprocating engine and a micro gas turbine; to explore the potential of a UAV powered by a micro gas turbine based propulsion system.

The exploration study first identifies the most promising application. Followed by nominating an existing UAV design as a baseline, based on the closest requirement match with the selected application. The Harfang EADS, powered by a Rotax 914 turbocharged reciprocating engine, acts as the baseline UAV. The flight performance of this UAV is determined by a software package in which point performance is integrated to obtain path performance of a typical mission profile. The aerodynamic model of the baseline UAV is determined using a combination of a vortex lattice method and the thin plate approximation. Weight estimation relationships are used to determine the components weight and the center of gravity location. Fuel flow and thrust data of the reciprocating engine are derived from the operating manual of the Rotax 914 engine, while thrust management tables from another Master thesis are used to model different micro gas turbine sizes (86, 70 and 60 kW), each having a number of technology levels. The influence of some of the assumed parameters is investigated by a sensitivity analysis. Minor modifications to the UAV dimensions resulted in a none notable effect on the mission performance of the baseline UAV. Increasing the critical Reynolds number on the other hand had a significant effect on the drag coefficient, while the influence of the Oswald factor on the drag coefficient gradually increased as function of the angle of attack. Changes to the drag coefficient and user-specified propeller propulsion efficiency of the baseline UAV both had limited effect on the mission performance. Modifications to the specific fuel consumption of the reciprocating engine resulted in a more pronounced effect.

The research indicates an increase in mission endurance of 4% for the 60 kW micro gas turbine with the highest technology level compared to the reciprocating engine using the same UAV platform. A take-off weight reduction of 18% can be obtained if the UAV platform is optimized for this micro gas turbine by a redesign process; modifying the wing, fuselage and empennage design. The fuel weight is reduced by 12.5% compared to the reciprocating engine as a result of the increased mission endurance and redesign process. The micro gas turbine can therefore perform the same mission as the reciprocating engine with less fuel. This Master thesis therefore concluded that there is a performance gain possible if a reciprocating engine is replaced by a micro gas turbine. This performance gain could also be transformed into a fuel weight reduction, proving the potential of civil UAVs powered by a micro gas turbine based propulsion system.

Acknowledgements

I would like to express my gratitude towards my supervisors Mark Voskuijl, Wilfried Visser and Piero Colonna for their guidance, advice and contributions towards this Master thesis. I would also like to thank Rene Pecnik for being part of the examination committee, taking the time to asses my thesis work.

Thanks to Anna Marcellan with whom I worked with during this Master thesis. It was a very pleasant experience to exchange knowledge with her and discuss both work-related and off-topic subjects.

I am grateful for all the friends I made at the faculty of Aerospace Engineering. I would not have made it this far without you. Finally, many thanks go to my parents and family for always supporting my efforts and believing in me.

Sander Beuselinck
Delft, May 2015

Table of Contents

Nomenclature

Roman Symbols

Symbol	Unit	Definition
#	$-$	Number
h	m	Height
A, B	$-$	Flap coefficient
AR	$-$	Aspect ratio
C	$-$	Dimensionless coefficient
F	$-$	Factor
FF	$-$	Form factor
J	$-$	Advance ratio
K	$-$	Constant
M	$-$	Mach number
N	N	Normal weight
P	W	Power
Q	$-$	Interference factor
R	m	Radius
RC	m/s	Rate of climb
RD	m/s	Rate of descent
Re	$-$	Reynolds number
S	m^2	Area
T	N	Thrust
V	m/s	Velocity
W	N	Weight
X	$-$	Cartesian X coordinate
Y	$-$	Cartesian Y coordinate
Z	$-$	Cartesian Z coordinate
a, c	$-$	Constant used to determine fuselage length
b	m	Span
c	m	Chord length
d	m	Diameter
d	$-$	Derivative
e	$-$	Oswald factor
g	m/s^2	Gravitational constant
k	$-$	Induced drag factor
l	m	Length
$\dot{m}$	kg/s	Fuel flow
n	$-$	Load factor
n	$1/s$	Rotation speed
q	Pa	Dynamic pressure
s	m	Distance
t	m	Thickness
t	s	Time
w	m	Width

Greek Symbols

Symbol	Unit	Definition
$\dot{\chi}$	$°/s$	Rate of turn
Γ	m^2/s	Vortex
Δ	$Variable$	Difference
Λ	$°$	Sweep angle
Φ	$°$	Bank angle
α	$°$	Angle of attack
γ	$°$	Flight path angle
δ	$°$	Deflection angle
δ	Pa	Relative ambient pressure
η	$-$	Efficiency
θ	$°$	Pitch angle
λ	$-$	Taper ratio
μ	$Pa \cdot s$	Dynamic viscosity
μ	$-$	Friction coefficient
ρ	kg/m^3	Density

Super- and Subscripts

Symbol	Definition
$1/2$	Half chord
0	Zero
0	Freestream
0.25	Quarter chord
5	Flap deflection angle of 5°
20	Flap deflection angle of 20°
AF	Airframe
$Avion$	Avionics
$Cant$	Cantilever
CG	Center of gravity
D	Drag
Des	Design dive speed
E	Empty
Emp	Empennage
Eng	Engine
Eq	Equivalent
Fr	Froude
Fus	Fuselage
Fwd	Forward
GE	Ground effect
GR	Ground run
$Guess$	Initial guess
HT	Horizontal tail
L	Lift
LG	Landing gear
LND	Landing
LOF	Lift-off
$Matl$	Materials
MG	Main Gear
Misc	Miscellaneous
NG	Nose Gear
$Press$	Pressure

Symbol	Definition
PL	Payload
$Prop$	Propulsion
R	Rotation
$Struct$	Structure
$Strut$	Landing gear strut
Sys	System
TO	Take-off
Tot	Total
VT	Vertical Tail
$Wheel$	Landing gear wheel
Wet	Wetted
$Wing, W$	Wing
a	Available
b	Span
c	Correction
$comp$	Component
cr	Critical
crz	Cruise
d	Descent
des	Desired
dwf	Delta Wing Factor
eff	Effective
f	Skin friction
g	Ground
i	Induced
j	Jet
kin	Kinetic
lam	Laminar
max	Maximum
mean	Mean aerodynamic chord
min	Minimum
n	Normal
no	None tapered
$prop$	Propeller
r	Root
r	Required
ref	Reference
seg	Segment
$side$	Side
st	Stiffness
st	Static
t	Horizontal tail moment arm
tfo	Trapped oil and fuel
$trans$	Transition
$turb$	Turbulent
uc	Under carriage
ult	Ultimate
v	Vertical tail moment arm
w	Wave
x	Cartesian x-axis
y	Cartesian y-axis
z	Cartesian z-axis

Glossary

A/C	Aircraft
AIAA	American Institute of Aeronautics and Astronautics
AoA	Angle of Attack
APU	Auxiliary Power Unit
C.G.	Center of Gravity
CAS	Calibrated Airspeed
CFD	Computational Fluid Dynamics
DC	District of Colombia
DDD	Dull, Dangerous and Dirty
DoD	Department of Defense
E.O.M.	Equations of Motion
EADS	European Aeronautic Defence and Space Company
EN	Endurance
GA	General Aviation
GPS	Global Positioning System
GSP	Gas Turbine Simulation Program
HALE	High Altitude Long Endurance
IFR	Instrument Flight Rules
ILS	Instrument Landing System
LR	Long Range
MAC	Mean Aerodynamic Chord
MALE	Medium Altitude Medium Endurance
MAV	Micro Unmanned Aerial Vehicle
MGT	Micro Gas Turbine
MIT	Massachusetts Institute of Technology
MR	Medium Range
MTOW	Maximum Take-off Weight
MUAV	Mini Unmanned Aerial Vehicle
NACA	National Advisory Committee for Aeronautics
NLR	National Aerospace Laboratory
OEW	Operative Empty Weight
Pr	Pressure Ratio
Ref	Reference
RPA	Remotely Piloted Aircraft
rpm	Rotations per Minute
RPV	Remotely Piloted Vehicle
RQ	Reconnaissance
SFC	Specific Fuel Consumption
SI	International System of Units
SR	Short Range
TAS	True Airspeed
TIT	Turbine Inlet Temperature
TL	Technology Level
UAS	Unmanned Aerial System
UAV	Unmanned Aerial Vehicle
UCAS	Unmanned Combat Aircraft System
VFR	Visual Flight Rules
VIP	Very Important Person
VLM	Vortex Lattice Method
VTOL	Vertical Take-off and Landing
WER	Weight Estimation Relationships

1 Introduction

For many decades Unmanned Aerial Vehicles (UAVs) only had a niche market in the aviation industry. Recent armed conflicts in the Middle East resulted in an upsurge of military UAVs. They have been used in large numbers during most of those conflicts proving their potential by booking great successes **[1,2,3]**. They gradually went from reconnaissance and surveillance roles to more offensive roles by executing strike missions with high precision. This made them well-known/notorious to the general public. Less familiar to the general public are the civil UAVs, except for the small off-the-shelf low budget drones which only have limited range. These drones often use small electric engines powering multiple rotors and are not categorized as UAVs by the industry **[4]**. Civil UAVs could however be of great value to various organizations, companies and the general public. For example, utility companies could use them to inspect the power and pipelines or they could be deployed for numerous science missions using remote sensing equipment acting as data acquisition platforms. They could even be used by police authorities, firefighting services, coast guards and emergency services to protect the general public. Some authors even suggest that one should only bring a UAV platform to the market and the applications will simply follow **[4]**. The high demand for civil UAVs is stimulated by some clear operating advantages compared to manned aircraft. They not only eliminate pilot risk, but also initiate a potential weight saving. Unfortunately, the large number of possible applications for civil UAVs is in strong contrast with the number of civil UAVs in operation. Numerous reasons are identified and addressed during this research project. An interesting technology that could help increase the flight performance of civil UAVs is the micro gas turbine (MGT) technology. In essence, this technology investigates scaled-down versions of the large gas turbines used to power commercial airliners. This is a promising propulsion system that is being developed at the moment. It could become a solid competitor for other propulsion systems used to power UAVs due to the higher power-to-weight ratio, lower complexity, higher energy density potential and power density advantage. This could fuel the continuous expansion of civil UAVs even more.

The aim of this Master thesis is to explore the potential of civil UAVs using a micro gas turbine based propulsion system by analyzing the flight performance of an existing civil/military UAV and its propulsion system; followed by using the characteristics of this baseline UAV to perform a redesign study. This redesign study optimizes the UAV design for an MGT matching the mission requirements of the selected application. This Master thesis project focuses on the flight performance simulation and UAV platform redesign, while another Master thesis focuses on the MGT technology **[5]**. Both projects interact with each other in order to come up with a feasible design. The Master thesis is therefore answering the following research question:

> *What is the difference in flight performance if the design of an existing UAV is optimized to accommodate an MGT based propulsion system?*

The exploration study gives a state-of-the-art overview of the previous work carried out by academics creating a proper knowledge environment and highlighting the gap in knowledge which this research project helps to solve. A feasible civil UAV application is identified in combination with the necessary mission requirements. An existing UAV powered by a reciprocating engine is selected and modeled through reverse engineering in order to simulate the flight performance. This is compared to the flight performance of the same UAV model powered by an MGT, investigating possible performance gains. This is followed by a redesign phase to optimize the UAV airframe for the MGT, increasing any potential performance gains. The UAV model is verified by comparing the performance characteristics with the actual data of the baseline UAV, while a sensitivity analysis investigates the influence of some of the assumed parameters. The results of the Master thesis could well lead to a new research field within the Flight Performance and Propulsion Section of the Delft University of Technology.

The structure of this report is divided in three parts; an exploration study, a modeling phase and a redesign phase. The exploration study starts with a brief background description of UAVs, see Chapter 2. An overview of the future civil UAV applications is given in Chapter 3. This chapter also identifies the selected applications which have been developed into a case study for the Master thesis. The modeling phase begins with stating the case study definition in Chapter 4. The flight performance simulation which involves a weight breakdown, aerodynamic, propulsion and flight performance analysis is discussed in Chapter 5. The results of the flight performance simulation in combination with the model verification can be found in Chapter 6. A comparison between the reciprocating and MGT mission performance is also discussed in this chapter. This is followed by a sensitivity analysis which examines the influence of some of the assumed parameters, see Chapter 7. The final part of this report discusses the redesign phase, which can be found in Chapter 8. The report is finalized by conclusions in Chapter 9 and some recommendations for future research, see Chapter 10.

Part I - Exploration Study

2
UAV Background

Throughout the years different names have been allocated to a UAV, e.g.: drone, Remotely Piloted Vehicle (RPV), Remotely Piloted Aircraft (RPA) and most recently Unmanned Aerial System (UAS) **[6]**. The later one was introduced to include subsystems such as the ground station and the launch and recovery system. All these different acronyms can however create some confusion if there is no consistency in their use. This report only uses the term UAV to avoid further confusion.

Not only the name changed throughout the years but also the role of a UAV has evolved drastically. This chapter therefore first gives a brief overview of the history of UAVs followed by a definition and classification, see Section 2.1 and 2.2. An overview of the existing UAVs, both military and civil, is given in Section 2.3, while the advantages and disadvantages compared to manned aircraft are addressed in Section 2.4. A discussion of the remaining issues related to the low number of civil UAVs in operation is provided in Section 2.5. Section 2.6 gives the design and configuration options of UAVs. The chapter is finalized by a brief discussion of the different propulsion systems, see Section 2.7.

2.1 History

The history of UAVs begins even before the first powered flight of the Wright brothers. In 1896 Samuel Pierpont Langley launched an unmanned aircraft powered by a steam engine over the Potomac River near Washington DC. His '*Aerodrome No. 5*' flew more than 1 km but did not have an active guidance system **[6]**. This missing element was added in the form of a gyroscope system by Elmer Sperry in 1918 **[6,7]**. During World War I aerial torpedoes and practice targets were being developed but the war ended before these systems could be deployed on the battlefield **[4]**. The interwar period only saw limited development. Great Britain focused further on the development of aerial targets during World War II **[6]**. They were produced in high numbers and used as gunnery practice targets. Meanwhile, Germany was focusing on the design of cruise missiles, of which the '*V1 flying bomb*' was the most notorious one **[6, 7]**. At the end of the war several countries were developing UAVs to measure nuclear radiation, act as assault drones or conduct reconnaissance missions. Optical equipment was used for 'hands-on' guidance. Between the postwar period and 1970, jet powered cruise missiles were further developed but only a few of those systems became operational **[6,7]**. The period between 1970 and 1990 saw a great upsurge in the number of military UAVs **[4]**. The predecessors of the Medium-Altitude Long-Endurance (MALE) and High-Altitude Long-Endurance (HALE) UAVs were developed during this period **[6]**. Their missions were mainly reconnaissance and surveillance missions for the military. During the period between 1990 and 2000 GPS technology, digital electronics and digital data links were mature enough to be used for UAVs **[4,6]**. The United States of America realized the potential of military UAVs during Operation Desert Storm and Iraqi Freedom. Perhaps the most well-known UAVs, the General Atomics Predator A and Northrop Grumman Global Hawk, were also designed between 1990 and 2000. A few civil UAVs were developed during this period as well and were conducting earth monitoring missions related to environmental research. Their usage was however limited. The use of military UAVs increased drastically between 2000 and the present **[6]**. Several UAVs were developed or modified to carry lethal payloads. This meant that the UAV could detect a threat and no longer had to wait for a conventional strike aircraft in order to eliminate the threat. This raised some ethical questions however **[4]**. The use of civil UAVs during this period is still limited compared to military UAVs. Currently military developments are focusing on the so called Unmanned Combat Aircraft System (UCAS) while civil UAVs seem to be on the verge of a breakthrough. **[4,6,7]**

2.2 Definition and Classification

Defining a UAV as an aircraft in which the flight crew has been replaced by a flight computer is just an over-simplification and too short-sighted **[4]**. Several authors and organization have proposed definitions for UAVs, but the most comprehensive one is the definition of the Department of Defense (DoD) of the United States of America. This definition is also the most common one. The DoD defines a UAV as:

> *"A powered, aerial vehicle that does not carry a human operator, uses aerodynamic forces to provide vehicle lift, can fly autonomously or be piloted remotely, can be expendable or recoverable, and can carry a lethal or nonlethal payload"* **[2]**.

The lethal payload has to be excluded from the definition if one wants to define a civil UAV. Airships and rockets or cruise missiles are generally not considered to be a UAV since no aerodynamic forces are used to provide lift. Model aircraft used for recreational activities and the user-friendly off-the-shelf drones have recently experienced an upsurge in use but are also not considered to be a UAV, which is often a misconception under the general public **[4]**. It can sometimes be difficult to distinguish the difference though UAVs generally undergo the same thorough design process as their manned counterparts and are tested extensively; whereas the model aircraft are designed by smaller companies which have less experience and sometimes lack knowledge on aircraft design and proper manufacturing techniques compared to UAV manufactures. Model aircraft also have to remain within sight of the operator which is not always wanted for UAVs. A few authors are taking it even one step further by saying that one can only speak of a UAV if there is to a greater or lesser extent some kind of automatic intelligence **[4]**. The UAV should also be able to communicate with its operator, e.g.: payload information, housekeeping data or video streams should be transmitted to the operator. He or she can then respond to the situation by sending direct control inputs or altering the mission profile.

A similar situation exists if one wants to classify UAVs, since numerous authors also have developed their own classification system. These systems are often based on size and weight going from small hand-launched UAVs weighing a couple of 100 grams to large fixed wing UAVs weighing over 12 tons with a range of 20,000 km **[8,9]**. Apart from the size, the classification can also be based on other factors like the propulsion system, mission or payload; to only name a few. The classification also changes as the technology evolves. It was therefore decided to use one specific classification, making a distinction based on the performance characteristics (altitude, endurance and range) and weight, for the duration of this Master thesis. This classification, defined by De Fátima Bento **[10]**, together with some example UAVs is outlined in Table 2-1. Please note that some overlap exist between the different classes.

Table 2-1: UAV Classification [10]

UAV Class	Altitude [m]	Endurance [hr.]	Range km]	MTOW [kg]	Example
HALE	15,000 - 20,000	24 - 48	> 2,000	2,500 - 12,500	Global Hawk
MALE	5,000 - 15,000	24 - 48	> 500	1,000 - 1,500	Predator
EN (Endurance)	5,000 - 8,000	12 - 24	> 500	500 - 1,500	Shadow II
LR (Long Range)	5,000	6 -13	200 - 500	/	Hunter
MR (Medium Range)	3,000 - 5,000	6 - 10	70 - 200	150 - 500	Eagle Eye+
SR (Short Range)	3,000	3 - 6	30 - 70	200	Firebird
Close-Range	3,000	2 - 4	10 - 30	150	Scan Eagle
MUAV (Mini UAV)	150 - 300	< 2	< 10	< 30	Desert Hawk III,
MAV (Micro Air Vehicle)	250	1	< 10	0.10	Wasp

2.3 Existing UAV Overview

In 2013 a total of 813 UAV designs were identified by the American Institute of Aeronautics and Astronautics (AIAA) **[11]**. The total amount of UAV designs will however be larger since some information is confidential due to military secrecy. Not all 813 UAVs are already flying, some of them are still being developed or tested. Figure 2-1 lists the top 10 of the countries which produce the most UAV designs. It is clear from this figure that the United States of America have the largest number of UAV designs by almost double the amount of China which is the second largest producer. Israel completes the top three; it is however one of the world leaders in UAV developments and technologies **[4]**.

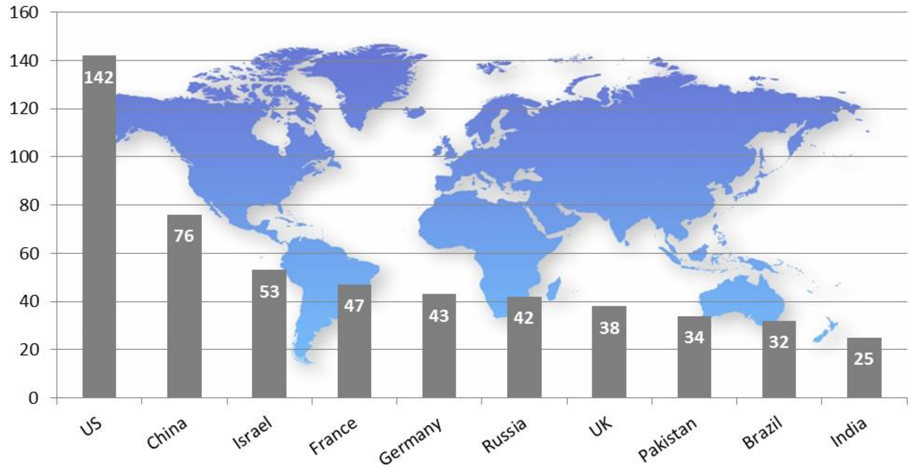

Figure 2-1: Top 10 Countries for Manufacturing UAVs [11]

The operational status of the UAV designs can be found in Figure 2-2, confirming the fact that some UAV designs are still in development. Only 37% of the 813 UAV designs are in operation, the largest portion, 52% of the UAVs, is still undergoing development. This can be at the early conceptual design phase, testing and prototype phase or initial low rate production phase. The remaining 11% is unknown (9%) or other (2%), i.e. on hold. This figure also confirms the recent growth within the UAV market since more than half of the UAVs are still being developed. These UAVs will become operational within a few years.

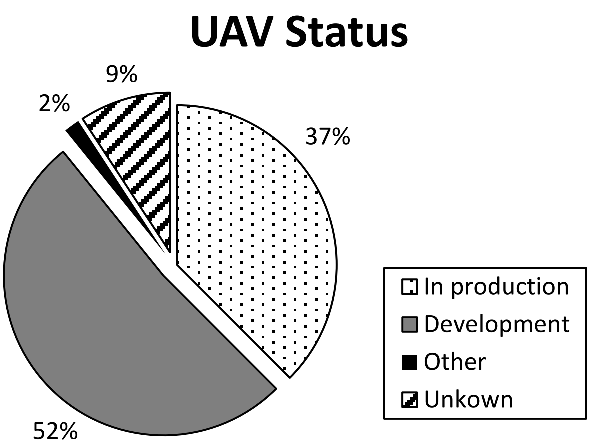

Figure 2-2: Status of the UAVs [11]

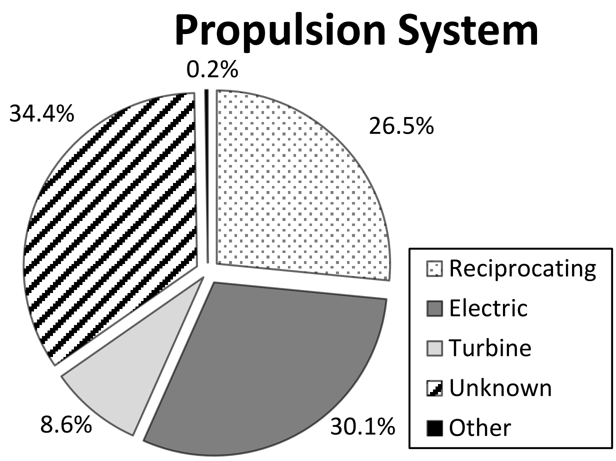

Figure 2-3: UAV Propulsion Overview [11]

Figure 2-3 gives an overview of the propulsion systems that are being used to power UAVs. Four main types of propulsion systems are being identified: reciprocating, electrical, turbine and other engines. It is however not possible to determine the propulsion system of 34.4% of the UAV designs from the AIAA dataset. About 30% of the UAVs are powered by an electrical engine. These are closely followed by the reciprocating engines (26.5%). Several reciprocating engine configurations are possible: two stroke, four stroke and rotary engines. Only 9% of the UAVs use a turbine based propulsion system which can also be subdivided into a number of configurations: turboshaft, turboprop, turbofan, turbojet and pulse jet. A final group, only 0.2%, represents the remaining propulsion systems, i.e. a hybrid engine. From all this data one can conclude that only a few UAVs are powered by a turbine, while most UAVs are either powered by a reciprocating or electrical engine. A final analysis on the existing UAV design investigates the VTOL and hover capabilities. About 20% of the UAVs have VTOL and hover capabilities, meaning that the majority of the UAVs does not have VTOL and hover capabilities. It was therefore decided, in collaboration with the various supervisors and supporting professors, to exclude the VTOL and hover requirements from this Master thesis. Moreover, modeling a UAV with such capabilities requires complex processes which do not suit this exploration study. UAVs powered by an MGT with VTOL and hover capabilities are therefore reserved for future research projects. Unfortunately, it is not possible to determine the percentage of military and civil UAVs from the

AIAA dataset. Moreover, some of the UAVs are being used for both civil and military applications, i.e., the Predator A from General Atomics. According to van Blyenburgh **[12]**, 70% of the UAV designs are used for military missions, the remaining part are civil/commercial, research, development vehicles and dual purpose UAVs.

2.4 Advantages and Disadvantages

Several academics have identified numerous reasons why one would like to use a UAV as a substitute of manned aircraft **[1,4]**. A number of operating advantages are identified, mainly the result of not having to house a human pilot. One of the major advantages is the fact that human lives are no longer jeopardized during high risk missions, for example: hostile environments, severe weather conditions, low altitude flights and flights above the Arctic region. There is also a weight saving possible if pilots are excluded from the design. Two pilots, windows, furnishings, instrument panels, control interfaces, support equipment and survival kits can all be removed from the aircraft resulting in a weight saving of approximately 250 kg **[6]**. A UAV can also have a higher endurance (up to 30 hours for UAVs using hydrocarbon fuels or multiple days for UAVs using solar power) compared to a human pilot who needs to be replaced after ± 5 hours **[1,11]**. Other advantages are higher acceleration, pressure and temperature limits; lower value loss in case of an incident/accident; higher precision in flight path; and more flexible packing since human pilots need a specific design space to operate properly compared to electronics **[1,6]**. The higher precision in flight path can be achieved since UAVs are always flying on instruments compared to human pilots who can fly both on VFR and IFR. All these advantages make the use of UAVs for certain civil applications an interesting possibility. There are however certain disadvantages in using UAVs as an alternative for manned aircraft **[1,6]**. A UAV only has a limited capability, depending on the robustness of the avionics to react to unusual or unexpected situations, unless an operator can intervene. The power consumption of the avionics, payload and communication is also higher which results in a higher power generation requirement, hence an increase in fuel consumption. If the communication system of the UAV relies on satellite communication a gimbaled antenna needs to be installed within the fuselage. A gimbaled antenna consumes a large part of internal volume which can lead to an increase in drag coefficient. These disadvantages have to be incorporated when an assessment between a UAV and a manned aircraft is made.

2.5 Civil UAV Issues

By having a look at civil UAVs, one has to conclude that their use is far less widespread compared to the military equivalents. Clearly there are some issues regarding the UAV technology which causes this low number of operational UAVs for civil applications. One of the main reasons why civil UAVs are not used as much as their military equivalents is the lack of regulations which would allow UAVs to fly in non-segregated airspaces **[13]**. There are at the moment almost no possibilities, or only after a time consuming application process, which can take up to a few months, to certify UAVs. This is because aviation authorities do not allow UAVs to fly in the non-segregated airspace of the manned aircraft without a "sense and avoid" system **[8]**. This "sense and avoid" system detects other aircraft and diverts the UAV from the potential collision path all without interference from the UAV operator **[14]**. Fortunately there are plans to create a framework in order to certify UAVs in the near future and also the "sense and avoid" technology is being developed by several companies **[13]**. However, the regulation side, although it is a crucial aspect of the civil UAV implementation process, is considered to be out of the scope of this research. Ethical questions also need to be considered as an issue for civil UAVs. These ethical questions can arise when UAVs are being used for certain civil applications. Privacy concerns can occur when UAVs with optical equipment are being deployed above urban environments **[15]**. Moreover, the lack of a human pilot onboard the aircraft can create a safety risk when an unaccounted problem arises. It is impossible to design robust avionics that react properly to any unexpected or unusual situation, especially in case of an emergency situation. This is also a difficult task if the UAV is remotely controlled by a human operator. The human operator does not have the same situational awareness as an onboard pilot and lacks certain senses which could detect unwanted vibrations, unusual odors or sounds. To avoid these problems one could use several safety features or keep the velocity and weight as low as possible, minimize the energy in case of an accident in an urban environment. Several safety features (parachutes or airbags) can be installed on the UAV but have a weight penalty. A parachute lowers the impact velocity while an airbag increases the shock absorbing characteristics of the UAV **[13]**. If the selected application is located within an urban environment such systems could be installed to resolve the safety issues. Fortunately, both systems are already used on certain UAVs **[13]**. Most other technological issues have already been solved by military UAVs; and massive resources are currently still allocated for the development and production of those military UAVs. All these technologies are also beneficial for civil UAVs **[1]**. According to some academics almost all technical problems of the UAV technology have already been solved with the exception of the "sense and avoid" system, discussed previously **[16]**.

2.6 Design and Configuration

In general, the design process is similar to that of manned aircraft. Some significant differences are however present. UAVs have more design freedom, resulting in more configuration possibilities compared to manned aircraft. There are however additional constrains for UAVs that do not apply to manned aircraft (e.g. communication capabilities and power budgets). Other differences are mainly the result of not having to house a pilot. Pilots are often seated at the front of the fuselage. Excluding them from the design could initiate a packing optimization of the various components resulting in a better weight distribution. For the same reason, the fuselage can also be optimized for drag reduction. Depending on the chosen application, the smaller size of a UAV compared to manned aircraft influences the aerodynamic analysis. The smaller component sizes, which are often in combination with lower flight velocities, result in a flight regime at low Reynolds numbers **[17]**. This low Reynolds number regime ($Re < 10^5$) creates many complex flow phenomena within the boundary layer **[18]**. These flow phenomena are not well understood yet, making the design of vehicles flying in this regime challenging. For example, at low Reynolds numbers rough airfoils are performing better than smooth airfoils while at $Re > 10^5$ the opposite occurs **[19]**. Moreover, profile drag increases as Reynolds number decreases **[20]**. It is therefore sometimes necessary to use low Reynolds number airfoils. These are however vulnerable to wind gusts and precipitation turbulence **[21]**. Three different flow regimes can be distinguished **[22]**. The first regime ranges from $30{,}000 < Re < 70{,}000$ and is applicable to the MAVs. Within this regime it is crucial to determine the right airfoil section since large hysteresis in lift and drag forces, caused by the laminar separation, can occur with relatively thick airfoils. The second regime, in which MAV and small UAVs fly, ranges from $70{,}000 < Re < 200{,}000$. Laminar flow can be obtained which increases the airfoil performance but laminar separation bubbles can still create problems. The third regime starts above 200,000 entering the flight regime of the large UAVs and manned aircraft. The airfoil performance can be increased because the parasite drag of the separation bubble decreases due to the decreasing bubble length.

It becomes apparent that the design of a UAV is a complex process which involves multiple design disciplines. Several books, including books dedicated to UAV design, describe this design process in a stepwise and detailed manner **[4,6,23,24,25]**. Moreover, several academics have utilized this stepwise design process to come up with conceptual designs **[26,21,27,28,29]**. These UAV platforms ranged from the smaller UAVs to the larger UAVs with a variety of missions and propulsion systems (i.e.: imagery, surveillance and reconnaissance missions with hybrid-electrical propulsion). Each design process is preceded by a market analysis which studies the future needs of the specific industry, in this case the global UAV industry **[4]**. The results of the market analysis are used to determine the mission definition and accompanying mission profile. This mission profile sketches a typical mission of the UAV. Next, the top level requirements are determined; these include range, payload weight, altitude and velocity. This is followed by a weight estimation and an analysis of the detailed requirements, an interaction between both is required. The weight estimation determines several weight groups like MTOW, fuel weight, engine weight and OEW. The analysis of the detailed requirements on the other hand determines the wing loading, power or thrust loading, stall speed, take-off & landing performance and climb performance. The next step in the design process is to focus on the subcomponent design to determine the optimum wing and tail sizing, engine positioning, landing gear arrangement and fuselage characteristics. Combining all this results in a conceptual design of a UAV platform.

Similar to manned aircraft, UAVs also have a conventional configuration. The wing-tail twin-boom pusher engine configuration with a tricycle landing gear is considered to be the conventional configuration for UAVs **[6]**. Although the conventional configuration is hard to beat from a purely aerodynamic perspective, other configurations could also become interesting due to several mission requirements. No single best UAV configuration exists. Some requirement can even have multiple suitable configurations. The different considerations, advantages and disadvantages of the configuration options regarding the wing system, empennage, fuselage, propulsion integration and landing gear arrangement, according to J. Gundlach **[6]**, are given in Appendix A - UAV Design Configuration. During a design process several decisions regarding the different configuration options have to be made. However during the redesign phase of this project no major modifications to the configuration of the baseline UAV are made. This to allow for a proper comparison between the flight performance of the reciprocating engine and MGT, in order to highlight the potential of the MGT.

2.7 Propulsion Systems

The propulsion system is a major sub-component of the UAV and is responsible for propelling the UAV. The weight of a propulsion system is approximately 5-10% of the MTOW, this number however depends on the propulsion system that is being used and only serves as an indication **[30]**. The propulsion system of a UAV is also often responsible for the auxiliary power generation. The required auxiliary power generation of a UAV is generally higher compared to a manned aircraft because of the additional avionics and communication equipment **[6]**. The power generation is usually realized by adding an electric generator to the propulsion system or by using a battery. Few UAVs use an APU due to the increased complexity, acquisition cost and weight penalty **[6]**. The emphasis of this Master thesis is however on the UAV platform. Nevertheless, it is beneficial to have a general understanding of the various propulsion systems, especially the MGT propulsion system. A propulsion system is responsible for transforming some sort of energy source (e.g. battery, solar panel, fuel cell or liquid fuels) into mechanical energy which is then converted into a lift or thrust force **[4]**. The lift or thrust converter can be a propeller/rotor or fan/jet mainly depending on the velocity requirement. Combining an energy source, mechanical energy converter and a lift/thrust converter leads to a propulsion system. Several propulsion systems are used to power UAVs. According to Section 2.3, electric engines are used the most to power UAVs, followed by the reciprocating engines and gas turbines, respectively **[11]**. A fourth category includes all the remaining propulsion systems, including hybrids, nuclear engines and rocket propulsion. Each propulsion system has its advantages and disadvantages which influence the application area of the engine. The characteristics, advantages and disadvantages, according to J. Gunlach **[6]**, of the different propulsion systems are given in Appendix B - Propulsion Types.

The MGT technology is an interesting technology that could help increase the number of suitable gas turbines for UAVs. The MGT technology investigates small scale gas turbines (turbine diameter < ±20 cm) with a reduced power range compared to the full scale gas turbines, with relatively acceptable efficiencies **[31]**. The research into the MGT technology also analyzes turbines with a diameter of 2 cm and a power output range of 10-100 W, like the one developed by MIT **[32]**. These turbines are however considered to be too small for the purpose of this Master thesis. If the advantages of an MGT are utilized to the full potential, it would result in an interesting competitor for the electric and reciprocating engines **[33]**. With respect to electric engines MGTs have a higher energy density potential, in Wh/kg, (see Figure 2-4) due to the available energy sources. Fuel-based power combustion engines also have a higher power density (W/kg) compared to electric which is illustrated in Figure 2-5. The advantages compared to reciprocating engines are related to reliability and weight savings. MGTs have fewer moving parts; some turbines even only have one rotating spool, compared to the reciprocating engines (e.g. four-stroke and radial engines). The weight savings of an MGT, compared to a reciprocating engine, are the result of a higher power-to-weight ratio.

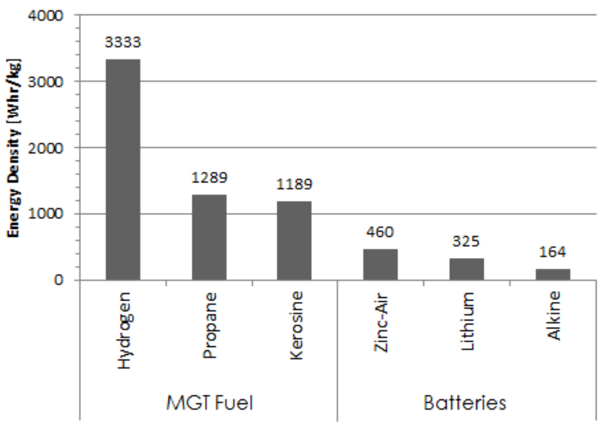

Figure 2-4: Comparison of the Energy Densities of Micro Gas Turbines and Batteries [33]

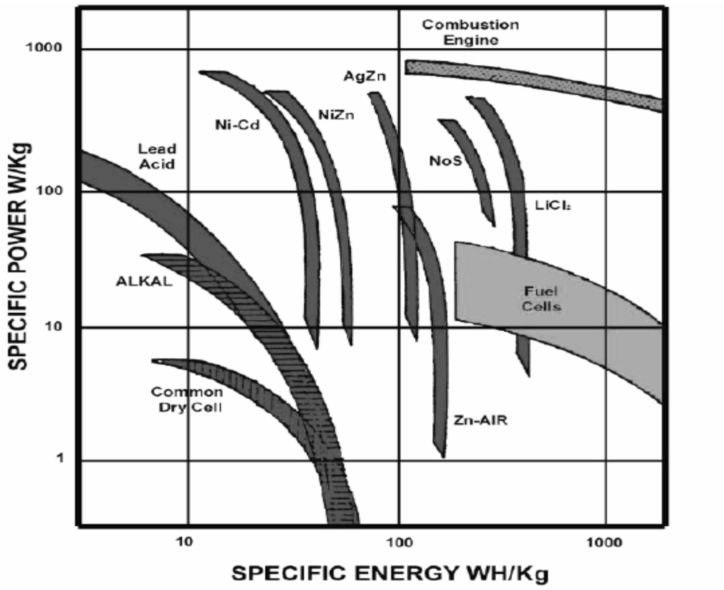

Figure 2-5: Power Density and Energy Density for Different Power Sources [33]

Designing a high performance MGT is still challenging and involves technical barriers to be overcome **[33]**. The remaining barriers of this technology are to design a turbine with an acceptable efficiency. The design of a MGT with positive power output is still a challenging task. Simply scaling a conventional gas turbine is not possible due to a number of design problems. The remaining design problems which cause these low efficiencies at the moment are the following **[34]**:

- The characteristics of the thermodynamic cycle need to be conserved; hence the enthalpy change in the compressor and turbine needs to be maintained. This can be achieved by conserving the velocity triangles, Mach number and Reynolds number. The latter one creates a conflict with the conservation of enthalpy change.
- Due to the smaller scale, distances between components are reduced. Hence, the compressor is heated by the turbine while the compressor is cooling the turbine. The end result is that both compressor and turbine are operating at lower efficiencies.
- Material and manufacturing techniques of today cannot cope with the small dimensions in combination with the high temperatures and rotation requirements.

High efficiency can only be obtained by solving these technological barriers. Several safety measurements are also required due to the high temperatures and rotation speeds. However, the MGT study is part of another research project **[5]**, therefore no further elaborations on the technology are made within this document.

3
Applications

This chapter discusses the possible applications of UAVs. The emphasis is on civil applications, military applications are only discussed briefly to give the reader a general understanding. First, all future civil applications are identified, see Section 3.1. Next, the application selection procedure is outlined in Section 3.2. This selection procedure narrows down the number of possible applications tailored for a civil UAV powered by an MGT based propulsion system. An overview of the final applications is presented in Section 3.3. One of these is further developed into a case study, see Chapter 4, acting as a baseline for this Master thesis.

3.1 Future Civil Applications

As already stated in Chapter 2, the use of UAVs within the Military is common. They have proven their potential on the battlefield during numerous conflicts around the world and will probably increase their contribution in the future even more **[2]**. At the moment they are being deployed for reconnaissance, surveillance, intelligence gathering, target practice, border patrol and more recently also for strike missions **[3]**. They execute the so called Dull, Dangerous and Dirty (DDD) roles **[4,16]**. An example of a dull role could be a surveillance mission lasting several hours. Reconnaissance missions above heavily defended airspaces are considered as dangerous roles while monitoring the environment for nuclear or chemical contaminations can be categorized as dirty roles. These DDD roles pose imminent risks for human pilots which makes the choice of a UAV rational. This results in a large application field for military UAVs covering all sizes and weights.

The number of reported civil UAVs (operational) is however limited at the moment, see Section 2.3. Example missions which already utilize UAVs are: protection and patrol for oil companies, magnetic surveys and forest management **[1,9]**. Fortunately, numerous civil applications have been proposed by several academics and the general literature which would like to exploit the benefits of civil UAVs. The following applications are proposed **[4,8,9,16]**:

- Fire-fighting support
- Disaster assessment and management
- Search and rescue assistance
- Border surveillance
- Police surveillance
- Counter terrorism operations
- High value objects and VIP guarding
- Ground and sea traffic surveillance
- Telecommunications
- Environmental control and monitoring (including air and sea pollution)
- Crop monitoring
- Animal surveillance
- Fisheries protection and management
- Mineral exploration
- Ground mapping and aerial photography
- Meteorological observation
- Power and pipeline monitoring
- Freight carrying
- Crowd control support

All these applications can be subdivided into three large domains: commercial, public safety and remote sensing applications. The latter one has the largest number of applications, especially earth monitoring applications. The public safety domain also shows some great potential but most of these applications operate in urban environments resulting in the aforementioned safety risks (Section 2.5). The commercial applications have the largest potential if a solid business case exists. From this list it is concluded that the application with the highest potential is the power and pipeline monitoring application which requires a UAV with a low flight velocity and optical equipment **[1,16]**.

3.2 Selection Procedure

The application is one of the main drivers of the UAV platform design since it determines the design requirements. Endurance, velocity, range, altitude or payload requirements play a vital role in the design process of a UAV. Especially the velocity requirement can be a dominant factor for both the UAV configuration and the propulsion system (turboprop or turbojet/fan) **[4]**. In general higher airspeed comes with higher fuel consumption which influences payload weight, endurance, range, UAV size and financial cost. Selecting an appropriate application for an MGT is therefore crucial.

To start the selection procedure several requirements per application are identified. The requirements per application are: range, endurance, altitude, velocity and whether or not VTOL and hover capabilities are necessary. The requirements table can be found in Appendix C - Civil Applications with Requirement Details. The applications are divided according to the three application domains, as discussed previously. An extra column is added indicating the type of UAV that could be used for the corresponding application. Next, the applications are arranged according to the best suited propulsion system based on an MGT. Three possibilities are available: turboshaft, turboprop and turbofan/jet. Range and endurance are left out during this selection step. If a high altitude and flight velocity are required, a turbofan/jet engine is desired. A turboprop is selected for applications which require a medium altitude and flight velocity. If the application requires VTOL/hover capabilities and the altitude and velocity range are low, then a turboshaft is preferred. An overview of the applications per propulsion system can be found in Figure 3-1. From this figure it can be concluded that some applications could use multiple propulsion system. Also most applications require a turboprop as propulsion system. An explanation of the different requirement options can also be found in in Appendix C - Civil Application with Requirement Details.

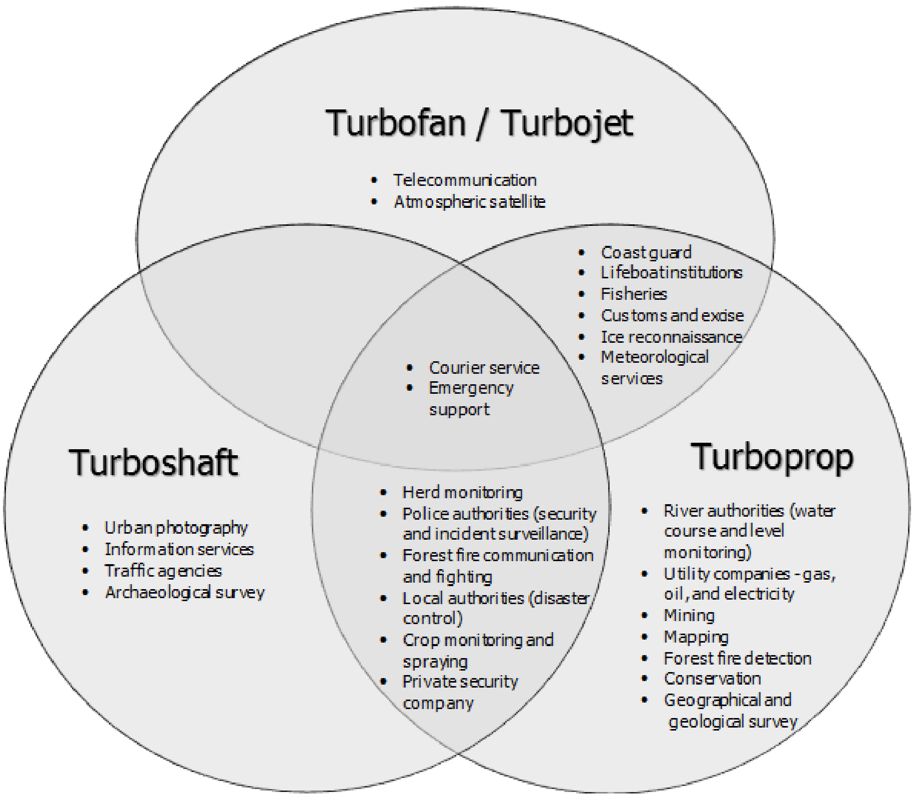

Figure 3-1: UAV Applications per Propulsion System

As one of the final steps in the selection procedure an overview of all applications together with the best suited propulsion system and UAV type is provided, see Figure 3-2. Several conclusions can be deduced from this figure. Larger UAVs either need a turboprop or turbofan/jet, while the smaller UAVs prefer a turboshaft or turboprop. The propulsion system for emergency support and courier service applications strongly depends on the required range and if VTOL/hover capabilities are necessary. Short range applications result in the use of a turboshaft or turboprop.

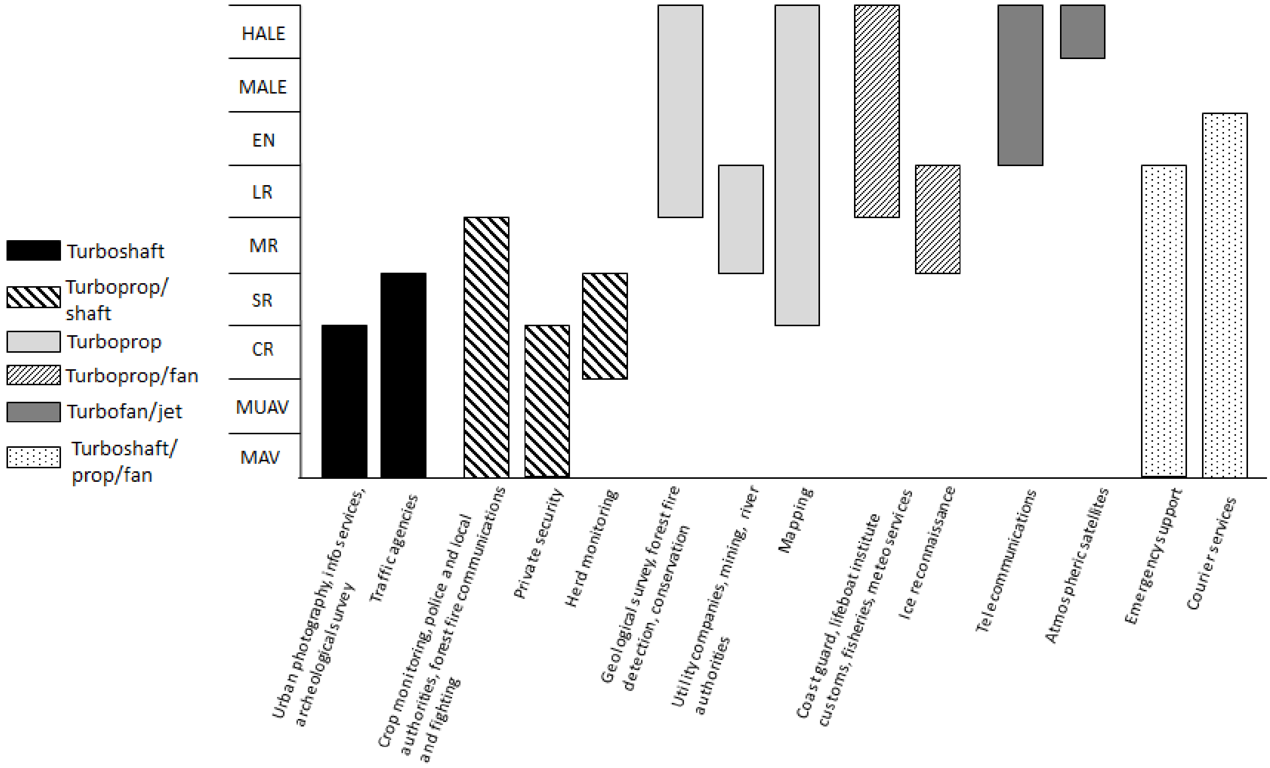

Figure 3-2: Civil Applications together with the Best Suited Propulsion System and UAV Type

3.3 Application Proposals

A clear picture of all the civil applications together with their requirements (in terms of range, endurance, altitude, velocity and whether or not VTOL and hover capabilities are necessary), UAV type and propulsion system is now available. The next step is to analyze the existing UAVs to identify any relation between the performance characteristics of the UAV and their application. To narrow down the search, and after careful consideration together with the various supervisors and supporting professors, a certain power range was identified. The selected power range is from 30 to 60 kW, only UAVs which have an output power between this range are analyzed. This power range has not been investigated yet and differs significantly from the power outputs of conventional gas turbines used for manned aircraft resulting in a new research field. Out of 813 UAVs only 25 UAVs fit within this power range each using a reciprocating engine, confirming the need of the new research field **[11]**. The flight performance characteristics of these UAVs are analyzed in order to discover useful relations linking the size of a UAV to the power output or application. The following relations are investigated:

- Range and endurance
- Velocity and power
- Endurance and power
- Range and power
- MTOW and power
- Span and MTOW
- Payload and MTOW
- Endurance and MTOW
- Range and MTOW

The graphs can be found in Appendix D - Existing UAVs within the 30-60 kW Power Range. From these graphs it becomes clear that there are no useful trends within the data except for the span, payload, endurance and range versus MTOW; which follow from aircraft sizing. Since no useful trends can be deducted from the existing UAV data three promising applications are chosen; power and pipeline inspection, package delivery and forest fire support or mining exploration. The first application, which is a commercial application, is selected because it has the greatest potential to be realized in the near future according to some academics, as already stated in Section 3.1. The second application is suggested by the supervisors and supporting professors, and is a humanitarian application. The final and third application can both be commercial and humane. For each application a mission description is given together with the mission requirements, see Table 3-1 and a best suited existing UAV.

- **Application 1: Power and Pipeline Inspection**
  The mission consists of inspect flights alongside power and pipelines on a regular basis. The UAV flies at an appropriate velocity and altitude in order to inspect the long stretches of power and pipelines which were previously being monitored by car or helicopter. The range and endurance requirements of this UAV are derived from the longest power and pipelines in the world **[1]**. The optical equipment determines the velocity, altitude and payload requirements **[1]**. A night camera or a low light camera can be installed on the UAV allowing night operations. Unfortunately, no UAV within the specified power range exist. The UAV with the closest requirement match is the Harfang EADS and is outside the 30-60 kW range. It has an 86 kW reciprocating engine and is used for reconnaissance and data collecting applications **[36]**. The Harfang is classified as a MALE UAV and has a wingspan over 16 m **[36]**.

- **Application 2: Package Delivery**
  The goal of this mission is to deliver packages to remote areas which have limited or difficult accessibility. This is especially useful in developing countries which do not have an appropriate road infrastructure. The UAV fits into a large network of UAVs and is responsible for transportation between hubs. Small UAVs with VTOL and hover capabilities are used to distribute the packages from the hubs to the desired locations. Average distances between capitals of African countries are used to derive the range requirement. The content of the packages can vary between missions. The packages can be weight or volume limited. Again no UAV is found within the specified power range. The General Atomics Predator A (RQ-1) is selected to perform the mission. It has a reciprocating engine which produces 86 kW of output power and is used for surveillance and data collecting applications **[37]**. The Predator A has been used on large scale by the United States of America for various military operations.

- **Application 3: Forest Fire Support or Mining Exploration**
  The task of this UAV is to support forest fighting services by spotting potential fires. If a forest fire is detected, the UAV starts circling above the fire to gather intelligence for the fire department. The UAV can also serve as a communication transmitter if the fires are located in remote areas or if other communication possibilities are inoperative/damaged by the fire. The UAV can also be used for more commercial applications; it could for example search for potential mining areas. Only the payload and data processing differs between these two missions. As with the previous two applications, also these application requirements are not fulfilled by a UAV within the specified power range. Again a UAV outside the 30-60 kW power range is selected, the Denel Dynamics Bateleur. The UAV has a 75 kW reciprocating engine and is used for surveillance and patrol missions **[38]**.

3.4 Selected Case Study

If the mission requirements of the three application proposals are compared with each other, one has to conclude that they have similar mission requirements, hence similar UAV specifications are required (Table 3-1). All three applications would require a MALE UAV. There are also only minor differences in the configuration of the selected UAVs. All three UAVs have high aspect ratio wings, one pusher propeller in the back and multiple tail surfaces. It was therefore decided to develop one UAV that could be used to perform all three proposed applications. The selected UAV is the Harfang EADS, since it has the closest specification match for all three applications. A model of this UAV is developed to determine the flight performance in order to identify the effect on mission performance if an MGT is used instead of a reciprocating engine.

Table 3-1: Mission Requirements and UAV Specifications [1,36,37,38]

	Requirements Application 1	Specifications Harfang EADS	Requirements Application 2	Specifications Predator A (RQ1)	Requirements Application 2	Specifications Bateleur
Range	900 km	965 km	1100 km	1100 km	400 km	750 km
Cruise Velocity	80 km/h	270 km/h	> 300 km/h	270 km/h	80 km/h	250 km/h
Endurance	20 h	24 h	4 h	40 h	30 h	24 h
Altitude	1000 m	7500 m	> 5000 m	7620 m	5000 m	8000 m
Payload	10 kg	250 kg	100 kg	Unknown	10 kg	250 kg

Part II - Modeling Phase

4
Case Study Definition

This chapter gives an overview of the case study used during the Master thesis. The input for this case study involves geometry and performance parameters of the UAV, a mission profile which the UAV will fly and a list of assumptions. The case study serves as a baseline for this Master thesis. Section 4.1 states the model dimensions and performance specifications, derived from the existing UAV. An overview of the mission profile can be found in Section 4.2. A list of assumptions is given in Section 4.3.

4.1 UAV Geometry Model

The geometry parameters are based on the Harfang EADS (MALE UAV) airframe dimensions. Most dimensions are obtained using a scaled three-view drawing of the UAV which can impose some deviations from the actual dimensions **[36]**. The effect of the dimension uncertainty is investigated in the sensitivity analysis which can be found in Chapter 7. The general dimensions of the airframe and landing gear can be found in Figure 4-1. These dimensions are used to develop the aerodynamic model of the UAV and the component weights.

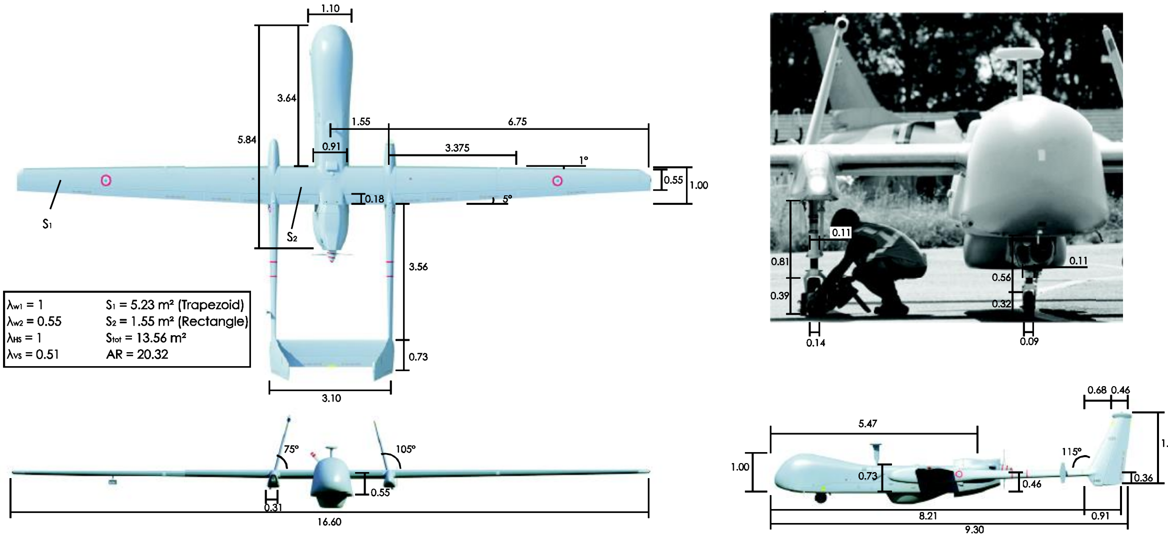

Figure 4-1: General Airframe Dimensions

The flight performance data is derived from the performance specifications of the Harfang EADS and can be found in Table 4-1. **[36]**

Table 4-1: UAV Model Performance and Weight Data [36]

Performance & Weight Data	Value
Endurance	24 h
Maximum velocity	56.5 m/s
Ceiling altitude	7620 m
Maximum load factor	3.8 [-]
MTOW	1250 kg
Payload weight	250 kg
Maximum fuel weight	343 kg
OEW	657 kg

The main wing is modeled using one airfoil section along the wingspan: the NACA 6414-43 airfoil, a modified NACA 4 digit airfoil, see Figure 4-2. The airfoil is derived using measurements from the wing tip airfoil section, which are derived from illustrations **[36]**. The main wing also has a plain flap system which has three flap settings; 0°, 5° (used during take-off) and 20° (used during approach and landing). The flap system has a flap chord of 18% of the local wing chord. It is installed on the straight wing part and on the inner half of the swept wing part. The outer half of the swept wing part houses the ailerons used for maneuvering. The main wing is attached to the fuselage with a 3° forward rotation. This wing twist is assumed constant along the wing span, due to a lack of data. The horizontal and vertical stabilizers have a standard NACA 0012 airfoil section.

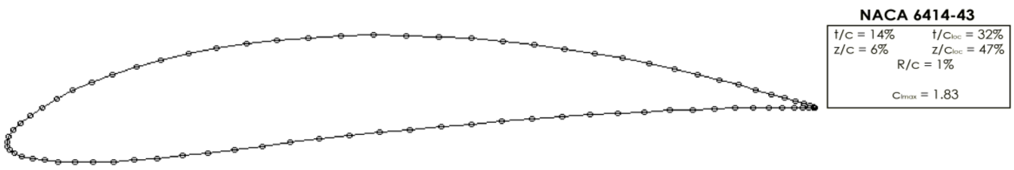

Figure 4-2: Main Wing Airfoil

The original engine of the UAV is modeled in order to obtain the baseline flight performance characteristics. The Harfang EADS uses a turbocharged four stroke Rotax 914 rear mounted pusher engine with a maximum power output of 86 kW **[53]**. The dry engine weight is 69.7 kg; the installed engine weight (adding engine mounts and external alternator) is 74.7 kg. Three scaled-down versions (86, 70 and 60 kW) of the TP100 turboprop are used to model the MGT flight performance. Each turboprop size also has different technology levels. An overview of the engines used during this project is given in Table 4-2. The analysis of the reciprocating engine is part of this Master thesis, while the analysis of the turboprop engine is part of another Master thesis **[5]**. Both engines have a fixed pitch two blade propeller with a diameter of 1.6 m. The ideal propeller theory or actuator disk theory is used to model the propeller performance, see Section 5.3. The reciprocating engine has a gearbox ratio of 2.43:1 **[53]**.

Table 4-2: Reciprocating Engine and MGT Overview

	Reciprocating Engine	Turboprop Engines (TIT in [K])		
Technology Level	/	TL 0: TIT = 1144 - Pr = 4.6 TL 1: TIT = 1144 - Pr = 6 TL 2: TIT = 1200 - Pr = 7 TL 3: TIT = 1250 - Pr = 8	TL 0: TIT = 1144 - Pr = 4.6 TL 1: TIT = 1144 - Pr = 6 TL 2: TIT = 1200 - Pr = 7 TL 3: TIT = 1250 - Pr = 8	TL 2: TIT = 1200 - Pr = 7 TL 3: TIT = 1250 - Pr = 8 TL 4: TIT = 1250 - Pr = 8 η =+2%
Power Output	86 kW	86 kW	70 kW	60 kW

4.2 Mission Profile

The mission profile gives a typical example mission that the UAV will have to perform, see Figure 4-3. It is used to assess the difference between a reciprocating engine and MGT in terms of flight performance. The mission profile consists of the following seven phases, in chronological order: take-off, climb, cruise, descent, loiter, approach and landing.

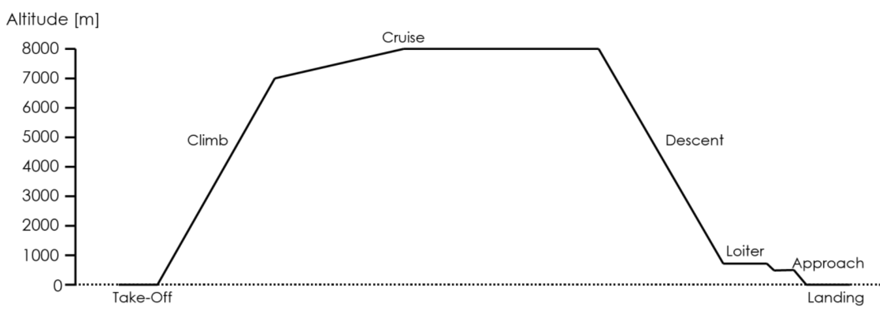

Figure 4-3: Mission Profile UAV Model

The UAV takes off with maximum power until it reaches the screen height and fulfils the user-specified take-off time, which cannot exceed the maximum operating conditions of the engine. During the climb phase the engine is throttled back to the maximum continuous engine setting. Once the UAV reaches the cruising altitude the engine setting is such that drag equals thrust and level flight can be maintained. The maximum cruise altitude is 7620 m, as stated in Section 4.1. Next, the UAV enters the descent phase until the altitude is reduces to 900 m. A loiter maneuver is performed at this altitude followed by an approach phase. During the approach phase the UAV first descents towards 500 m where it flies level to intersect the ILS, to initiate the final descent phase. The landing phase starts as soon as the UAV reaches the screen height. The landing phase has an airborne and ground run phase. The mission simulation is concluded once the UAV has come to a complete stop.

4.3 General Assumptions

Several assumptions are made to develop the model of this case study. These assumptions simplify the calculations; though decrease the fidelity of the result. It is therefore important to keep track of all assumptions and understand their influence. It should however be noted that the research project is an initial exploration study which only deals with a conceptual design study, hence detailed models and high accuracy are not yet desired at this stage. The correctness of the results is investigated by means of a verification process, see Section 6.6. To aid this process a sensitivity analysis has been conducted. The results of this analysis can be found in Chapter 7. The assumptions defined by the MGT study, to obtain thrust and fuel consumption data, are outlined in **[5]**. The following general assumptions are made during this Master thesis.

- Point performance is integrated to obtain path performance in order to determine mission performance. A higher time step results in a less accurate result. Different time steps are therefore used depending on the expected change in state variables.
- The aircraft model is assumed to be a rigid point mass body. The translational motion of the aircraft is therefore a response of external forces acting on the C.G. of the aircraft. Complex motions of wing and fuselage bending are not taken into account.
- Wind effects are not included into the model. These could however affect take-off and landing distances, endurance, fuel consumption and range. This however does not affect the comparison of the engine types.
- The braking force during the landing phase is calculated using a fixed friction coefficient. The friction coefficient does however vary with the so-called braking slip ratio. Normally, it gradually increases with decreasing forward velocity. The ground run of the landing maneuver is however only of limited duration and the influence is therefore not notable in the mission results.
- During the loiter maneuver coordinate turns are performed assuming a nonsideslipping flight condition. This maneuver can be controlled by the autopilot with relative limited efforts.
- The propeller is modeled using the ideal propeller theory (actuator disk theory), assuming a user-specified propeller propulsion efficiency. It is also assumed that a fixed pitch propeller is used. To avoid singularity problems at static conditions a propeller with virtual rotation speed as power setting is introduced.
- The specific fuel consumption at take-off conditions is multiplied with the altitude correct power to obtain the fuel consumption for the reciprocating engine at different altitudes. The specific fuel consumption is assumed to be complying with the propeller model.
- Fuel is stored inside the fuselage at the wing C.G. location. No fuel is stored in the wing or empennage.
- The C.G. location is assumed to be located on the lateral symmetry axis. This also does not influence the results since no control and stability analysis is performed.
- The lift coefficient is calculated assuming incompressible, inviscid irrotational flow. The drag coefficient is determined using the drag polar equation in which the zero-lift drag coefficient is obtained using the component build-up technique. The zero-lift drag coefficient uses the thin plate approximation. The Oswald factor is determined using an empirical formula. These assumptions still create an aerodynamic model with acceptable accuracy for this exploration study. The sensitivity analysis also investigates the influence of the critical Reynolds number, Oswald factor and total drag coefficient.

5
Flight Performance Simulation

A flight performance program is developed to numerically simulate the flight performance of the baseline UAV with the various engines; and the redesign. The program follows the various mission segments chronologically. The user can select different flying strategies (maximizing range endurance) for a number of mission segments. The flight performance calculator generates the following output to determine the mission performance:

- Total and mission phase endurance
- Height profile
- Velocity profile
- Fuel consumption
- Thrust
- Total and mission phase range
- Lift and drag forces and coefficients
- Aircraft flight angles
- Height, velocity and angle derivatives

The methodology to determine the flight performance is split up into four parts. Section 5.1 discusses the component weight breakdown analysis to determine the weight of each component and the C.G. location of the UAV. The aerodynamic analysis is discussed in Section 5.2, while Section 5.3 outlines propulsion analysis to determine thrust and fuel flow. The framework of the flight performance analysis is listed in Section 5.4. This section also discusses the available flying strategies. The results of each analysis can be found in Chapter 6 together with a verification of the model.

5.1 Components Weight Breakdown

Only limited information about the UAV components weight is present; partially the result of the high number of configuration possibilities and size differences **[29]**. Therefore it is not possible to use common design methodologies which rely on large statistical databases. Having an accurate weight estimation of the various structural components is however crucial to determine the C.G. of the UAV. It is also required during the redesign phase for the comparison of the reciprocating engine and MGT. Weight Estimation Relationships (WER) are therefore used to resolve this problem. Various WERs are used to determine the components weights while the fuel and payload weight are derived from the baseline UAV, see Section 4.1. The component weight estimation can be found in Section 5.1.1. The determination of the center of gravity is being discussed in Section 5.1.2. A Matlab script has been set up to calculate the WERs and determine the C.G. location. The input of this Matlab script can be found in Appendix E - C.G. Calculator Input.

5.1.1 Weight Estimation Relationships

The take-off weight can be split up into five groups, see equation 5-1. The weight of the trapped fuel and oil is considered to be zero, as is the crew weight. The empty weight can further be subdivided into seven subgroups (equation 5-2). These seven subgroups are the main structural elements of a UAV **[6]**. Their weight and individual C.G. location determines the C.G. of a UAV with an acceptable accuracy for a conceptual design level.

$$W_{TO} = W_E + W_{PL} + W_{Fuel} + W_{tfo} + W_{Crew} \tag{5-1}$$
$$W_E = W_{Wing} + W_{Fus} + W_{Emp} + W_{Prop} + W_{Boom} + W_{LG} + W_{Misc} \tag{5-2}$$

Unfortunately, no large statistical databases are present for UAV weight determination, as has been stated in the introduction of this chapter. For many UAV classes suitable weight estimation procedures simply do not exist. The weight of each component is therefore determined using WERs based on manned, conventional aircraft. WERs are empirical relations based on historical data of other aircraft with a similar configuration, size and mission profile. Parametric WERs can be useful in the conceptual design phase for rapid design space exploration. WERs of manned aircraft should however be used with caution since configuration and size can deviate significantly for UAVs leading to erroneous results, especially if the results are extrapolated. One should always examine the intended purpose of a WER and analyze the range of the input parameters. Common sense is also required to determine if the weight output is in line with other structural elements and fits the expectations of the designer. Non-credible output weights should be excluded from the analysis. Validation of the results is also difficult due to the rarely available public weight reports. The limited data problem is solved by using WERs of various authors and compare the outcome. Unrealistic results are excluded from the analysis while the remaining results are combined to determine the weight of the structural component in question, by averaging out the results. The excluded methods are listed in Section 6.1. An un-weighted average is used since it is difficult to assign weight values to each method. The weights of all seven subgroups are validated by combining them and comparing the overall result to the known MTOW of the baseline UAV. **[6]**

Three WERs of different authors are used to determine the wing weight, see Table 5-1. MALE UAVs often have a wing with high aspect ratio (between 20 and 30), a wing thickness ratio of about 14% to 18% and a small sweepback of maximum 10°. Carbon fiber is a popular material for the wing structure. These properties are similar to the wing properties of modern sailplanes. It is therefore possible to use the WER developed for manned sailplanes by Gerard (equation 5-3). The WER of Torenbeek makes use of an iterative process to determine the wing weight, see equation 5-4. The final wing WER, equation 5-5, is developed by Yi and is specifically for HALE UAVs.

Table 5-1: Different Wing WERs

Author	WER Wing	
Gerard **[40]**	$W_{Wing} = 0.0038 \cdot (n_{ult} \cdot W_{TO})^{1.06} \cdot AR^{0.38} \cdot {S_W}^{0.25} \cdot (1+\lambda)^{0.21} \cdot {(t/c)_r}^{-0.14}$	**5-3**
Torenbeek **[25]**	$W_{Wing} = 8.94 \cdot 10^{-4} \cdot K_{no} \cdot K_{\lambda} \cdot K_{Eng} \cdot K_{uc} \cdot K_{st} \cdot \left[K_b \cdot n_{ult}\left(W_{Des} - 0.8 \cdot W_{Wing,Guess}\right)\right]^{0.55} \cdot b^{1.675} \cdot {(t/c)_r}^{-0.45} \cdot \left(\cos\Lambda_{1/2}\right)^{-1.325}$	**5-4**
Yi **[41]**	$W_{Wing} = 0.0118 \cdot \dfrac{{S_W}^{0.48} \cdot AR \cdot M^{0.43} \cdot {W_{TO}}^{0.84} \cdot {n_{ult}}^{0.84} \cdot \lambda^{0.14}}{(t/c)^{0.76} \cdot \cos\left(0.0175 \cdot \Lambda_{1/2}\right)^{1.54}}$	**5-5**

The fuselages of most MALE and HALE UAVs have a high fineness ratio and often have the engine intake integrated into the fuselage. The first out of five (Table 5-2) WERs to estimate the fuselage weight, is based on hand-launched glider aircraft which have a fineness ratio of a least 4:1 (Gundlach, equation 5-6). The second and third WERs are both developed by Raymer, one for fighter/attack aircraft and one for general aviation aircraft, see equation 5-7 and 5-8 respectively. The fourth WER is developed by Howe and is applicable for single engine aircraft (equation 5-9). The final WER to estimate the fuselage weight is developed by Yi and is again specifically for HALE UAVs, see equation 5-10. Most of the methods are however underestimating the weights of conventional fuselage of light aircraft, since they are developed for much higher MTOWs. This problem is however counteracted by the fact that UAV fuselages are usual more efficiently designed, hence have a lower weight per unit area; making these methods more appropriate. The higher efficiency is the result of fewer breaks in critical load paths (no windows and access doors) and more use of composite structures.

Table 5-2: Different Fuselage WERs

Author	WER Fuselage	
Gundlach **[6]**	$W_{Fus} = 0.5257 \cdot F_{MG} \cdot F_{NG} \cdot F_{Press} \cdot F_{VT} \cdot F_{Matl} \cdot {l_{Struct}}^{0.3796} \cdot (W_{Carried} \cdot n_{ult})^{0.4863} \cdot {V_{Eq,max}}^{2}$	**5-6**
Raymer (Fighter attack) **[23]**	$W_{Fus} = 0.499 \cdot K_{dwf} \cdot {W_{TO}}^{0.35} \cdot n_{ult} \cdot l_{Fus} \cdot {h_{Fus}}^{0.849} \cdot {w_{Fus}}^{0.685}$	**5-7**
Raymer (GA) **[23]**	$W_{Fus} = 0.052 \cdot {S_{Wet,Fus}}^{1.086} \cdot (n_{ult} \cdot W_{TO})^{0.177} \cdot {l_t}^{-0.051} \cdot \left(\frac{l_{Fus}}{h_{Fus}}\right)^{-0.072} \cdot \left(\frac{1}{2}\rho_{crz} \cdot {V_{crz}}^{2}\right)^{0.241}$	**5-8**
Howe (Single Engine) **[42]**	$W_{Fus} = 0.053\left[l_{Fus}(h_{Fus} + w_{Fus})(0.3048)^2\sqrt{V_{Des}}\right]^{1.5} \cdot 2.2$	**5-9**
Yi **[41]**	$W_{Fus} = 0.0025 \cdot {K_{Inlet}}^{1.42} \cdot q^{0.283} \cdot {W_{TO}}^{0.95} \cdot \left(\frac{l_{Fus}}{h_{Fus}}\right)^{0.71}$	**5-10**

For the estimation of the horizontal tail weight a total of five WERs are used, see Table 5-3. Palumbo assumes a simple constant aerial weight to determine the tail weight (equation 5-11). Torenbeek on the other hand estimates the horizontal tail weight to be a certain percentage of the empty weight, see equation 5-12. The remaining WERs are developed by Raymer, Roskam and Howe (equation 5-13, 5-14 and 5-15 respectively). It appears to be that the tail weight is relatively insensitive towards the moment arm length but shows a greater sensitivity towards the ultimate load factor and design dive speed **[29]**.

Table 5-3: Different Horizontal Tail WERs

Author	WER Horizontal Wing	
Palumbo **[43]**	$W_{HT} = WA_{Emp} \cdot S_{HT}$	**5-11**
Torenbeek **[25]**	$W_{HT} = 0.035 \cdot W_E$	**5-12**
Raymer (GA) **[23]**	$W_{HT} = 0.016(n_{ult} \cdot W_{TO})^{0.414} \left(\frac{1}{2}\rho_{crz} \cdot {V_{crz}}^{2}\right)^{0.168} \cdot {S_{HT}}^{0.896} \left(\frac{100 \cdot t/c}{\cos \Lambda_{HT}}\right)^{-0.12} \left(\frac{AR}{\cos^2 \Lambda_{HT}}\right)^{0.043} {\lambda_{HT}}^{-0.02}$	**5-13**
Roskam **[24]**	$W_{HT} = K_{HT} \cdot S_{HT}\left[3.81\frac{{S_{HT}}^{0.2} \cdot V_{Des}}{1000(\cos \Lambda_{HT})^{0.5}} - 0.287\right]$	**5-14**
Howe **[42]**	$W_{HT} = 0.8(0.028)\left[\left(\frac{b_{HT} \cdot S_{HT}}{\cos \Lambda_{HT}}\right)\left(\frac{1+2\lambda_{HT}}{3+3\lambda_{HT}}\right)\left(\frac{n_{ult} \cdot W_{TO}}{S_{HT}}\right)^{0.3}\left(\frac{V_{Des}}{t/c}\right)^{0.5}\right]^{0.9} \cdot 2.2$	**5-15**

Three WERs are available to estimate the vertical tail weight, these can be found in Table 5-4. Equation 5-16 by Palumbo is also applicable to vertical tails. The two other remaining WERs are developed by Howe and Nicolai/Anderson, see equation 5-17 and 5-18 respectively. Also here the methods are relatively insensitive towards changes in moment arm length. A greater sensitivity towards ultimate load factor and design dive speed is present. The methods are only slightly sensitive to sweep angle and thickness-to-chord ratio.

Table 5-4: Different Vertical Tail WERs

Author	WER Vertical Tail	
Palumbo **[43]**	$W_{VT} = WA_{Emp} \cdot S_{VT}$	**5-16**
Howe **[42]**	$W_{VT} = 0.8(\#_{Fins})\left(0.11156 \cdot {S_{VT}}^{1.3}\right)\left(\frac{l_t}{l_{Fus}}\right)^{-0.2422} {V_{Des}}^{0.7812} \cdot 2.2$	**5-17**
Nicolai/Anderson **[44,46]**	$W_{VT} = 98.5\left[\left(\frac{n_{ult} \cdot W_{TO}}{100\,000}\right)^{0.87}\left(\frac{S_{VT}}{100}\right)^{1.2}\left(\frac{b_{VT}}{t_{VT,r}}\right)^{0.5}\right]^{0.458}$	**5-18**

Table 5-5 finally, lists the WERs of some miscellaneous items (landing gear, fuel system and avionics) and the tail booms. The WER for the booms has been developed by Gundlach (equation 5-19). Gundlach also estimated the landing gear weight as a percentage of the MTOW, see equation 5-20. Yi also relates the landing gear weight to the MTOW (equation 5-21). Equation 5-22 developed by Gundlach estimates the weight of the fuel system which includes the fuel tank, fuel pumps, valves, venting and fuel lines. A total of three WERs are available to estimate the weight of the avionics. This is however the most disparate weight group and is influenced by the mission and autopilot requirements. Gundlach, Torenbeek and Roskam base their WER on the MTOW; equation 5-23, 5-24 and 5-25 respectively. The engine, fuel and payload weight are derived from the specifications of the baseline UAV, while the weight of the propeller and control surfaces are not taken into account.

Table 5-5: Miscellaneous WERs

Author	WER Vertical Tail	
Gundlach **[6]**	$W_{Boom} = 0.14 \cdot l_{Boom} \cdot W_{Cant}$	**5-19**
Gundlach **[6]**	$W_{LG} = F_{LG} \cdot W_{TO}$	**5-20**
Yi **[41]**	$W_{LG} = 0.165 \cdot {W_{TO}}^{0.84}$	**5-21**
Gundlach **[6]**	$W_{Fuel,Sys} = 0.692 \cdot {W_{Fuel}}^{0.67}$	**5-22**
Gundlach **[6]**	$W_{Avion} = 0.11 \cdot W_{TO}$	**5-23**
Torenbeek **[25]**	$W_{Avion} = 40 + 0.008 \cdot W_{TO}$	**5-24**
Roskam **[24]**	$W_{Avion} = \left(15 + \frac{0.032 \cdot W_{TO}}{1000}\right) + \#_{Eng}\left(5 + \frac{0.006 \cdot W_{TO}}{1000}\right) + 0.15\frac{W_{TO}}{1000} + 0.012 \cdot W_{TO}$	**5-25**

5.1.2 Center of Gravity

Once the weight of every component is determined one needs to estimate the C.G. location of the component in question to calculate the overall C.G. location using equation 5-26. The C.G. coordinates of each component are determined using a reference datum which is commonly located at the nose and below the UAV on the symmetry axes. The center of gravity will shift during flight as fuel is burned. A shift in C.G. is however not take into account since it would complicate calculations by a too large extend. The lateral C.G. location is assumed to be located on the symmetry axis.

$$X_{CG} = \frac{\sum W_{(i)} \cdot X_{(i)}}{W_{Tot}}, \quad Y_{CG} = \frac{\sum W_{(i)} \cdot Y_{(i)}}{W_{Tot}}, \quad Z_{CG} = \frac{\sum W_{(i)} \cdot Z_{(i)}}{W_{Tot}} \qquad \textbf{5-26}$$

Determining the C.G. location of each component is difficult since the exact weight distribution of each component in unknown. A large statistical database of existing longitudinal C.G. locations within the components is therefore used, see Table 5-6. Please note that the cited values in Table 5-6 are measured from the front of the corresponding component. When no longitudinal C.G. location is available, a value of 40% of the component length is assumed **[29]**. Avionics, payload and landing gear weights are assumed to have the same C.G. location as the fuselage. The longitudinal C.G. location of the engine is based on the fact that the engine is a pusher engine configuration with gearbox and propeller located at the back. The C.G. along the normal axis is assumed to be in the midpoint of each component, except for the vertical tail, which uses the C.G. of a trapezoid along the normal axis.

Table 5-6: Component Longitudinal Center of Gravity Location [29]

	Torenbeek	Raymer	Stinton	Roskam
Wing	38-42%	40%	40%	38-42%
Fuselage	/	40-50%	40%	/
Horizontal Tail	42%	40%	/	42%
Vertical Tail	42%	40%	/	42%
Engine	/	40-50%	40%	/

5.2 Aerodynamic Properties

A prerequisite to the aircraft performance analysis is the ability to calculate the lift and drag forces, hence lift and drag coefficients, at different altitudes, velocities and aircraft configurations. Several methods exist to model the aerodynamic characteristics of an aircraft, each having different levels of complexity and computation times (e.g. empirical relations, Vortex Lattice Method, Euler equations and Navier-Stokes equations) **[45]**. For this Master thesis it was opted to use a combination of empirical relations and a Vortex Lattice Method (VLM). The combination of these methods gives an acceptable model accuracy with a relative small computation effort and timeframe **[46]**. Euler and Navier-Stokes equations can be time consuming and require higher computation power compared to other methods. VLM is therefore often used during the early design phase to obtain the aerodynamic characteristics. It is an extended model of Prandtl's classical lifting line theory **[46]**. A number of lifting panels are placed on the lifting surfaces, each containing a single horseshoe vortex. The entire wing is covered by a lattice of horseshoe vortices, each having a different unknown strength Γ_n. A control point is placed on each panel. One can calculate the normal velocity induced by all vortices using the Biot-Savart law at any control point. A set of algebraic equations can be created by applying the flow-tangency condition at all control points. This set of equations can be solved for all the unknown Γ_n in order to calculate the lift and drag coefficients. Some disadvantages of using VLM are however unavoidable. The method can only be used for incompressible and inviscid flows, since it is built on the potential flow which neglects viscous effects **[46]**. The empirical relations are therefore necessary since VLM cannot estimate the viscous drag of a model. This results in a less accurate determination of the aerodynamic characteristics. The accuracy of the model is however large enough to satisfy the goals of the conceptual design process. Several VLM software packages are available (AVL, Tornado and Vlaero+ to only name a few). The Tornado software package is selected based on the user-friendly interface, relative small learning curve and availability.

The total drag coefficient is determined using the drag polar equation, see equation 5-27. It is build up from three components; the zero-lift drag or parasite drag coefficient (C_{D_0}), the lift dependent drag or induced drag coefficient (C_{D_i}) and the wave drag coefficient (C_{D_w}). The airspeed of the UAV is however below Mach 0.3, which implies that the UAV operates in the subsonic flow regime. The wave drag component is therefore negligible. A VLM program is used to determine the lift coefficient while empirical relations are used to determine the parasite drag component. The span efficiency factor or Oswald factor (e) is also determined using an empirical relation.

$$C_D = C_{D_0} + C_{D_i} + C_{D_w} = C_{D_0} + \frac{{C_L}^2}{\pi \cdot AR \cdot e} + C_{D_w} \qquad \textbf{5-27}$$

The drag and lift coefficients depend on UAV configuration changes caused by the landing gear and flap settings. Three different UAV configurations are identified: take-off, cruise and landing. The take-off setting has a flap deflection angle of 5° and the landing gear is deployed. The cruise setting is the clean configuration, no flap deflection and the landing gear is retracted. The landing setting has a flap deflection of 20° and the landing gear is again deployed.

5.2.1 Lift Coefficient

The lift coefficient is modeled in Tornado, this includes the main wing, horizontal tail and two vertical tails, see Figure 5-1. The flap settings are also modeled in order to provide the lift coefficient at different flap settings. The result of Tornado are $C_L - \alpha$ graphs for each flap setting, which are given in Chapter 6. The required input used by Tornado can be found in Appendix F - Tornado Input.

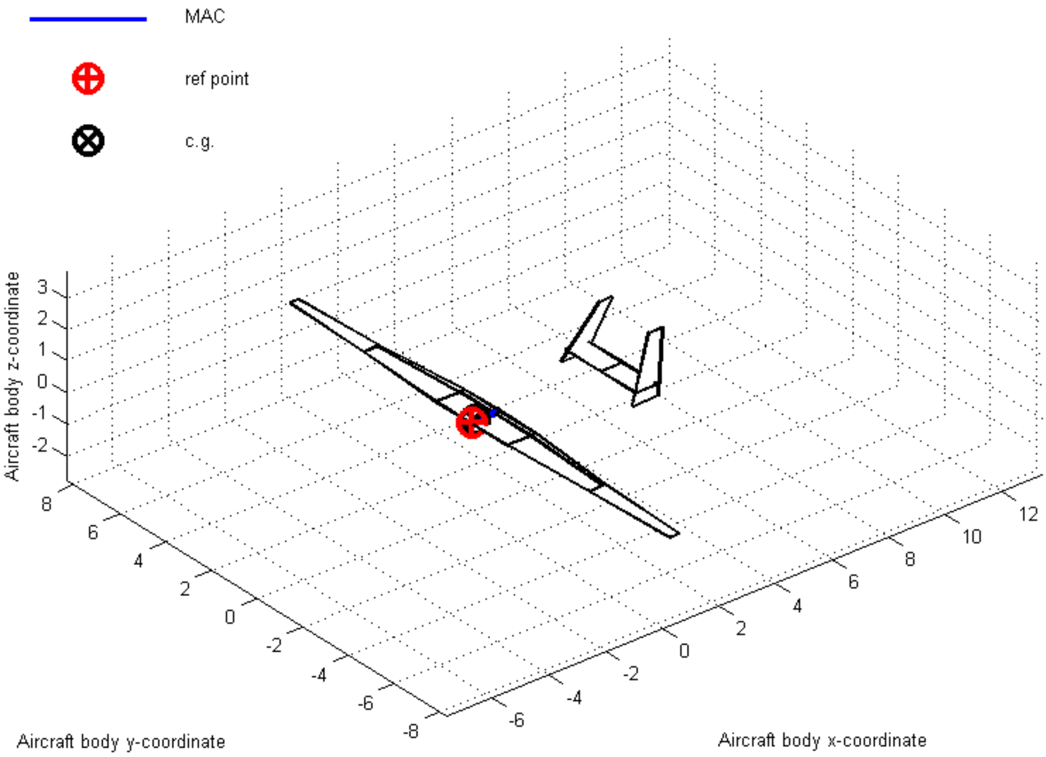

Figure 5-1: Tornado Geometry Input

The number of panels used to cover each lifting surface and the panel distribution can however affect the results. Especially if too few panels are used, leading to erroneous results. This can also occur if the number of panels becomes too high which also increases the computation time. It is therefore important to verify if the number of panels is adequate. A verification of the number of panels and their distribution is therefore given in Section 6.6.

5.2.2 Zero-Lift Drag Coefficient

The zero-lift drag is estimated using the component build-up technique relying mainly on empirical formulas. Each external component (wing, horizontal & vertical tail, fuselage, tail booms, flaps, landing gear and miscellaneous items) of the UAV has a certain drag contribution which needs to be taken into account to estimate the total zero-lift drag coefficient. The wing, fuselage, tail booms and horizontal & vertical tail zero-lift coefficients are calculated using the thin plate approximation (equation 5-28). This approximation assumes that each component is modeled as a thin flat plate with a certain skin friction coefficient C_f. A form factor (FF) compensates for the actual shape of the component, accounting for super velocities and pressure drag resulting from the component shape. An interference factor (Q) is also taken into account to represent the interference between the various components. S_{Wet} is the wetted area of the component while S_{ref} is a reference Area. This reference area acts simply as a base or reference and can be arbitrarily specified, as long as it is used consistently. It is a measure of the relative size of each component compared to other components. The wing planform area is commonly selected as reference area.

$$C_{D_0} = \frac{C_f \cdot FF \cdot Q \cdot S_{Wet}}{S_{ref}} \quad \textbf{5-28}$$

The skin friction coefficient depends on the boundary layer conditions. The airflow over a thin plate however always starts with laminar flow at the leading edge. At some point downstream of the leading edge transition from laminar to turbulent occurs. This transition point can be calculated by dividing the critical Reynolds number ($\mathrm{Re}_{\mathrm{cr}} = 500{,}000$) by the Reynolds number of the component ($\mathrm{Re}_{\mathrm{comp}}$), see equation 5-29. The critical Reynolds number can differ significantly depending on the component and flow properties but is difficult to estimate. Therefore the sensitivity of the critical Reynolds number is investigated in Chapter 7. The Reynolds number of the component can be calculated using equation 5-30, where l_{comp} is the length of the component (fuselage length or mean aerodynamic chord for lifting surfaces).

$$x/c_{trans} = \frac{Re_{cr}}{Re} \quad \textbf{5-29}$$

$$Re_{comp} = \frac{\rho \cdot V_{eff} \cdot l_{comp}}{\mu} \quad \textbf{5-30}$$

The laminar flow coefficient is calculated using equation 5-31. Unfortunately, no exact analytical solution for calculating the turbulent skin friction coefficient exists. Different methods are available depending on the Reynolds number, see Figure 5-2. This Master thesis uses equation 5-32. The result of this equation is compared to other methods in Section 6.6. The total skin friction coefficient can know be calculated using equation 5-33.

$$C_{f_{lam}} = \frac{1.328}{\sqrt{Re_{comp}}} \quad \textbf{5-31}$$

$$C_{f_{turb}} \approx \frac{0.074}{{Re_{comp}}^{0.2}} \quad \textbf{5-32}$$

$$C_f = x/c_{trans} \cdot C_{f_{lam}} + C_{f,tur} - x/c_{trans} \cdot C_{f_{turb}} \quad \textbf{5-33}$$

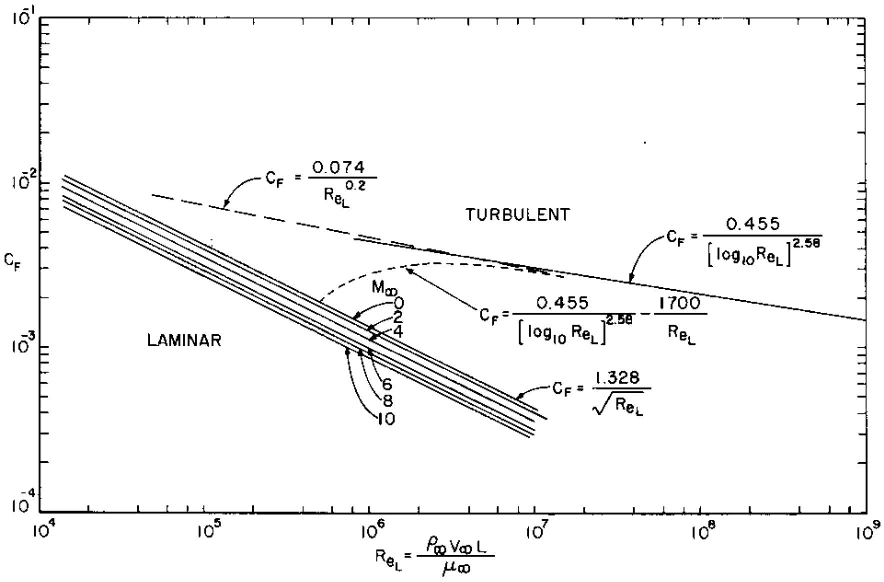

Figure 5-2: Skin Friction Coefficient in Function of Reynolds Number [47]

The form factor of each component is estimated using empirical models **[48]**. Several equations of different authors are used to increase the accuracy. From these results an un-weighted average is calculated for the component in question. Table 5-7 lists four form factors used for the lifting surfaces (wing, horizontal and vertical tail).

Table 5-7: Different Form Factors for Wing, Horizontal and Vertical Tail

Author	Form Factor	
Raymer **[23]**	$FF_{Wing} = \left[1 + \frac{0.6}{(x/c)_{max}}\left(\frac{t}{c}\right) + 100\left(\frac{t}{c}\right)^4\right]\left[1.34M^{0.18}(\cos\Lambda_{max})^{0.28}\right]$	**5-34**
Hoerner **[49]**	$FF_{Wing} = 1 + 2\cdot\frac{t}{c} + 60\cdot\left(\frac{t}{c}\right)^4$	**5-35**
Torenbeek **[25]**	$FF_{Wing} = 1 + 2.7\cdot\frac{t}{c} + 100\cdot\left(\frac{t}{c}\right)^4$	**5-36**
Shevell **[50]**	$FF_{Wing} = 1 + \frac{(2-M^2)\cdot\cos\Lambda_{0.25}}{\sqrt{1-M^2\cdot\cos^2\Lambda_{0.25}}}\cdot\frac{t}{c} + 100\cdot\left(\frac{t}{c}\right)^4$	**5-37**

The form factors used for the bodies of revolution, the fuselage and booms, are given in Table 5-8. Five different equations are available. The body fineness ratio, l/d, is defined as the ratio between the body length and the maximum body diameter.

Table 5-8: Different Form Factors used for Fuselage and Booms

Author	Form Factor	
Raymer **[23]**	$FF_{Fus} = 1 + \frac{60}{(l/d)^3} + \frac{l/d}{400}$	**5-38**
Hoerner **[49]**	$FF_{Fus} = 1 + \frac{1.5}{(l/d)^{1.5}} + \frac{7}{(l/d)^3}$	**5-39**
Torenbeek **[25]**	$FF_{Fus} = 1 + \frac{2.2}{(l/d)^{1.5}} + \frac{3.8}{(l/d)^3}$	**5-40**
Shevell **[50]**	$FF_{Fus} = 1 + 1 + \frac{2.8}{(l/d)^{1.5}} + \frac{3.8}{(l/d)^3}$	**5-41**
Nicolai/Jobe **[44,51]**	$FF_{Fus} = 1 + 0.0025\cdot(l/d) + \frac{60}{(l/d)^3}$	**5-42**

The mutual interference between the different components creates a contribution toward the zero-lift drag coefficient. This contribution is estimated by specifying an interference factor for the different components. Table 5-9 lists the interference factors for each component.

Table 5-9: Component Interference Factors [28]

Component	Interference Factor
Q_{Wing}	1
Q_{Fus}	1
Q_{HT}	1.05
Q_{VT}	1.05

The final factor in order to calculate the zero-lift drag of each component is the wetted area. This is the area that is submerged into the flow. Equations 5-43 and 5-44 are used to estimate the wetted areas of the lifting surfaces (wing, horizontal & vertical tail) and the bodies of revolution (fuselage and booms). The estimation of the top and side areas of the fuselage and booms is given in Figure 5-3.

$$S_{Wet,Wing} = 2\cdot\left(1 + 0.2\cdot\frac{t}{c}\right)S_{ref} \quad \textbf{5-43}$$

$$\mathrm{S_{Wet,Fus}} = 3.4\cdot\left(\frac{\mathrm{S_{Fus_{top}}} + \mathrm{S_{Fus_{side}}}}{2}\right) \quad \textbf{5-44}$$

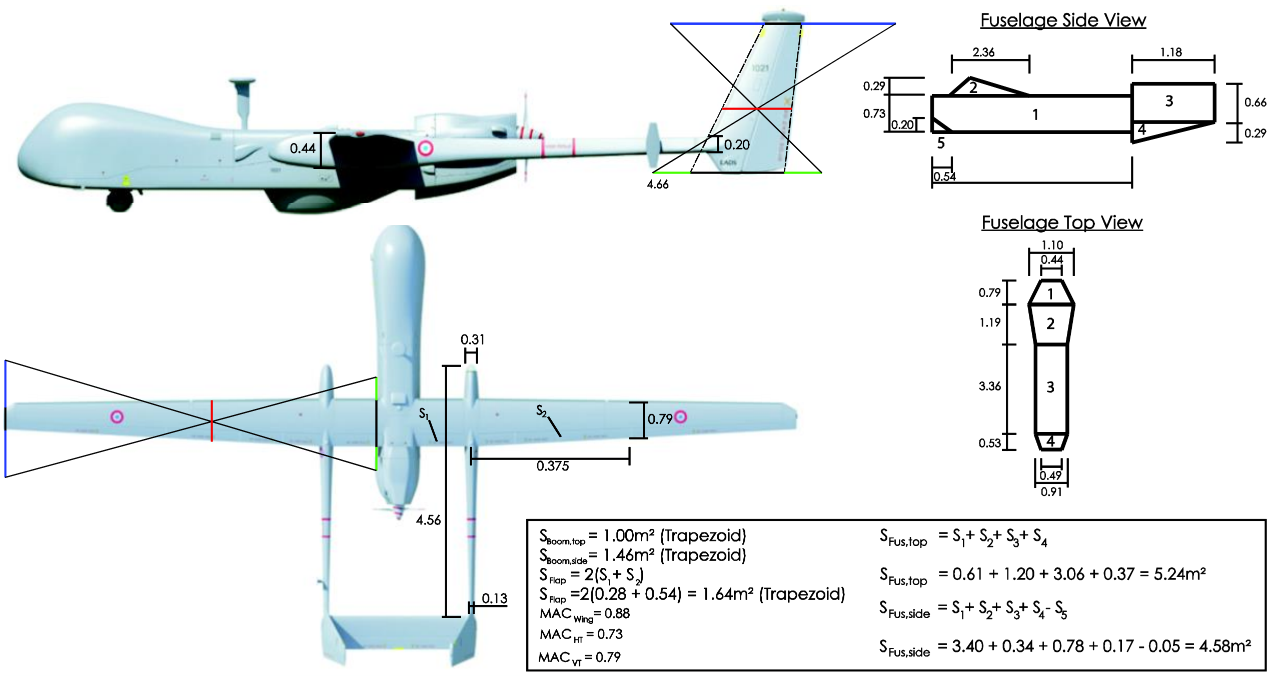

Figure 5-3: Mean Aerodynamic Chord and Fuselage, Boom & Flap Area

The increase in the zero-lift drag coefficient due to the flaps can be determined by equation 5-45 **[52].** The flaps span over the full length of the unswept wing section and the inner half of the swept wing section. A_{flap} and B_{flap} represent flap coefficients based on the type of flap system ($A_{flap} = 0.0014$ and $B_{flap} = 1.5$ for plain flaps, refer to **[52]** for other flap types). The flap over wing chord fraction is equal to 0.18, see Figure 4-1. The flap area is calculated in Figure 5-3.

$$C_{D_{0\,Flap}} = A_{Flap} \frac{c_{Flap}}{c_{Wing}} \cdot \frac{S_{Flap}}{S_{ref}} \cdot \left(\delta_{Flap}\right)^{B_{Flap}} \qquad \textbf{5-45}$$

The landing gear drag coefficient is split up into the drag due to the wheel and the strut, see equation 5-46. $\mathrm{C_{D_{Wheel}}}$ and $\mathrm{C_{D_{Strut}}}$ are the drag coefficients of the wheel and strut which are both equal to 0.3. The frontal area of the wheel and strut is simply the diameter multiplied by the width. These dimensions can be found in Figure 4-1. Please note that the baseline UAV has a tricycle landing gear arrangement.

$$C_{D_{0\,LG}} = C_{D_{Wheel}} \cdot \frac{S_{frontal,Wheel}}{S_{ref}} + C_{D_{Strut}} \cdot \frac{S_{frontal,Strut}}{S_{ref}} \qquad \textbf{5-46}$$

The total zero-lift drag coefficient can now be calculated by adding $\mathrm{C_{D_0}}$ of all aircraft components together, see equation 5-47. A correction factor (K_c) of 1.2 is introduced to account for miscellaneous drag components like: antennas, rivets and screws, gaps, surface roughness and measuring devices **[52].**

$$C_{D_0} = K_C \left[C_{D_{0\,Wing}} + C_{D_{0\,HT}} + 2 \cdot C_{D_{0\,VT}} + C_{D_{0\,Fus}} + 2 \cdot C_{D_{0\,Boom}} + C_{D_{0\,Flap}} + C_{D_{0\,NG}} + 2 \cdot C_{D_{0\,MG}} \right] \qquad \textbf{5-47}$$

5.2.3 Induced Drag Coefficient

The induced drag coefficient is calculated using equation 5-27. The lift coefficient is obtained with Tornado, see Section 5.2.1. The Oswald factor or span efficiency factor (e) is estimated using equation 5-48. The aspect ratio is given in Figure 4-1.

$$e = 1.78 \cdot (1 - 0.045 \cdot AR^{0.68}) - 0.64 \qquad \textbf{5-48}$$

The induced drag factor (k), see equation 5-49, is influenced by the ground effect. This ground effect can be explained as a reduction in the induced downwash angle and is encountered when the wing is close to the ground ($h < 50m$). The ground effect is represented by multiplying a ground effect factor, F_{GE}, (equation 5-50) with the induced drag factor. This ground effect reduces the induced drag coefficient.

$$k = \frac{1}{\pi \cdot AR \cdot e} \tag{5-49}$$

$$F_{GE} = \frac{33 \cdot \left(h_g/b\right)^{1.5}}{1 + 33 \cdot \left(h_g/b\right)^{1.5}} \tag{5-50}$$

5.3 Propulsion Modeling

The goal of the propulsion analysis is to obtain the thrust and fuel consumption at different velocities, heights and engine settings. The thrust of the reciprocating engine is calculated using the actuator disk theory or ideal propeller theory, see equation 5-51, assuming a fixed pitch propeller. The fuel flow follows from the power output at specific operating conditions. The propeller propulsion efficiency (η_{Prop}) is the product of the Froude efficiency (η_{Fr}) and an axial flow energy transformation efficiency ($\eta_{kin,x}$). The Froude efficiency is calculated using equation 5-52, wherein the jet velocity (V_j) is determined by solving equation 5-53. For ideal propellers $\eta_{kin,x} = 1$, real propellers have a lower value due to the swirl and profile drag. An algorithm is therefore included to select a user-specified efficiency or the Froude efficiency as η_{Prop}, whichever is the lowest one. This is required to truncate the Froude efficiency in order to exclude unrealistic high propeller propulsion efficiencies.

$$T = \frac{P \cdot \eta_{Prop}}{V_0} \tag{5-51}$$

$$\eta_{Fr} = \frac{2}{1 + \frac{V_j}{V_0}} \tag{5-52}$$

$$P = \rho \cdot S_{prop} \cdot \left(V_j + V_0\right) \frac{\left(V_j^{\,2} - V_0^{\,2}\right)}{4} \tag{5-53}$$

Equation 5-51 is however not applicable for standstill and low flight speeds due to singularity problems. Therefore equation 5-54 is used which gives the static thrust at standstill. The static thrust equation is used until the advance ratio, J, becomes higher than 0.2 (equation 5-55). Please note that n_{prop} represents the propeller rotational speed in revolutions per time unit. The engine rpm should therefore be divided by the gear box ratio of the engine, defined in Section 4.1.

$$T_{st} = \left(\sqrt{\frac{\pi}{2}} \cdot \sqrt{\rho_0} \cdot d_{prop} \cdot \eta_{Prop} \cdot P\right)^{2/3} \tag{5-54}$$

$$J = \frac{V_0}{d_{prop} \cdot n_{prop}} \tag{5-55}$$

The power output of the reciprocating engine is determined using data from the manufacturer. Figure 5-4 gives the power output as a function of rpm at sea level conditions. This power curve is altitude correct using Figure 5-5 which relates the decrease in power by increasing altitude. One can conclude from this figure that the power decreases 2% per 2000 ft until it reaches 15000 ft, the critical altitude of the turbo. From this altitude onwards power decreases with 5% per 2000 ft increase.

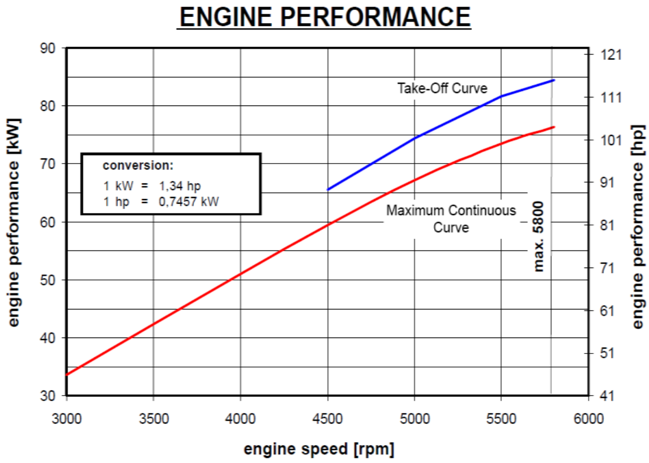

Figure 5-4: Rotax 914 Power a as Function of rpm at Sea Level [53]

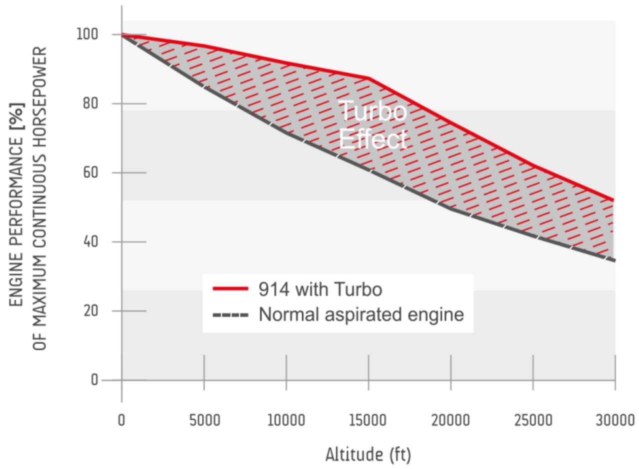

Figure 5-5: Turbo Effect at Altitude of the Rotax 914 [54]

Different power settings are used to simulate the mission. The engine can operate for a maximum of 5 minutes at a maximum rpm of 5800 which is used during take-off. The climb setting of the engine corresponds with the maximum rpm for continues operations; 5500 rpm giving 73.5 kW of power at sea level. The minimal rotation speed of the engine is 2000 rpm and is used during idle engine operations. Please note that the engine setting for level flight is set at a value between idle and maximum continuous power to maintain level flight. The specific fuel flow of the reciprocating engine increases as engine rpm decreases, see Figure 5-6. This figure is based on the fuel consumption (l/h) as a function of rpm, at sea level conditions; and a fuel density of 720 kg/m³. Multiplying the SFC by the altitude corrected power gives fuel flow in g/s.

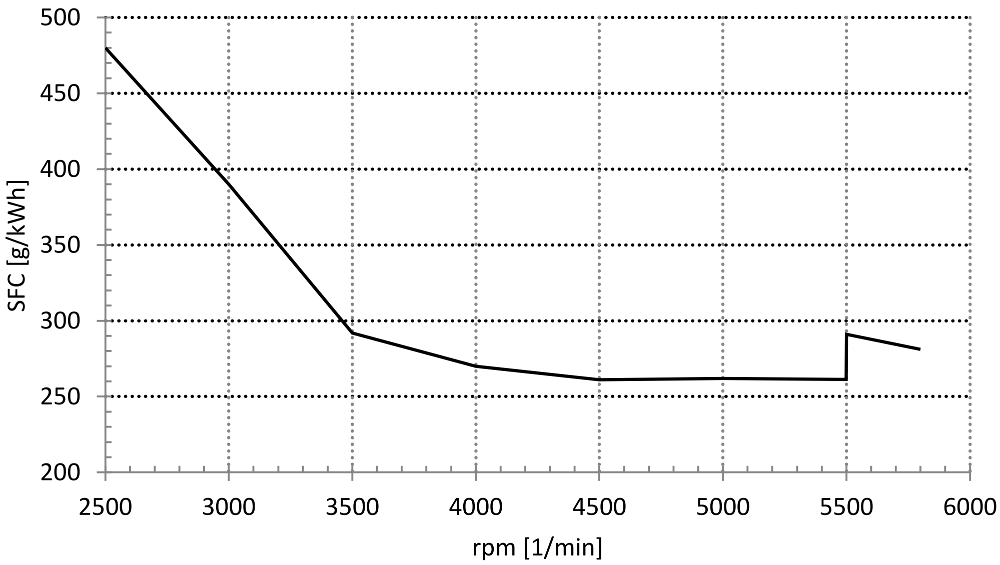

Figure 5-6: Specific Fuel Consumption as Function of rpm - Rotax 914 [53]

The analysis of the MGT is part of another Master thesis **[5]**. This project models the different MGTs using the Gas turbine Simulation Program (GSP) developed by NLR. GSP is a component based modeling environment which provides thrust management tables including fuel flow and thrust data at different velocities, altitude and engine settings **[55]**. The data can readily be implemented since an altitude correction is already taken into account as is the propeller model.

5.4 Flight Performance Analysis

The flight performance relates to the translational motion of flight vehicles. The theory of point performance is applied to determine the performance of the UAV at a given point in time during the mission **[39]**. The total mission performance is obtained by integrating the point performance to path performance. The aircraft is assumed to be a point mass, see Section 4.3. The aircraft motion can therefore be divided into translational and rotational motion around the body axis of the aircraft. Rotation along the normal axis is not taken into account, while rotation along the lateral axis only occurs during the loiter phase. The point performance is obtained using the Equations of Motion (E.O.M.) of each mission phase which follows from the free body diagrams of each mission phase **[39]**. The forces (lift, drag, thrust and weight) on the free body diagrams are, depending on the mission phase, determined using the analyses of Section 5.1 through 5.3. The integration into path performance is done using Euler integration. The initial point performance of a mission phase is defined by the end point of the pervious mission phase, or the initial starting values in case of the take-off phase. Next, the change in velocity, height, distance, weight and aircraft angles per time unit is determined and added to the initial point performance. This process is repeated until the end point of the mission phase in question is reached. A smaller time step results in a higher accuracy but lengthens the computation time. Different Matlab scripts have been developed to model each phase in combination with supporting scripts (e.g.: loading data, modeling standard atmosphere and calculating drag coefficients). The flowcharts of each Matlab script used for the different mission phases can be found in Appendix G - Flowcharts Mission Simulation. Each script starts with loading the engine, aerodynamic, aircraft and atmosphere properties followed by loading the phase specific parameters (time step, flap setting and flying strategy) and the state variables (time, height, distance, velocity, weight and aircraft angles). Next, the different E.O.M. are used calculating the required output in order to continue to the following point. Section 5.4.1 to 5.4.8 discuss the flight performance of the different mission phases according to Ruijgrok **[39]**.

5.4.1 Take-Off

The take-off maneuver is defined by a UAV that accelerates from rest to an initial climb until it reaches a screen height of 15.2 m (50 ft). The maneuver consists out of two segments: the ground run and the airborne phase. The power is set to deliver maximum thrust for the entire duration of the maneuver while the flaps are set to the take-off setting of 5°, with the landing gear deployed. A range of different pitch angles and rotation speeds, defined by the user, are modeled to determine the combination which results in the shortest take-off distance. The minimum rotation speed is determined using equation 5-56. The pitch angle is increased to the desired pitch angle, using a delay curve of 3 seconds, as soon as the desired rotation speed is reached. Once the desired pitch angle is reached the flight mode changes to the airborne phase where the ground drag, $\mathrm{D_g}$, is set to zero. The lift coefficient is calculated based on the angle of attack and is used to calculate the drag coefficient. Thrust and fuel consumption follows from the take-off engine setting. The velocity and flight path derivatives can be calculated using the E.O.M. for take-off, see equations 5-57 and 5-58.

$$V_{R,min} = \sqrt{\frac{2 \cdot W}{\rho \cdot S_W \cdot C_{L,max,5}}} \qquad \textbf{5-56}$$

$$\frac{dV}{dt} = \frac{g}{W}\left[T - D - W \cdot \sin\gamma - D_g\right] \; with \; D_g = N_g \cdot \mu \qquad \textbf{5-57}$$

$$\frac{d\gamma}{dt} = \frac{g}{W} \cdot V\left[L - W \cdot \cos\gamma + N_g\right] \; with \; N_g = W - L \qquad \textbf{5-58}$$

The height and distance derivatives are calculated using equation 5-59 and 5-60. Please note that the take-off phase continues until a user-specified time, this to allow for an initial climb at full power. The decrease in gross weight is determined using equation 5-61 and is also used during the other mission phases.

$$\frac{dh}{dt} = V \cdot \sin\gamma \qquad \textbf{5-59}$$

$$\frac{ds}{dt} = V \cdot \cos\gamma \qquad \textbf{5-60}$$

$$\frac{dW}{dt} = \dot{m}_{Fuel} \cdot g \qquad \textbf{5-61}$$

5.4.2 Climb

Two different climb profiles are available: a 3 step climb profile and an optimum climb profile maximizing the rate of climb. Both profiles use the clean aircraft configuration (flaps = 0° and landing gear retracted). The 3 step climb profile divides the climb phase into 3 segments, each segment climbs at a user-specified velocity. The optimum climb profile on the other hand climbs at a velocity which results in the maximum rate of climb. This velocity is determined by calculating the difference between power available and required. The velocity at which this difference is the largest corresponds with the velocity for maximum rate of climb, see equation 5-62 and Figure 5-7.

$$RC_{max} = \frac{(P_a - P_r)_{max}}{W} \qquad \textbf{5-62}$$

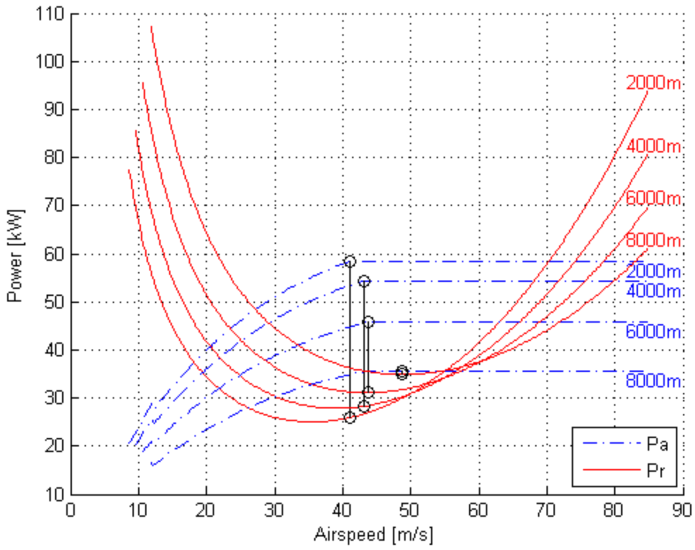

Figure 5-7: Maximum Rate of Climb as a Function of Altitude

Two different E.O.M. are used to model the climb. One to model the unsteady climb, if the desired climb velocity is not reached, see equation 5-63. And one to model the quasi-steady climb once the desired climb velocity is reached (equation 5-64). Height and distance derivatives are calculated with equation 5-59 and 5-60. The climb phase terminates once the desired cruise height is reached.

$$\gamma = \sin^{-1}\left(\frac{T-D}{2\cdot W}\right)\ with\ \gamma = \sin^{-1}\left(g\cdot\frac{dV}{dt}\right) \qquad \textbf{5-63}$$

$$\gamma = \sin^{-1}\left(\frac{T-D}{W}\right) \qquad \textbf{5-64}$$

5.4.3 Cruise

The cruise phase is the longest mission phase and therefore also consumes the majority of the fuel. Three different cruise profiles are available to the user: a fixed height and flight velocity cruise, optimum range cruise and an optimum endurance cruise. Each profile uses equation 5-65 as the E.O.M. for cruise. The required thrust is set between idle and maximum continuous power such that the level flight and desired cruise velocity is maintained, see equation 5-66.

$$L = W \Leftrightarrow C_L = \frac{2\cdot W}{\rho\cdot V^2\cdot S_W} \qquad \textbf{5-65}$$

$$T = D + \frac{W}{g}\frac{dV}{dt} + \frac{W}{V}\frac{dh}{dt} \qquad \textbf{5-66}$$

User-specified values for height and flight velocity are used during the fixed height and flight velocity profile. The optimum range profile flies at a velocity to maximize the cruising distance, see Figure 5-8 and at an AoA which maximizes C_L/C_D. The optimum endurance profile maximizes flight time by flying at a velocity corresponding with the minimum power required (Figure 5-8). The UAV must therefore fly at an AoA at which $C_L{}^3/C_D{}^2$ is maximum. These criteria are however based on the assumption of constant available power as a function of airspeed. The available power is however not constant as a function of airspeed, see Figure 5-7. The fuel consumption as a function of airspeed of both engine types is therefore depicted in Section 6.6 to verify this assumption. Both optimum cruise profiles are valid for a specific weight. However as fuel is consumed, airspeed should be steadily reduced if one wants to fly at a constant altitude. Or, if the airspeed is held constant, the cruising height must be gradually increased, commonly referred to as a cruise-climb flight. The latter option is selected for this mission. The increase in height is such that W/δ remains constant **[56]**. The relative ambient pressure (δ) must therefore decrease proportional to the aircraft gross weight.

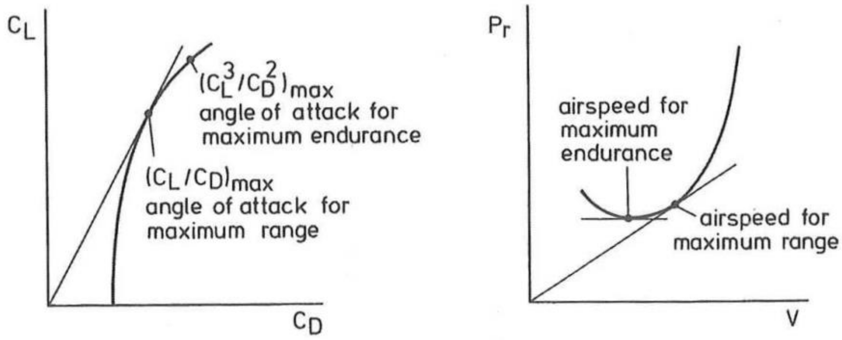

Figure 5-8: Optimum Endurance and Range in Level Flight for Propeller Aircraft [39]

5.4.4 Descent

Also the descent phase has three different profiles available: a 3 step descent, an optimum range descent and an optimum endurance descent. The 3 step descent is similar to the 3 step climb. The descent is split-up into 3 segments, each having a user-specified descent velocity while idle engine setting is selected. The negative flight path angle is calculated using equation 5-67.

$$\gamma = \sin^{-1}\left[\left(T - D - \frac{W}{g}\frac{dV}{dt}\right)\frac{1}{W}\right] \qquad \textbf{5-67}$$

The optimum range descent maximizes the traveled distance during the descent by flying at a velocity which gives the minimum descent angle (Figure 5-9). A minimum descent angle occurs when C_L/C_D is minimum. The optimum endurance descent on the other hand tries to maximize the descent time by minimizing the rate of descent, see Figure 5-9. A minimum rate of descent occurs at $C_L{}^3/C_D{}^2$. Thrust is set to idle ($T \neq 0$) for all three descent profiles.

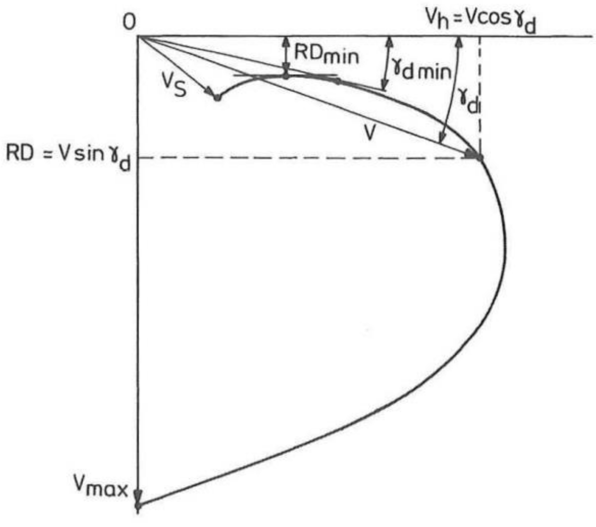

Figure 5-9: Hodograph Curve for Optimum Descent Profiles [39]

5.4.5 Loiter

The loiter phase performs rate-one ($\dot{\chi} = 3\,°/s$) or rate-two turns ($\dot{\chi} = 6\,°/s$) for a user-specified time. The turning maneuver is modeled as a steady curvilinear flight with banked wings and without a sideslip angle. A level-off maneuver is performed first since the UAV is still in a descending mode as it arrives at the loiter phase. The bank angle is increased to the desired value (equation 5-68) once the UAV has a level flight attitude. Equation 5-69 states the E.O.M. used to calculate the lift force during the turning maneuver while the velocity is determined using equation 5-70. The required thrust during the loiter phase is calculated, with a similar approach as in the cruise phase, using equation 5-66.

$$\Phi_{des} = \cos^{-1}\left(\frac{1}{n}\right) \; with\; n = \sqrt{\left(\frac{V^2}{R \cdot g}\right)^2 - 1} \qquad \textbf{5-68}$$

$$L = \frac{W}{\cos \Phi} \qquad \textbf{5-69}$$

$$V = \sqrt{\frac{2 \cdot n \cdot W}{\rho \cdot S_W \cdot C_L}} \qquad \textbf{5-70}$$

5.4.6 Approach

This phase consists out of three different parts: a descent, level flight and an approach part. The descent part is similar to the descent phase and is used to descent from the loiter height to the ILS interception height. Once this height is reached a level flight, similar to the fixed height and velocity profile of the cruise phase, is performed until the glide slope intersection point. During this phase the thrust is set between idle and maximum continuous to maintain level flight. The duration of this level flight phase is user-specified. The approach part starts with lowering the landing gear and setting the flaps to 20°. The approach speed is calculated using equation 5-71, while a flight path angle of -3° is selected. The thrust is set such that the approach speed and descent angle can be maintained using equation 5-66.

$$V_{Approach} = 1.3\sqrt{\frac{2 \cdot W}{\rho \cdot S_W \cdot C_{L_{\max 20}}}} \qquad \textbf{5-71}$$

5.4.7 Landing

The landing phase starts at a screen height of 15 m (50 ft) with the engine set to idle. The maneuver can be split up into four segments. A final approach, flare to go from a descending motion to a horizontal motion at ground level; a rotation phase to rotate the nose gear towards the runway and a ground run where braking is applied to come to a complete stop. The flare maneuver is modeled using an exponential function. Velocity and flight path derivatives are calculated using a similar E.O.M. as the take-off phase, although a negative braking force is added to the left hand side of the speed derivative equation (equations 5-56 and 5-58). This braking force is however simplified to advance the calculations, see Section 4.3. The landing maneuver, and also the entire mission, is ended when the velocity becomes zero.

5.4.8 Total Mission Simulation

Two different iteration algorithms are developed to model the complete mission. One iterates towards a user-specified total endurance. It first calculates the required time for the mission excluding the cruise phase. Extracting this time from the user-specified endurance results in an expected cruise time which is converted into an expected range using the average cruise speed. This process is repeated until the mission time converges to the user-specified time. The other algorithm iterates until all fuel is consumed. The fuel for the cruise is calculated by extracting the fuel use of the other phases from the total fuel weight. The expected cruise range follows from a combination with the average specific range during cruise. This is iterated until the used fuel converges to the maximum fuel weight. Flowcharts of both algorithms can also be found in Appendix G - Flowcharts Mission Simulation.

6
Results

The results of the different analyses of Chapter 5 are given in this Chapter. The selected flight performance profiles for this results chapter are: optimum climb, optimum cruise endurance and optimum descent endurance. A rate-one turn is performed during the loiter phase. Section 6.1 lists the results of the weight breakdown analysis while Section 6.2 and 6.3 give the results of the aerodynamic and propulsion analyses. Mission results of the baseline model powered by the reciprocating engine can be found in Section 6.4. A comparison of the mission results for the different engine types is given in Section 6.5. The verification process is discussed in Section 6.6.

6.1 Weight Breakdown Analysis

The weight breakdown analysis begins with the MTOW which differs for the various engines. The weight of each engine and the resulting MTOW is given in Table 6-1. The weight of the reciprocating engine is obtained using data from the engine manufacturer **[53]**. The weight of the different MGT sizes is determined in **[5]** using dedicated turbine WERs.

Table 6-1: Weight of the Different Engines and the Corresponding MTOW

Engine	Weight [kg]	Weight Reduction Compared to Rotax 914 [kg]	MTOW [kg]
Reciprocating Engine - 86 kW	74.7	/	1250
MGT - 86 kW	34	40.7	1209.3
MGT - 70 kW	29	45.7	1204.3
MGT - 60 kW	25	49.7	1200.3

Table 6-2 lists the results of the components WERs for the reciprocating engine. Please note that not every author has a WER for each component; and the weight of the vertical tails and booms are for two components each. Unrealistic results are removed from the analysis since they would otherwise offset the results. The resulting component weights are determined using an un-weighted average. The fuel and payload weight are added to determine the total weight.

Table 6-2: Results of Components WERs Reciprocating Engine in [kg]

	Wing	Fuselage	Horizontal Tail	Vertical Tails	Booms	Landing Gear	Fuel System	Avionics	Total
Gerard	261.02								
Torenbeek	159.01		~~23.00~~					118.14	
Yi	361.87	84.37				65.9			
Gundlach		~~186740~~			23.57	50	26.64	137.5	
Raymer (Fighter attack)		~~1170.7~~							
Raymer (GA)		15.55	3.43						
Howe (Single Engine)		32.37	4.61	7.38					
Palumbo			5.52	6.08					
Roskam			~~11.61~~					~~24.31~~	
Nicolai/Anderson				~~22.97~~					
Average	260.63	44.10	4.52	6.73		57.95		127.82	1219.7
Maximum	361.87	84.37	5.52	7.38	23.57	65.9	26.64	137.5	1380.4
Minimum	159.01	15.55	3.43	6.08		50		118.14	1070.1

The component weight breakdown results of the various MGT sizes and can be found in Appendix H - Weight Breakdown Analysis MGT. The average component weights are listed in Table 6-3.

Table 6-3: Average Component Weight per MGT Size in [kg]

Engine Size [kW]	Wing	Fuselage	Horizontal Tail	Vertical Tails	Booms	Landing Gear	Fuel System	Avionics	Total
86	252.91	43.19	4.49	6.72	23.48	56.23	26.64	123.96	1164.6
70	251.96	43.08	4.49	6.72	23.47	56.02	26.64	123.48	1157.9
60	251.20	42.99	4.49	6.72	23.46	56.85	26.64	123.10	1152.4

The average component weights in combination with equation 5-26 and the components C.G. locations (Table 6-4) give the UAV C.G. coordinates. These coordinates are measured from the nose and below the UAV. Only a small shift in C.G. is present between the reciprocating engine and the MGT. The shift in C.G. between the different MGT sizes is negligible.

Table 6-4: Selected Longitudinal C.G. Location of Components

Component	Selected Location
Wing	40%
Fuselage	40%
Horizontal Tail	42%
Vertical Tail	42%
Engine	50%

- UAV with reciprocating engine: $[X_{cg}, Y_{cg}, Z_{cg}] = [3.54\ 0\ 0.48]$
- UAV with 86 kW MGT: $[X_{cg}, Y_{cg}, Z_{cg}] = [3.47\ 0\ 0.47]$
- UAV with 70 kW MGT: $[X_{cg}, Y_{cg}, Z_{cg}] = [3.46\ 0\ 0.47]$
- UAV with 60 kW MGT: $[X_{cg}, Y_{cg}, Z_{cg}] = [3.46\ 0\ 0.47]$

6.2 Aerodynamic Analysis

The results of the aerodynamic analysis are not influenced by the engine type, since MTOW is not taken into account during the determination of lift and drag coefficients. Figure 6-1 shows the lift coefficient as a function of alpha for the different flap settings. The maximum lift coefficient is determined by Tornado using the maximum lift coefficient of the airfoil (NACA 6414-43) obtained from Javafoil. The lift coefficient during the ground roll is assumed at $\alpha = -3$: $C_{L_{GR,0}} = 0.28$; $C_{L_{GR,5}} = 0.45$; $C_{L_{GR,20}} = 0.96$.

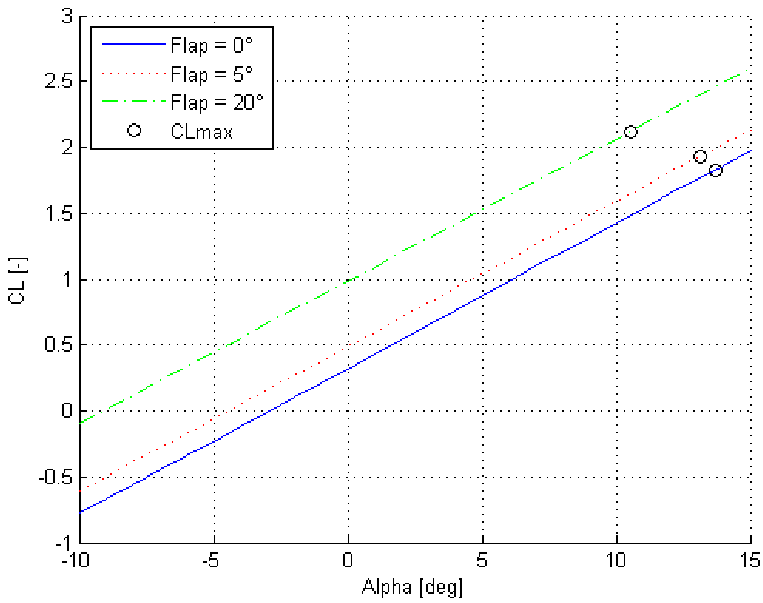

Figure 6-1: $C_L - \alpha$ Graph for Different Flap Settings

The form factors, used to determine C_{D_0}, of different authors for each component are listed in Table 6-5. An un-weighted average is used to calculate the resulting form factors.

Table 6-5: Form Factors of Each Component

	Wing	Horizontal Tail	Vertical Tail	Fuselage	Booms
Raymer	1.28	1.20	1.21	1.41	1.06
Hoerner	1.30	1.25	1.25	1.17	1.03
Torenbeek	1.42	1.34	1.34	1.21	1.04
Shevell	1.32	1.26	1.24	1.25	1.05
Nicolai/Jobe	/	/	/	1.41	1.06
Average	**1.33**	**1.27**	**1.26**	**1.29**	**1.05**

The skin friction coefficient of each component can be found in Table 6-6, together with the wetted area, Reynolds number and the transition point as a percentage of the component length.

Table 6-6: Skin Friction Coefficient of Each Component

	Wetted Area [m²]	Reynolds Number	Transition Point [%]	$C_{f_{lam}}$	$C_{f_{tur}}$	C_f
Wing	26.01	3404500	14.69	0.00072	0.0037	0.0032
Horizontal Tail	4.63	2824200	17.7	0.00079	0.0038	0.0033
Vertical Tail	2.55	3056300	16.36	0.00076	0.0037	0.0032
Fuselage	16.69	2259400	2.21	0.00028	0.0025	0.0025
Boom	4.18	1764200	2.83	0.00032	0.0026	0.0026

Table 6-7 lists the C_{D_0} of the various components and the different flap settings ($\delta_{flap} = 0°$ does not contribute to C_{D_0}). From this table it becomes clear that the flaps and fuselage create the largest contribution towards C_{D_0}. The drag coefficient of the vertical tail and boom is for one component and is therefore taking twice into account during the determination of the total zero-lift coefficient.

Table 6-7: Zero-Lift Coefficients for Each Component

Component	Zero-lift coefficient
Wing	0.0082
Horizontal Tail	0.0015
Vertical Tail	0.00081
Fuselage	0.0039
Boom	0.00083
Landing Gear	0.0084
Flaps 5	0.0039
Flaps 20	0.0312

The total zero-lift drag coefficient is estimated using the component build-up technique. The results of each configuration setting can be found in Table 6-8. The cruise setting has a clean configuration with the landing gear and flaps retracted. The take-off setting has a flap setting of 5° and landing gear deployed. The landing setting also has the landing gear deployed but the flap setting is increased to 20°. This also gives the highest C_{D_0} which is 3 times as high as the clean configuration. The total drag coefficient is calculated using the zero-lift drag coefficient, lift coefficient and an Oswald factor of $e = 0.52$. The estimation of the Oswald factor results in a lower value than anticipated. The sensitivity analysis, see Section 7.3, therefore investigates the influence of this value and the estimation method is highlighted as a point for future research. C_D as a function of AoA and C_L is given in Figure 6-2.

Table 6-8: Configuration Zero-Lift Coefficients

Configuration	C_{D_0}
$C_{D_{0,crz}}$	0.0203
$C_{D_{0,TO}}$	0.0350
$C_{D_{0,LND}}$	0.0677

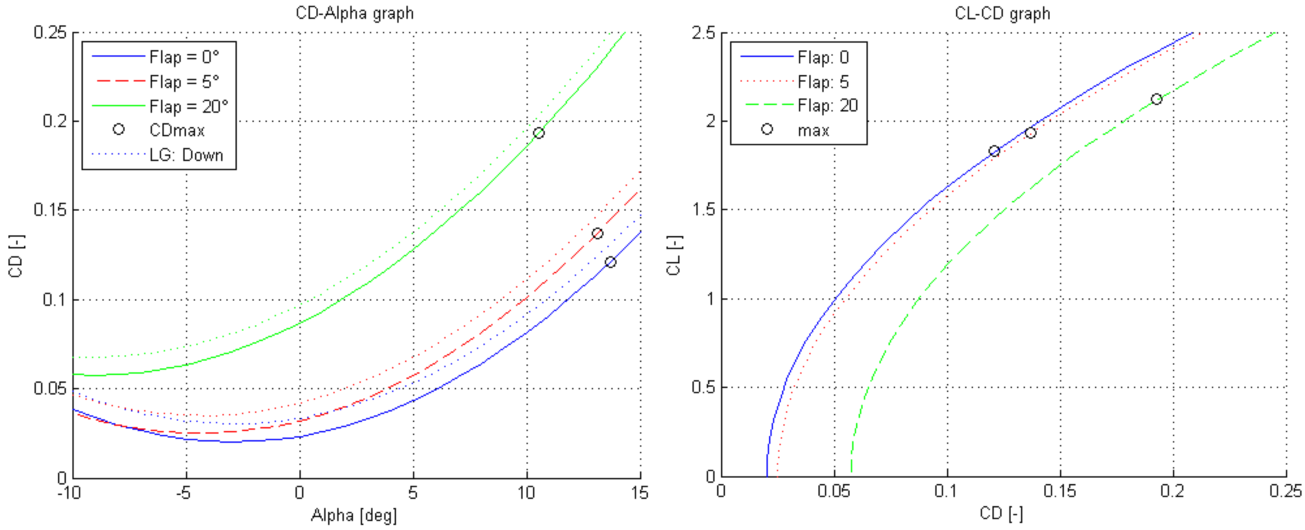

Figure 6-2: C_D Graphs for Different Configurations

The influence of the ground effect on the induced drag factor (k) is depicted in Figure 6-3. The ground effect is not taken into account above an altitude of 50 m. $\mathrm{k} = 0.014$ during the take-off ground run.

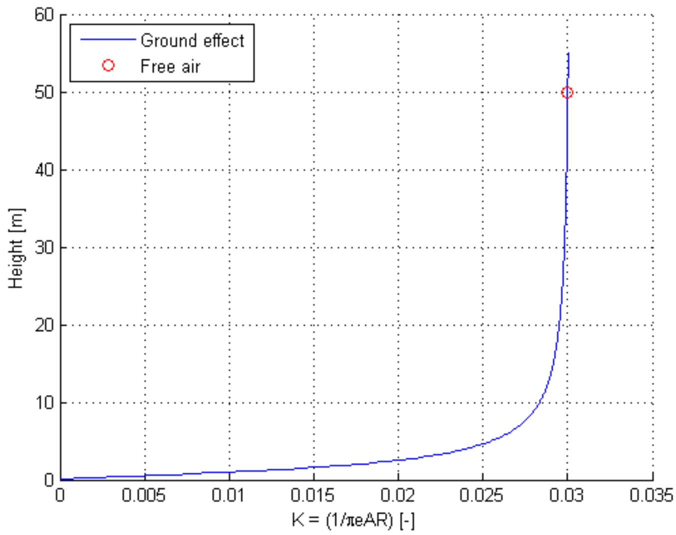

Figure 6-3: Induced Drag Factor with Ground Effect

6.3 Propulsion Analysis

The main outputs of the propulsion analysis are thrust and fuel consumption at a given altitude, velocity and engine setting. The reader is referred to **[5]** for more detailed information about the propulsion data of the MGTs. Figure 6-4 to Figure 6-6 give the thrust at take-off for the 86, 70 and 60 kW MGTs at different technology levels with respect to the reciprocating engine. All 86 kW MGTs produce more thrust during take-off than the reciprocating engine. The net thrust increases as the technology level of the engine is increased, especially if the TIT increases. The 70 kW MGT on the other hand produces less thrust compared to the reciprocating engine, except if technology level 3 is applied. The 70 kW MGT - TL 3 gives a similar thrust output as the reciprocating engine. The thrust of the MGT decreases even more for the 60 kW turbine. However, higher thrust can again be obtained if technology level increases. None of the 60 kW MGTs produces more thrust than the reciprocating engine. This indicates that reducing the MGT even more would result in an underperforming turbine, since the 60 kW MGT - TL 2 already produces 350 to 250 N less thrust at take-off.

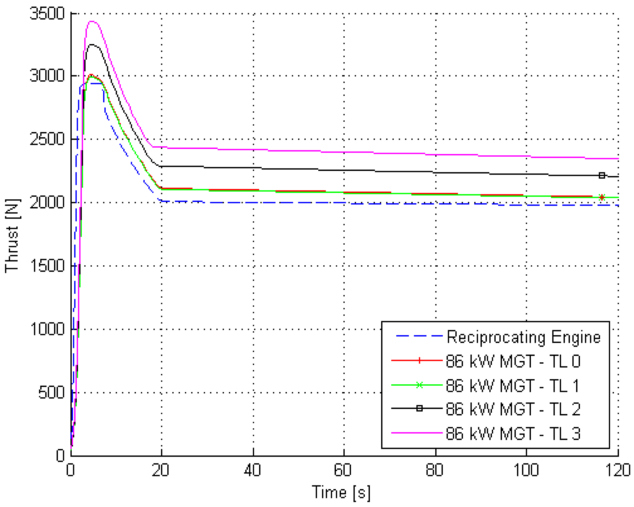

Figure 6-4: Thrust at Take-off: 86 kW MGT

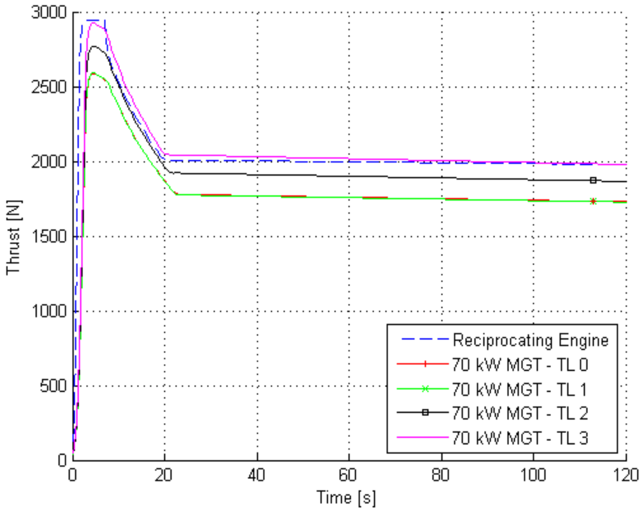

Figure 6-5: Thrust at Take-off: 70 kW MGT

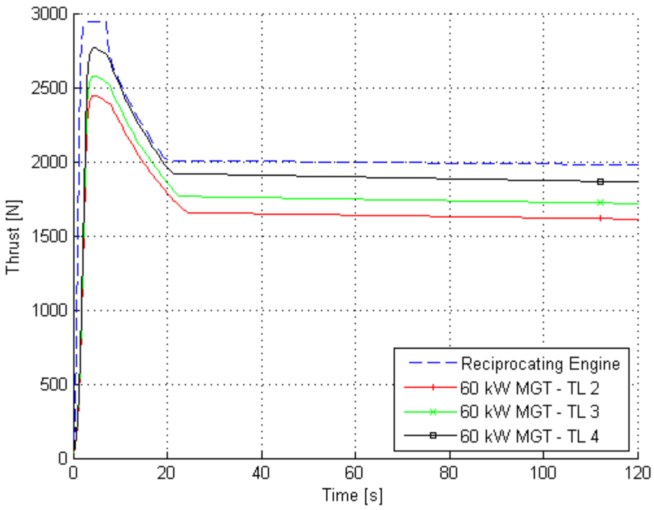

Figure 6-6: Thrust at Take-off: 60 kW MGT

The maximum fuel consumption during take-off for the different engine types is given in Table 6-9. None of the MGTs have better specific fuel consumption than the reciprocating engine. The fuel consumption of the 86 kW MGT is almost twice as high. The fuel consumption does however decrease if the MGT size is reduced.

Table 6-9: Fuel Consumption [g/s] during Take-Off

	Reciprocating engine	86 kW MGT	70 kW MGT	60 kW MGT
TL 0		12.56	10.12	/
TL 1		11.47	9.41	/
TL 2	6.60	12.04	9.90	8.44
TL 3		12.55	10.32	8.79
TL 4		/	/	8.90

Thrust during climb phase, using the maximum continuous engine setting, as a function of altitude can be found in Figure 6-7 through Figure 6-9. Again thrust increases as technology level increases. Only the 86 kW MGT TL 3 produces more thrust than the reciprocating engine. One can also see the change in gradient at the critical altitude of the turbocharged reciprocating engine. The decreasing thrust due to decreasing MGT size is also present during the climb phase. This has a negative effect on the time to reach the desired cruising altitude, see Section 6.5.

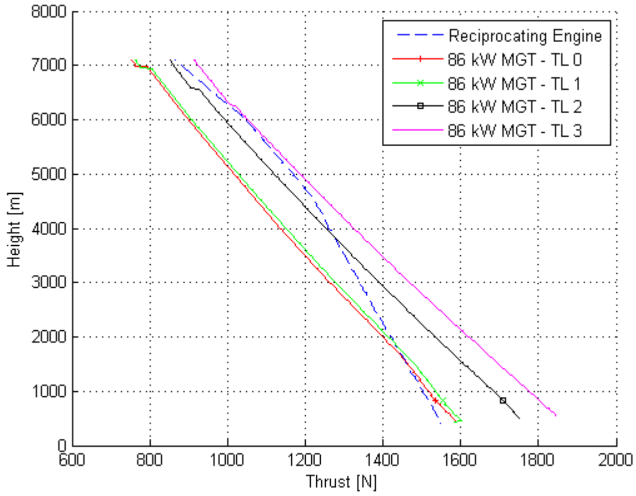

Figure 6-7: Thrust During Climb as a Function of Altitude - 86 kW MGT

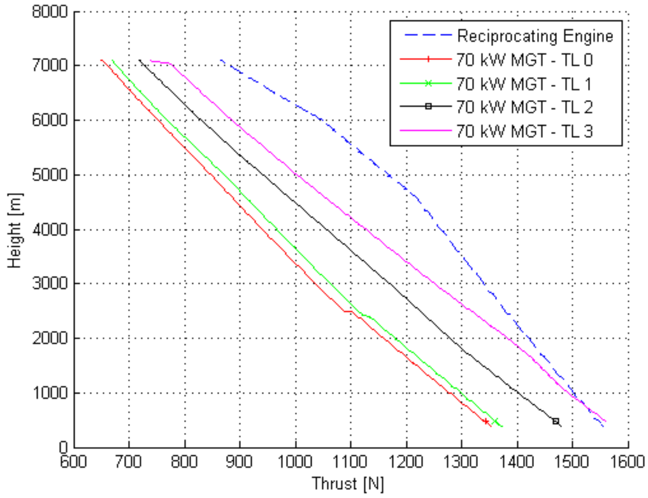

Figure 6-8: Thrust During Climb as a Function of Altitude - 70 kW MGT

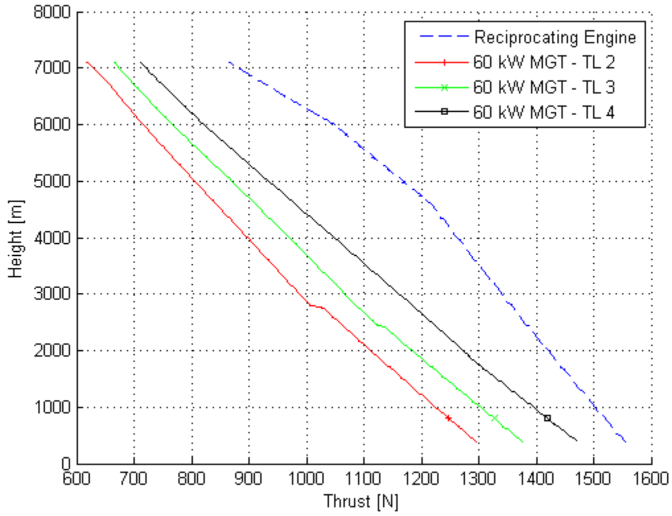

Figure 6-9: Thrust During Climb as a Function of Altitude - 60 kW MGT

Table 6-10 lists the maximum idle thrust during the descent phase. Please note that the idle thrust decreases as altitude increases. None of the MGTs have a matching idle thrust production with the reciprocating engine. The idle thrust of the 86 kW MGT decreases as technology level increases. This trend does however not occur for the 70 and 60 kW MGTs.

Table 6-10: Maximum Thrust [N] During Descent

	Reciprocating engine	86 kW MGT	70 kW MGT	60 kW MGT
TL 0		410	333	/
TL 1		398	308	/
TL 2	360	347	389	343
TL 3		334	339	381
TL 4		/	/	342

Figure 6-10 to Figure 6-12 give the fuel consumption as a function of altitude with the engine setting on maximum continuous. Fuel consumption decreases as altitude increases for all engine types. Decreasing the MGT size results in a decreasing fuel consumption. Only the 60 kW MGT - TL 2 matches the fuel consumption of the reciprocating engine, but only above an altitude of 4500 m; the critical turbo altitude. The highest technology level results in the highest fuel consumption for all MGT sizes. This is in line with the fuel consumption during take-off. Decreasing the technology level to zero does however not necessarily result in the lowest fuel consumption. The fuel consumption at idle engine setting as a function of altitude can be found in Figure 6-13 to Figure 6-15. No MGT matches the fuel consumption of the reciprocating engine at idle engine setting. As altitude decreases fuel consumption increases. Also MGT size reductions results in a decreasing of fuel consumption. The trend in fuel consumption as a result of changing technology levels depends on the engine size. The fuel consumption decreases as the technology level increases for the 86 kW MGT, although the difference is minimal between TL 1, 2 and 3. The fuel consumption decreases from TL 0, 2, 3 and 1 for the 70 kW MGT. The 2% efficiency increase represented by TL 4 of the 60 kW turbine gives the lowest fuel consumption at idle engine setting.

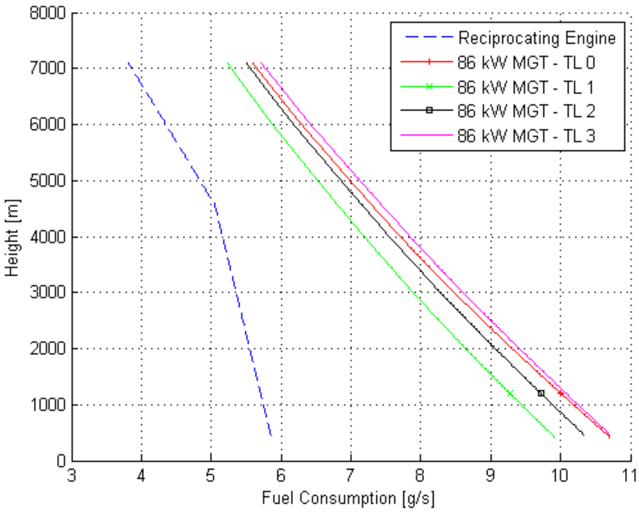

Figure 6-10: Fuel Consumption During Climb as a Function of Altitude - 86 kW MGT

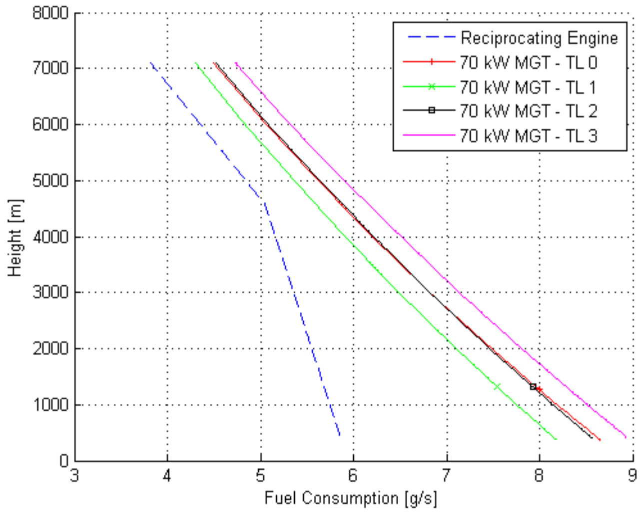

Figure 6-11: Fuel Consumption During Climb as a Function of Altitude - 70 kW MGT

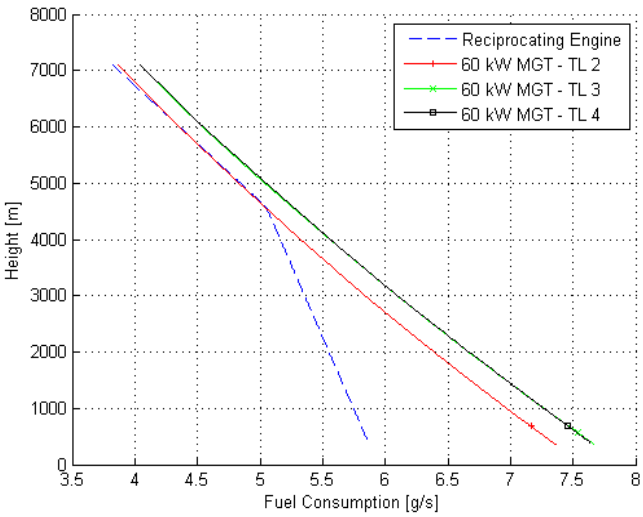

Figure 6-12: Fuel Consumption During Climb as a Function of Altitude - 60 kW MGT

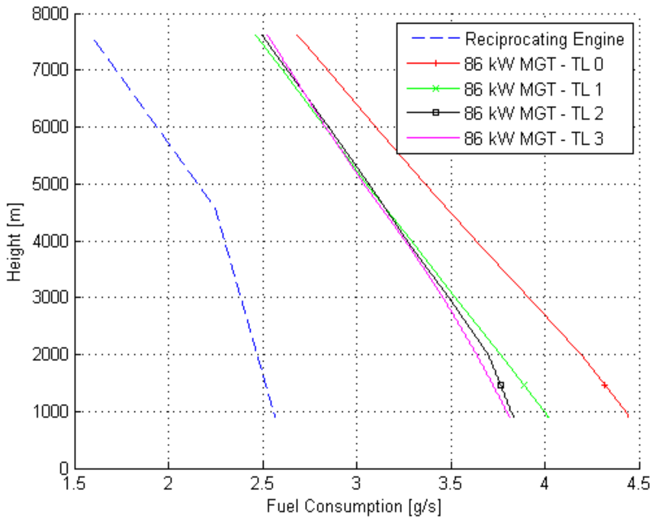

Figure 6-13: Fuel Consumption During Descent as a Function of Altitude - 86 kW MGT

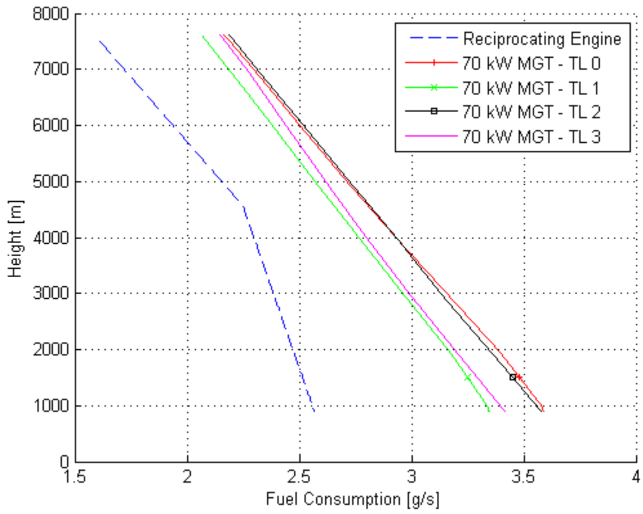

Figure 6-14: Fuel Consumption During Descent as a Function of Altitude - 70 kW Turbine

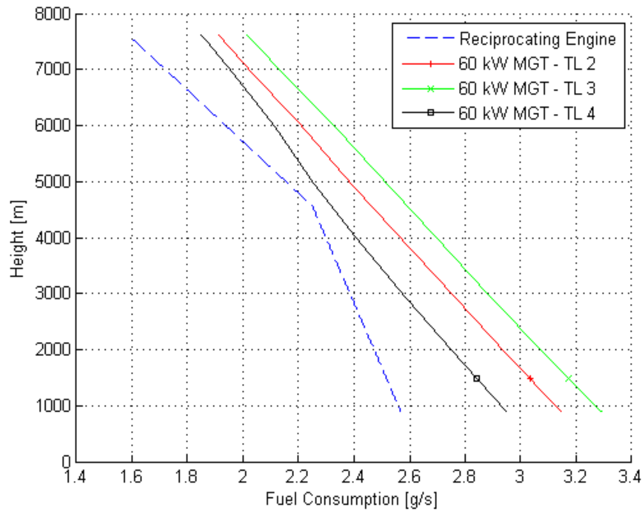

Figure 6-15: Fuel Consumption During Descent as a Function of Altitude - 60 kW Turbine

6.4 Baseline Model Mission Simulation

In this section, the results of the mission simulation are given for the baseline model powered by the reciprocating engine. The comparison in mission performance for the different engine types is outlined in Section 6.5. Figure 6-16 to Figure 6-18 describe the take-off phase. The velocity increases as the aircraft accelerates. θ is increased to the maximum value at the rotation speed, from which the altitude steadily increases. The climb phase is outlined in Figure 6-19 through Figure 6-21. Ideally, an optimum climb is performed at constant calibrated airspeed. However, the power available decreases at lower velocities, see Figure 5-7. Only at higher altitude one can see the trend to climb at constant calibrated airspeed. Rate of climb also decreases as altitude increases. The accelerations of Figure 6-21 are caused by the discretization and have a magnitude of $0.06\ m/s^2$. They can therefore be neglected. Figure 6-22 and Figure 6-23 depict the cruise phase, where lift decreases as weight decreases. The descent phase is represented by Figure 6-24 and Figure 6-25. The descent is performed at constant calibrated airspeed. The descent rate decreases due to the increasing idle thrust by decreasing altitude. Figure 6-26 and Figure 6-27 outlines the approach phase. The velocity first decreases during the descent phase towards the ILS interception altitude, to be kept constant during the level flight and finally increases again during the approach maneuver. The landing phase is described in Figure 6-28 through Figure 6-30, in which the flare and braking maneuvers can be seen.

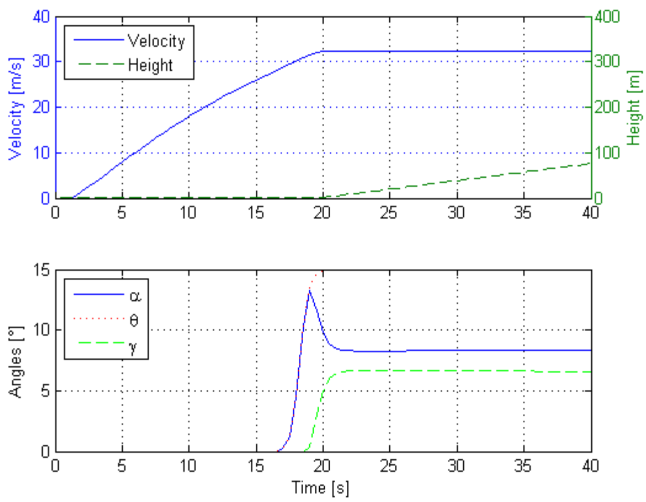

Figure 6-16: Take-Off - Velocity, Height and Angles

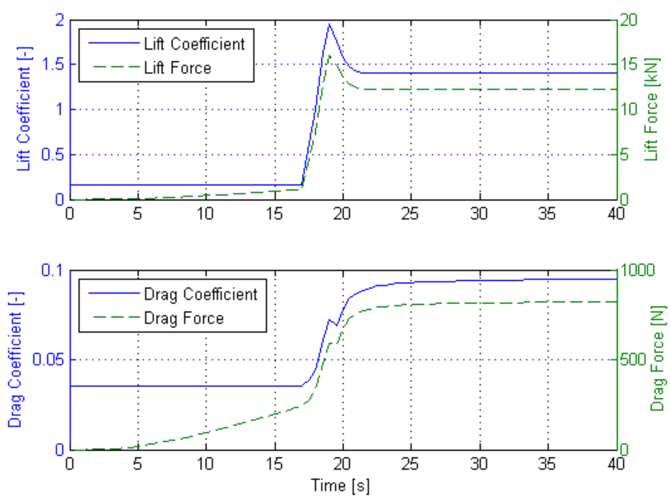

Figure 6-17: Take-off - Lift and Drag Forces and Coefficients

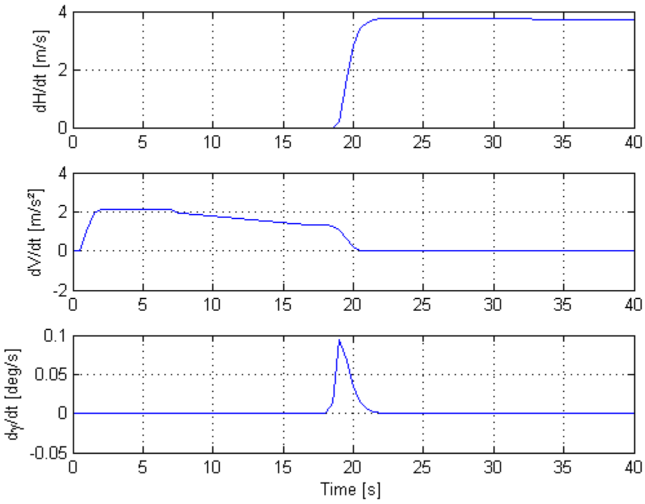

Figure 6-18: Take-off - Height, Velocity and Angle Derivatives

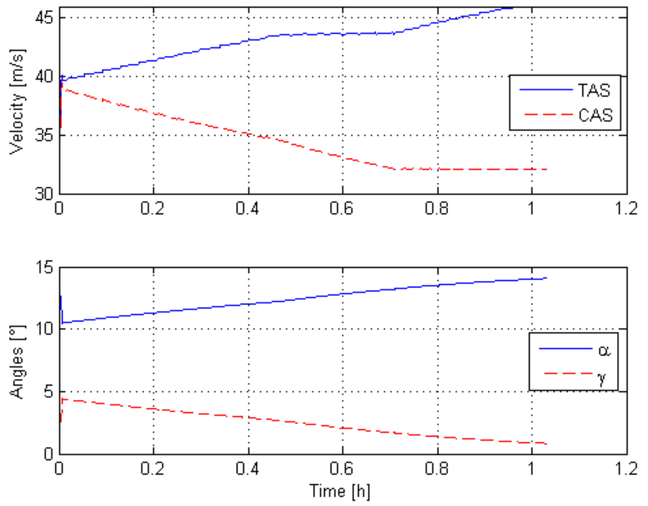

Figure 6-19: Climb - Velocity and Angles

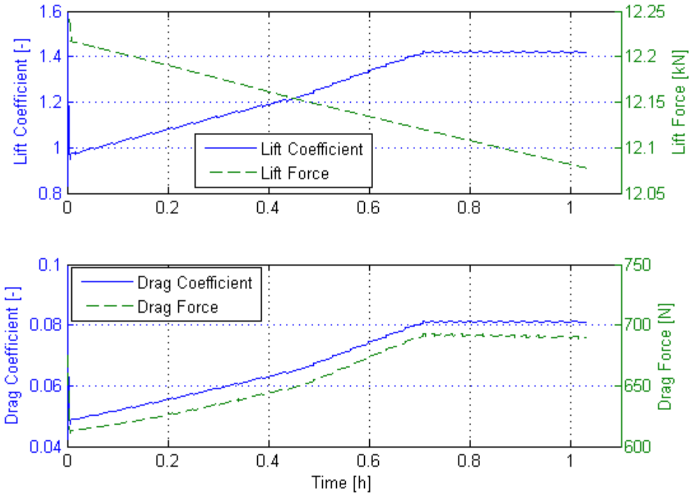

Figure 6-20: Climb - Lift and Drag Forces and Coefficients

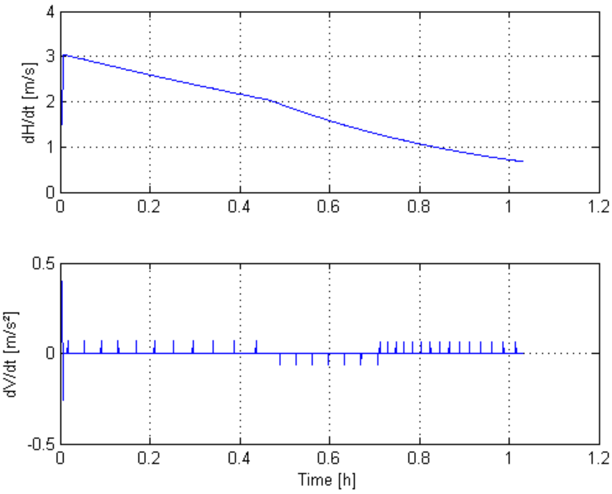

Figure 6-21: Climb - Height and Velocity Derivatives

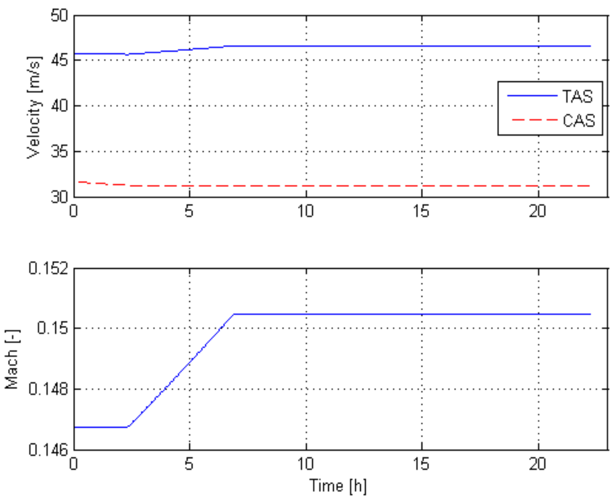

Figure 6-22: Cruise - Velocity Profile and Mach Number

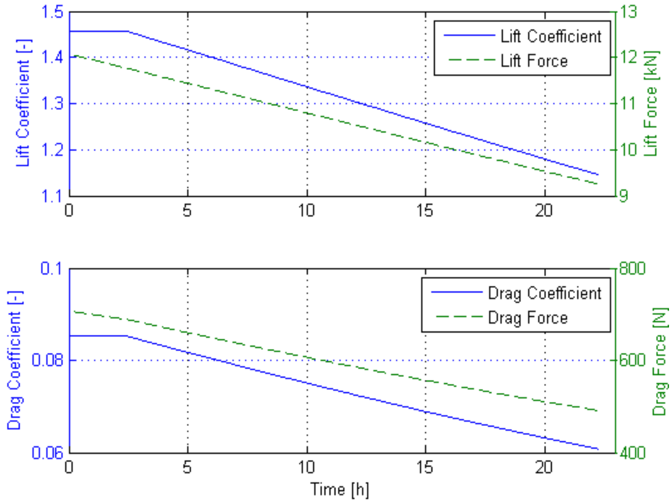

Figure 6-23: Cruise - Lift and Drag Forces and Coefficients

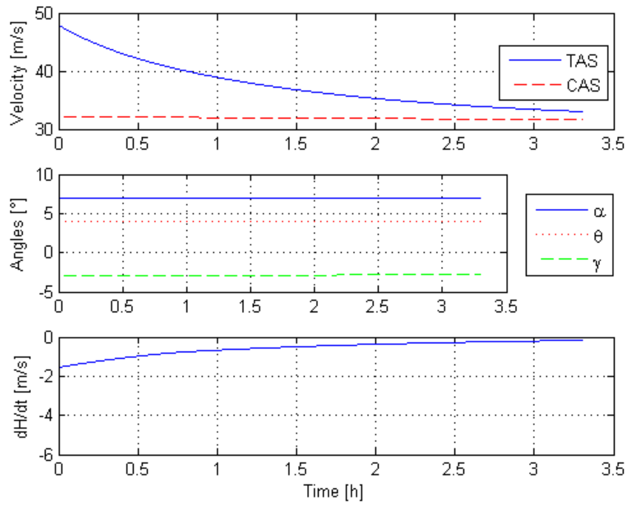

Figure 6-24: Descent - Velocity, Angles and Height Derivatives

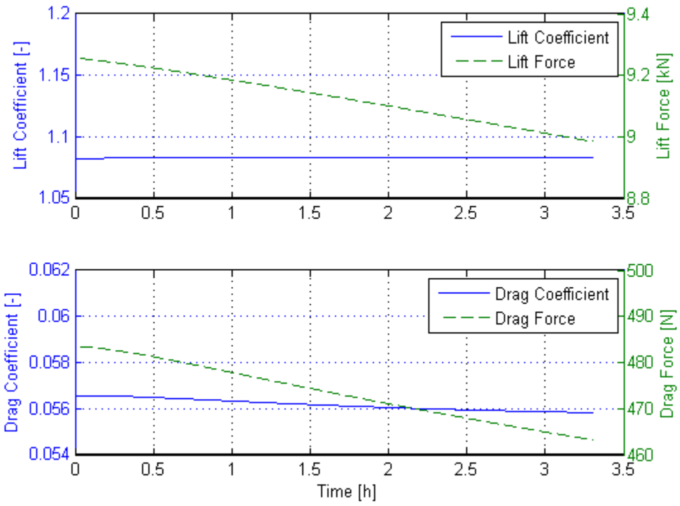

Figure 6-25: Descent - Lift and Drag Forces and Coefficients

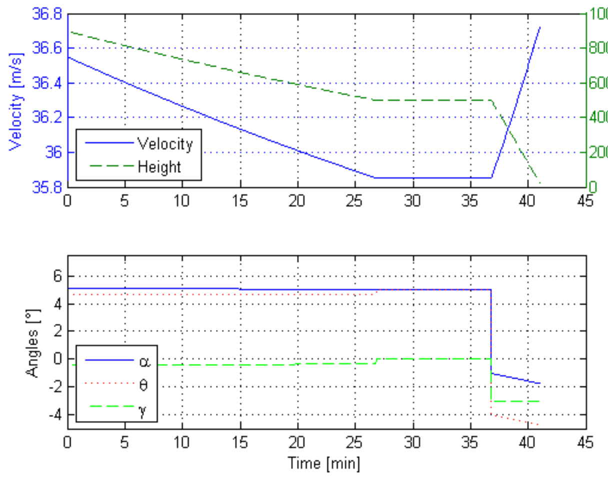

Figure 6-26: Approach - Velocity Profile and Angles

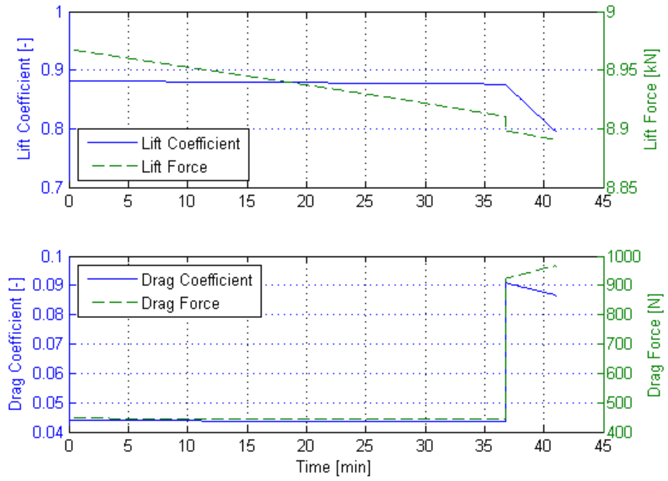

Figure 6-27: Approach - Lift and Drag Forces and Coefficients

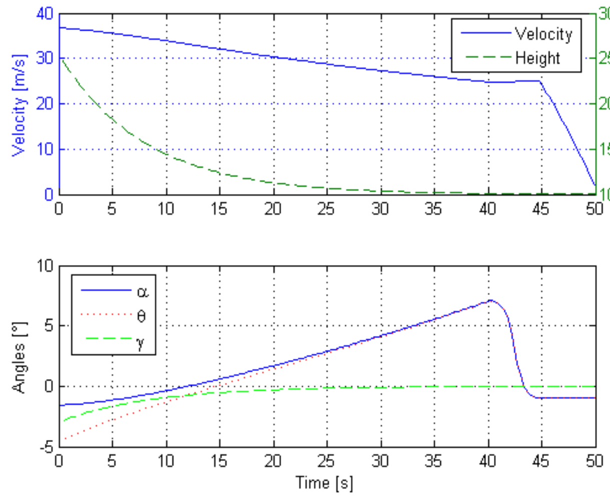

Figure 6-28: Landing - Velocity Profile and Angles

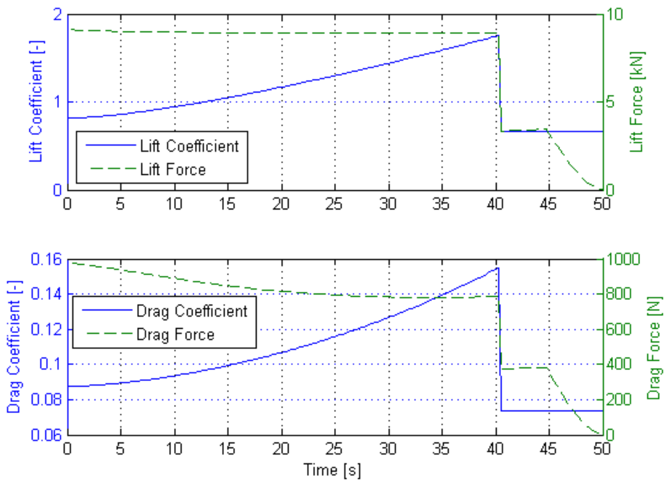

Figure 6-29: Landing - Lift and Drag Forces and Coefficients

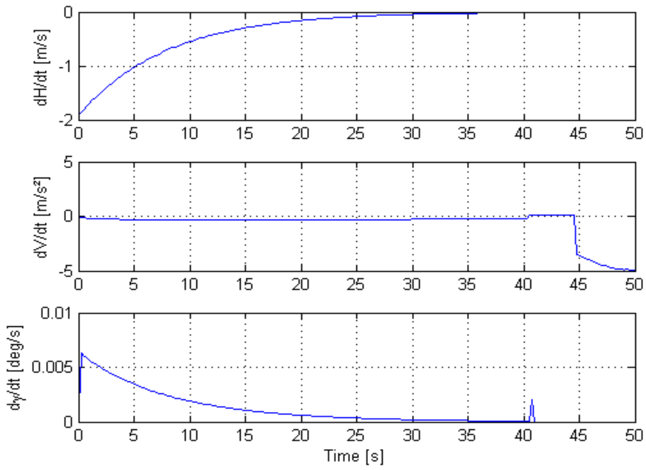

Figure 6-30: Landing - Height, Velocity and Angle Derivatives

6.5 Engine Mission Comparison

The results of the mission performance of each engine type are compared against each other in order to identify any possible performance gains for the MGT. Table 6-11 lists the endurance and range for each engine design. The take-off, loiter, approach and landing endurance are added to represent the remaining endurance. Only the 60 kW MGT - TL 4 is able to cover a larger distance than the reciprocating engine. Range does however increase as engine size is reduced and technology level is increased. Also endurance increases as engine size reduces and technology level increases. However again only the 60 kW MGT - TL 4 can outperform the reciprocating engine. Looking at the climb endurance indicates potential problems if the engine size is reduced even more. Since both the 70 and 60 kW turbines already require 4 and 6 times as long to reach the cruising altitude. Climb endurance improves if the technology level increases. Only the 86 kW MGT - TL 2 and 3 have better climb performance than the reciprocating engine. The cruise endurance increases if engine size is reduced and technology level increased. The descent endurance on the other hand does not indicate a clear dependence on engine size or technology level. The increased descent endurance of the 70 and 60 kW - TL 2 is caused by a higher idle thrust production, compared to the other engine designs with the same power output, see Table 6-10. A higher thrust during the descent phase results in a smaller descent angle, see equation 5-67. This gives a lower rate of descent according to equation 5-59, which results in a longer descent endurance.

Table 6-11: Mission Endurance and Range Comparison

	Climb [h]	Cruise [h]	Descent [h]	Other [h]	Total [h]		Range [km]
Reciprocating	1.1	22.3	3.3	0.9	27.6		4438
86 kW MGT - TL 0	1.3	14.7	4.8	0.7	21.5	-22.1%	3358
86 kW MGT - TL 1	1.2	16.9	4.8	0.8	23.7	-14.0%	3711
86 kW MGT - TL 2	0.9	19.8	3.3	0.6	24.6	-10.7%	3936
86 kW MGT - TL 3	0.7	20.8	2.9	0.6	25.0	-9.1%	4026
70 kW MGT - TL 0	4.4	15.3	2.8	0.7	23.2	-15.9%	3663
70 kW MGT - TL 1	3.1	18.6	2.6	0.7	25.0	-9.4%	3968
70 kW MGT - TL 2	1.8	18.4	4.4	0.8	25.4	-2.9%	4193
70 kW MGT - TL 3	1.3	21.0	3.2	0.6	26.2	-5.0%	4168
60 kW MGT - TL 2	6.8	15.8	3.1	0.7	26.4	-4.0%	4136
60 kW MGT - TL 3	3.3	18.5	4.1	0.9	26.8	-2.9%	4193
60 kW MGT - TL 4	1.9	23.0	3.1	0.7	28.7	4.2%	4567

Figure 6-31 depicts the percentage of fuel use for each mission stage with respect to the total mission. Again take-off, loiter approach and landing are added together because of their limited duration compared to the total mission. The cruise phase obviously consumes the most amount of fuel, approximately 70% to 80% depending on the engine. All MGTs use a higher percentage of fuel during climb and descent compared to the reciprocating engine, while they use a lower percentage during cruise. These results however need to be analyzed in combination with the phase endurance, since only the 60 kW MGT - TL 4 has a longer cruise endurance than the reciprocating engine due to a better cruise fuel consumption.

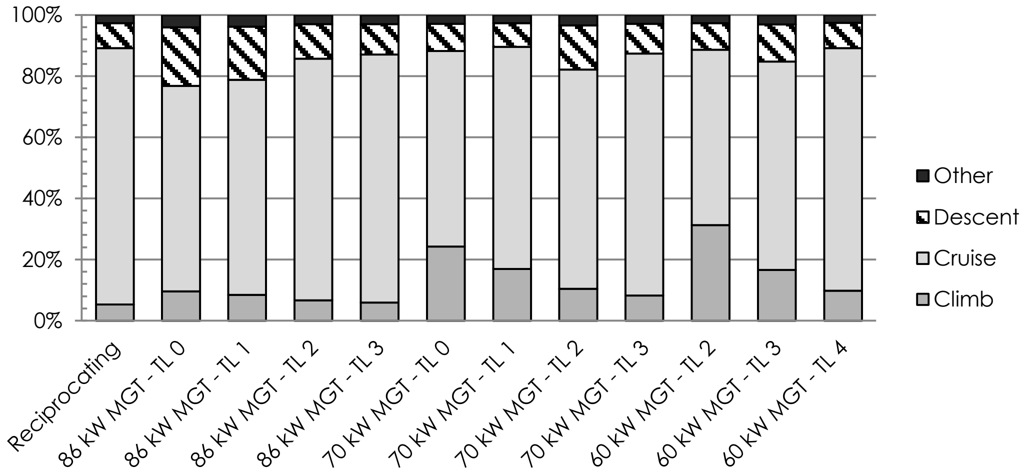

Figure 6-31: Mission Fuel Consumption Comparison

The mission height profiles of the different MGT sizes and technology levels with respect to the reciprocating engine can be found in Figure 6-32 to Figure 6-34. The endurance increases as engine size decreases and technology level increases, confirming the endurance results of Table 6-11. The increasing time to reach the desired cruising altitude due to the decreasing engine size is cause by the climb from 6000 m to 7000 m.

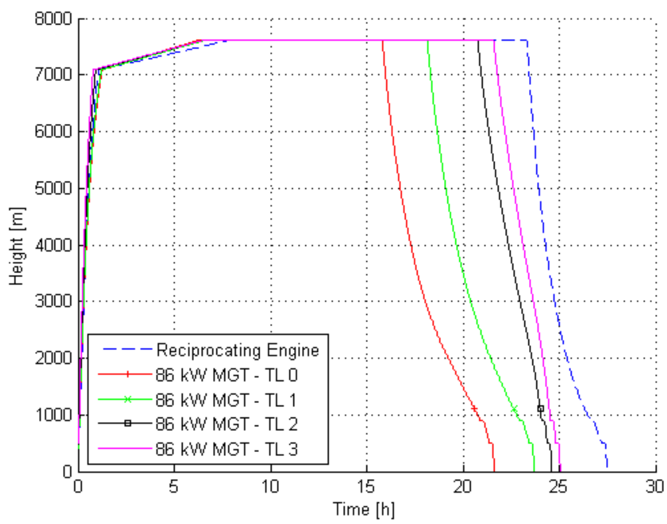

Figure 6-32: Mission Height - 86 kW MGT

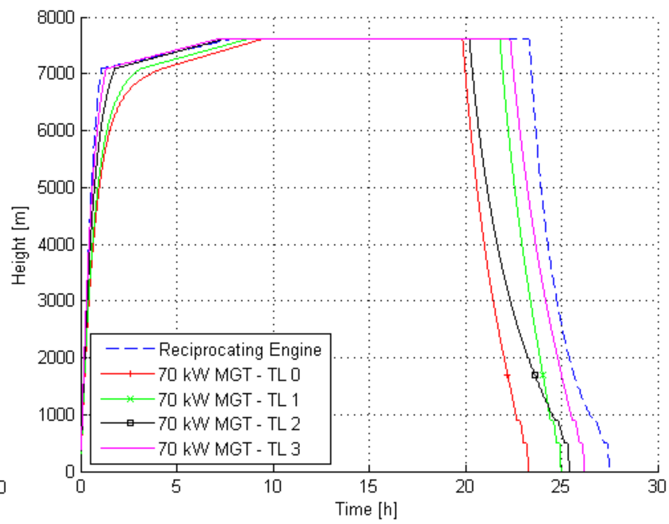

Figure 6-33: Mission Height - 70 kW MGT

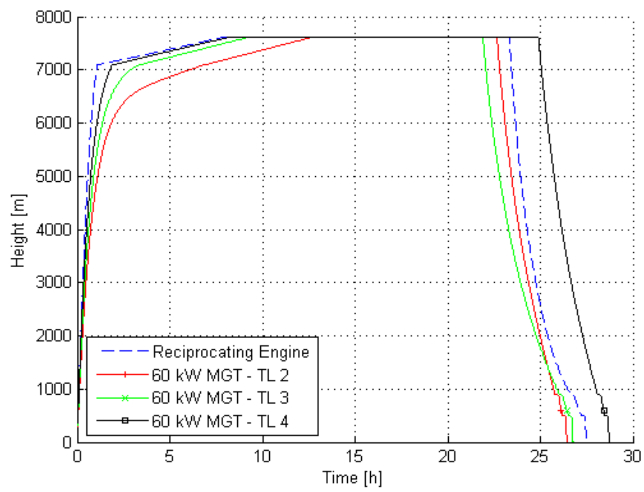

Figure 6-34: Mission Height - 60 kW MGT

6.6 Verification of the Model

A proper verification of the model is required to ensure the simulation yields in accurate results. The weight breakdown analysis is verified by adding the different component weights together and compare them with the MTOW of the baseline UAV. The results of this comparison can be found in Table 6-12. The weight breakdown analysis of the baseline UAV with the reciprocating engine underestimates the MTOW by 2.5%. The error margin however increases to 4.2% as the MTOW decreases due to engine weight reductions. These error margins are however small and still acceptable taking the limited datasets into account. It is therefore concluded that the weight breakdown analysis is verified to work correctly.

Table 6-12: Verification of the Weight Breakdown Analysis

	Reciprocating Engine	86 kW MGT	70 kW MGT	60 kW MGT
Actual MTOW [kg]	1250	1209.3	1204.3	1200.3
WER Average MTOW [kg]	1219.7	1164.6	1157.9	1152.4
Difference [kg]	30.3	44.7	46.4	47.9
Error Margin	2.5%	3.8%	4%	4.2%

The aerodynamic analysis provides important input for the flight performance simulation making proper verification a necessity. The number of panels and their distribution are verified using the rectangular wing analogy. An unswept wing with a chord length of 1 m and wingspan of 6 m is modeled in Tornado with different panel density and distribution. Please note that the number of panels is defined per half span length. The influence of changing the number of panels increases as the angle of attack is increased, see Figure 6-35. Especially at very high angles of attack (AoA) ($\alpha > 15°$). These AoAs are outside the operation range of the UAV and are unrealistic due viscous effects which cause separation. Variations in the number of chordwise panels have a negligible effect on C_L. Spanwise variations have a more significant effect on C_L. The C_L values increase as the number of panels decreases. The results start to deviate drastically if the number of spanwise panels is smaller than 4. The effect of increasing the number of spanwise panels from 8 to 20 is a reduction of $\Delta C_L = -0.03$ at $\alpha = 14°$. From this it is decided to use 5 panels per meter in chordwise direction, since a higher chordwise panel density does not increase the accuracy. It does however increases the computation time. A panel density of 2 panels per meter is used in spanwise direction which should give acceptable results with a limited computation time.

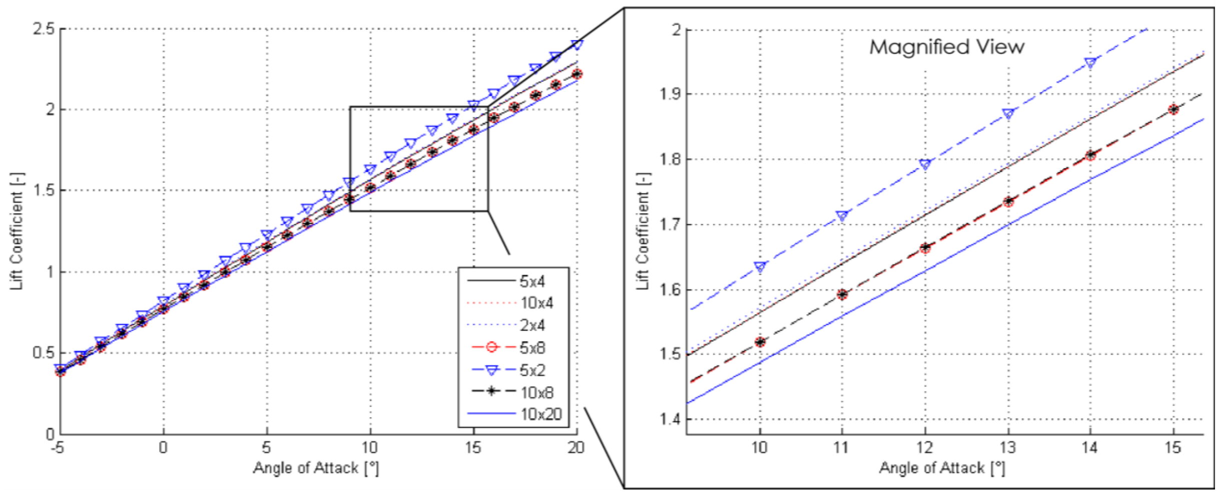

Figure 6-35: Verification of Number of Panels (Chordwise x Spanwise)

Five different panel distributions are available: linear, spanwise half cosine, spanwise cosine, chordwise cosine/spanwise half cosine and chord cosine. The variation due to the different distributions remains constant as a function of the AoA (Figure 6-36). A variation in spanwise distribution only shows a marginal effect and can therefore be considered negligible. C_L decreases by 0.1 if a chordwise cosine panel distribution is used instead of a linear distribution. A linear distribution is however not preferred since one would like to have a higher panel density near the leading edge and wing tips. It is therefore decided to use a chordwise cosine/spanwise half cosine distribution. The conclusions of the panel verification are in line with findings in literature. The findings discussed in literature are **[29]**:

- There is a perceivable increase in C_L variation as a function of α if the panel density is increased/decreased.
- No direct correlation between greater panel density and higher result accuracy is identified.
- Non-linear panel distribution in chordwise direction has a more significant effect compared to spanwise direction.
- A linear panel distribution in chordwise direction results in an overpredication of the lift coefficient.

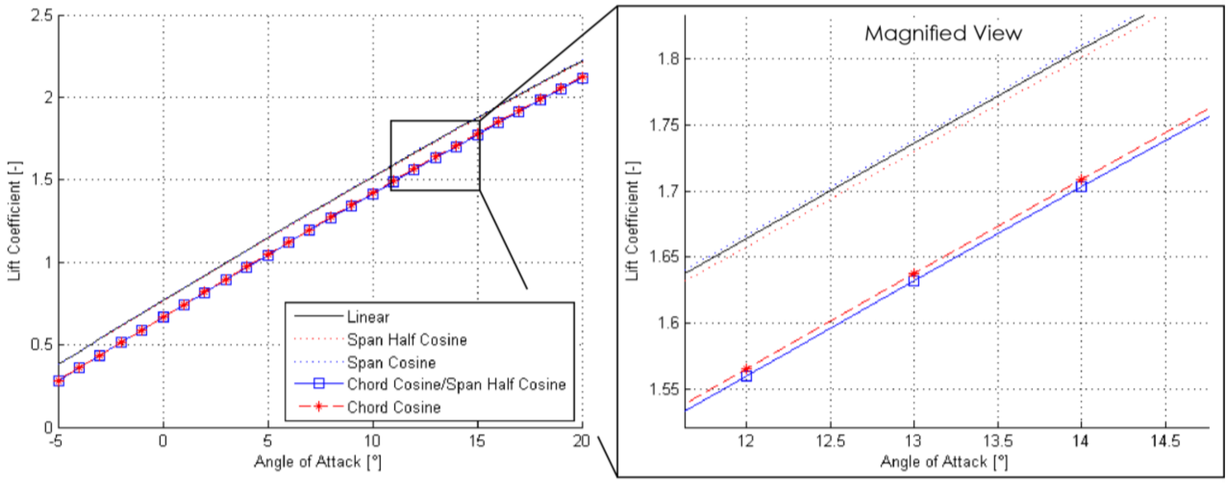

Figure 6-36: Verification of Panel Distribution

No exact analytical solution exists for the determination of the turbulent skin friction coefficient used to determine the zero-lift coefficient of the UAV. The selected method used during this Master thesis is therefore verified by comparing it with three other methods, see Figure 5-2 and Anderson **[46]**. The first method uses a different equation to determine $C_{f_{turb}}$, see equation 6-1. The second method does not subdivides the calculation of C_f into a laminar and turbulent part. Instead it uses equation 6-2 to determine C_f. The third method also uses one equation to determine C_f, see equation 6-3.

$$C_{f_{turb}} \approx \frac{0.455}{(\log_{10} Re_{comp})^{2.58}} \qquad \textbf{6-1}$$

$$C_f = \frac{0.455}{(\log_{10} Re_{comp})^{2.58}} - \frac{1700}{Re_{comp}} \qquad \textbf{6-2}$$

$$C_f = \frac{0.074}{{Re_{comp}}^{0.2}} - \frac{1742}{Re_{comp}} \qquad \textbf{6-3}$$

Table 6-13 gives an overview of the different methods and the original method in order to verify the calculation of the skin friction coefficient. All methods resemble the results obtained using the original method. The deviation is smaller than 0.002 or 6%. From this it is decided that the method used to determine the skin friction coefficient is valid.

Table 6-13: Verification of the Skin Friction Coefficient

	Original	Method 1	Method 2	Method 3
Wing	0.0032	0.0032	0.0031	0.0031
Horizontal Tail	0.0033	0.0032	0.0031	0.0032
Vertical Tail	0.0032	0.0032	0.0031	0.0032
Fuselage	0.0025	0.0026	0.0026	0.0024
Booms	0.0026	0.0027	0.0027	0.0025

The conditions of the maximum airspeed as defined by the manufacturer are unclear. No information is given regarding the weight and altitude related to the maximum airspeed. Both parameters can however influence the maximum airspeed. Figure 6-37 depicts the maximum airspeed as a function of altitude for different rates of climb with variations to the MTOW. An MTOW of 1250 kg results in a maximum velocity of

60.7 m/s at a cruising altitude of 7600m. The maximum velocity increases/decreases to 63.3 m/s and 56.9m/s if the MTOW is increased/decreased with 50 kg, respectively. From this it is concluded that the maximum velocity defined by the manufacturer is the maximum airspeed at a cruising altitude of 7600 m. A closer maximum velocity match is possible if the correction factor, K_C, for the miscellaneous drag components of equation 5-47 is increased from 1.2 to 1.3, see Figure 6-38. The maximum velocity at 7600 m for an MTOW of 1250 kg with K_C = 1.3 is equal to 58.0 m/s.

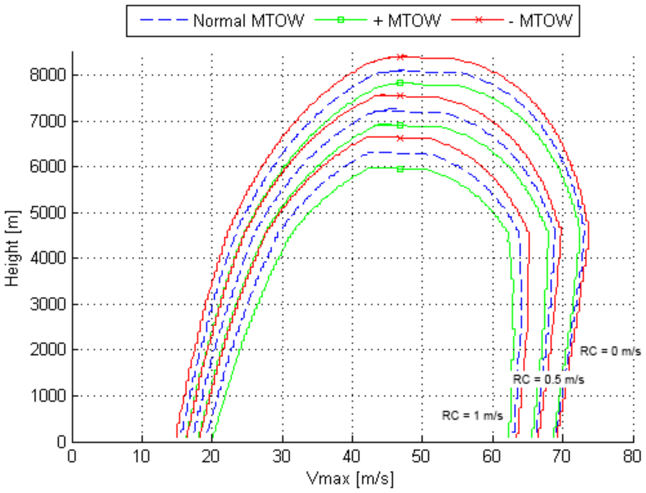

Figure 6-37: Verification of the Maximum Velocity (K_c = 1.2)

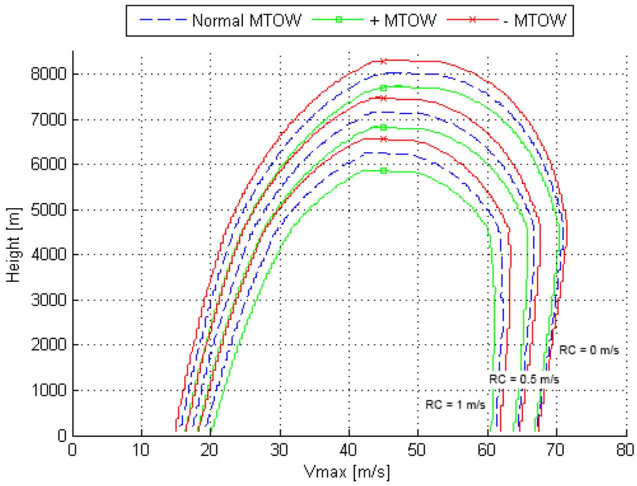

Figure 6-38: Verification of the Maximum Velocity (K_c = 1.3)

The criteria to obtain maximum endurance are derived assuming constant power available **[39]**. This is however an analytical approximation and deviates from the actual power available curves. The fuel flow as a function of airspeed at cruising altitude for the different engine types is therefore depicted in Figure 6-39. From this figure one has to concluded that the fuel flow of the reciprocating engine remains constant as a function of airspeed. The fuel flow of the different MGT designs show a marginal decrease if the airspeed is decreased. The trend in fuel flow does not change if the technology level is increased, only the absolute values change. The different technology levels are therefore not included in this figure. The marginal decrease in fuel consumption implies that the criteria to obtain maximum endurance defined in Section 5.4.3 and 5.4.4 are applicable to this case study. These criteria are however identified as a point for future research, see Chapter 10.

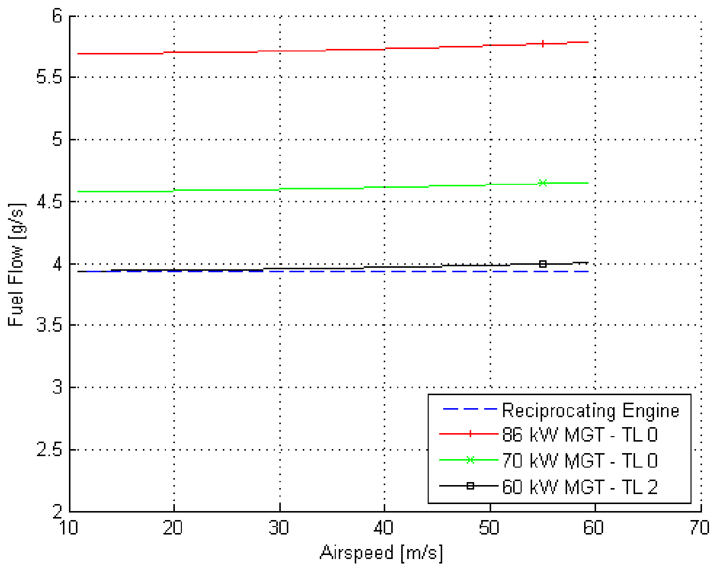

Figure 6-39: Fuel Flow as a Function of Airspeed (H = 7000 m)

A validation of the model is obtained by comparing the mission results with the performance data of the baseline UAV provided by the manufacturer. Unfortunately, only limited flight performance data is available. The endurance of the baseline UAV is 24 hrs. The endurance of the model is estimated to be 26.7 hrs which is an overestimation of 2.7 hrs or 11%. This overestimation is partially the result of inaccuracies in the model, but also due to uncertainties about the performance data of the manufacturer. The manufacturer for example does not specify under which conditions this endurance can be achieved. The cruise altitude, gross weight and mission profile influence the endurance significantly. The specifications simply define the endurances as 'more than 24 hrs'. Nevertheless, inaccuracies in the model still need to be identified and clarified. The aerodynamic model can have a large influence on the overall endurance. A more accurate model logically results in a better performance match with the baseline UAV. However both engine types use the same model. Inaccuracies therefore influence the results of both engine types by an equal extend. The fuel consumption of the reciprocating engine has a more significant effect. Unfortunately, the limited data problem could not be resolved. A more accurate fuel consumption model is therefore highlighted as a point for future research. The reader is referred to **[5]** for a verification of the turbine models.

7
Sensitivity Analysis

Some parameters need to be assumed to model the baseline UAV due to a lack of data available into open literature. One would like to know the influence of these parameters on the mission simulation. A sensitivity analysis is therefore performed to examine the influence of modifications to the assumed values. The model with the reciprocating engine is used during this analysis.

7.1 UAV Dimensions

The dimensions of the UAV are acquired using a three-view scaled drawing of the manufacturer and influence the aerodynamic analysis and flight performance analysis. This method is however susceptible to inaccuracies. The sensitivity of these inaccuracies is investigated by increasing and decreasing all dimensions by 2.5%, wetted areas are increased/decreased by 5% (see Figure 7-1). The wing span and fuselage length remain unaltered, since they are warranted by the manufacturer; as are the sweep angles of the main wing and vertical tails.

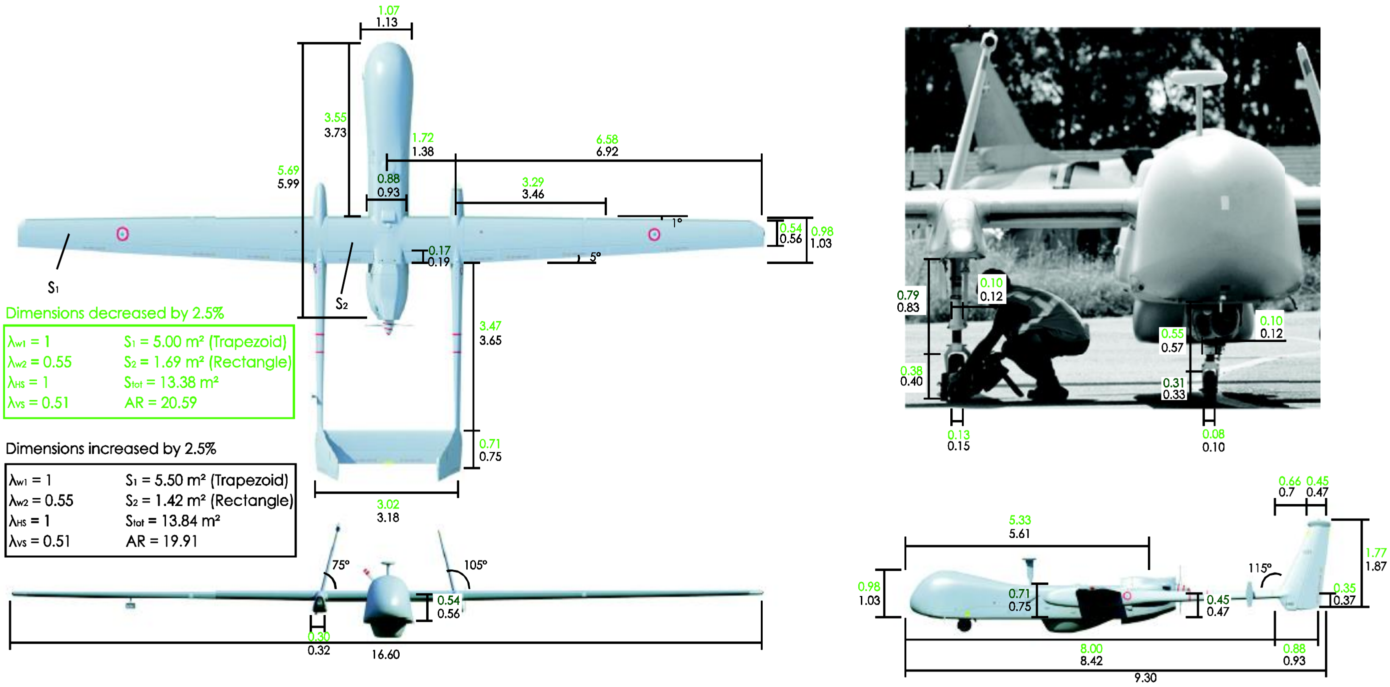

Figure 7-1: New Dimensions of Harfang UAV (Green: - 2.5%, Black: +2.5%)

Zero-Lift Coefficient

Table 7-1 lists the impact of increasing/decreasing the dimensions on the drag coefficient. The zero-lift drag coefficient of most components is relatively insensitive, with the exception of the landing gear and flap deflections. It is therefore decided to forward this error margin into the mission results in order to see the overall effect of increasing/decreasing the dimensions in the worst case scenario.

Table 7-1: Sensitivity Analysis on Drag Coefficient

Component	Zero-lift coefficient	Increased Dimension		Decreased Dimensions	
Wing	0.0082	0.0082	0%	0.0082	0%
Horizontal Tail	0.0015	0.0015	0%	0.0014	6.7%
Vertical Tail	0.00081	0.00083	2.5%	0.00076	6.2%
Fuselage	0.0039	0.0040	2.6%	0.0038	2.6%
Booms	0.00083	0.00085	2.4%	0.0008	3.6%
Landing Gear	0.0084	0.0092	9.5%	0.0075	10.7%
Flaps 5°	0.0039	0.0042	7.7%	0.0035	10.3%
Flaps 20°	0.0312	0.0338	8.3%	0.0284	9%
Oswald factor	0.5191	0.5276	1.6%	0.5135	1.2%
C_{D_0} Cruise	0.0203	0.0205	1%	0.0200	1.5%
C_{D_0} Take-Off	0.0350	0.0366	4.6%	0.0332	5.1%
C_{D_0} Landing	0.0677	0.0742	9.6%	0.0630	6.9%

Mission Results

The effect of increasing/decreasing the dimensions on the mission results is given in Table 7-2. Only the relevant mission phases are included, since take-off, loiter, approach and landing are of limited duration. The effect is of minor influence towards the mission results. Moreover, if the reserve fuel of each mission simulation is taken into account the differences become of such insignificance that increasing/decreasing the dimensions by 2.5% has a negligible effect on the mission results. It is therefore concluded that the dimension uncertainties of the model can be neglected.

Table 7-2: Sensitivity Analysis of the Dimensions on the Mission Results

	Original Dimensions	Increased Dimensions		Decreased Dimensions	
Climb Time [h]	1.1	1.1	0%	1.1	0%
Cruise Time [h]	22.3	22.3	0%	22.9	2.6%
Descent Time [h]	3.3	3.3	0%	3.3	0%
Total Endurance [h]	27.6	27.5	-0.4%	27.6	0%
Climb Distance [km]	153	152	-0.7%	154	0.7%
Cruise Distance [km]	3724	3679	-1.2%	3752	0.8%
Descent Distance [km]	446	446	0%	450	0.9%
Total Distance [km]	4438	4388	-1.1%	4474	0.8%
Reserve Fuel [kg]	-0.40	-0.04		-0.53	

7.2 Critical Reynolds Number

The critical Reynolds number determines the transition point, from laminar to turbulent flow, along the component. Predicting the value of Re_{cr} is difficult under specific conditions. The analysis of the transition point is therefore still an active research area in modern aerodynamics **[46]**. A value of 500,000 is commonly suggested. An examination of the sensitivity gives an indication of the impact this assumption has. The results are listed in Table 7-3. From this it becomes clear that an increase/decrease of $1 \cdot 10^5$ only has a minor effect on the results. A larger effect is present when the value is decrease towards $5 \cdot 10^4$. This shifts the transition point upstream, extending the turbulent flow part which increases the drag coefficient. An even more significant result is produced when Re_{cr} is increased towards $5 \cdot 10^6$, since the component experiences a longer laminar flow part, hence reducing the drag coefficient extensively. The critical Reynolds number is therefore identified as a recommendation for future research.

Table 7-3: Sensitivity of the Critical Reynolds Number

		Increased $Re = +1 \cdot 10^5$	Decreased $Re = -1 \cdot 10^5$	Increased $Re = +1 \cdot 10^6$	Increased $Re = +2 \cdot 10^6$	Increased $Re = +5 \cdot 10^6$	Decreased $Re = -5 \cdot 10^4$
C_{D_0}Cruise	0.0203	0.0199	0.0207	0.0182	0.0141	0.0018	0.0221
C_{D_0} Take-Off	0.0350	0.0346	0.0354	0.0329	0.0288	0.0166	0.0368
C_{D_0} Landing	0.0677	0.0673	0.0681	0.0656	0.0615	0.0493	0.0695

7.3 Drag Coefficient

Increasing or decreasing the dimensions by 2.5% influences the zero-lift drag coefficient by a maximum of approximately 10%. The sensitivity analysis is extended to the total drag coefficient by investigating the consequences of increasing/decreasing C_{D_0} by 10%. The results are listed in Figure 7-2 and show a constant offset of 0.002 for cruise configuration which increases to 0.007 for landing configuration. The Oswald factor is estimated using an empirical formula and it is therefore interesting to examine the sensitivity of this factor by increasing/decreasing it with 10%, see Figure 7-3. The effect increases as the α is increased, due to the increasing ${C_L}^2$ in the drag polar equation. The offset at $\alpha = 15°$ is already 0.01 for cruise configuration and doubles for the landing configuration. How the increase/decrease of total drag coefficient translates to the mission performance is examined in Section 7.4. Nevertheless, the determination of the Oswald factor is already highlighted as a recommendation for future research, see Chapter 10.

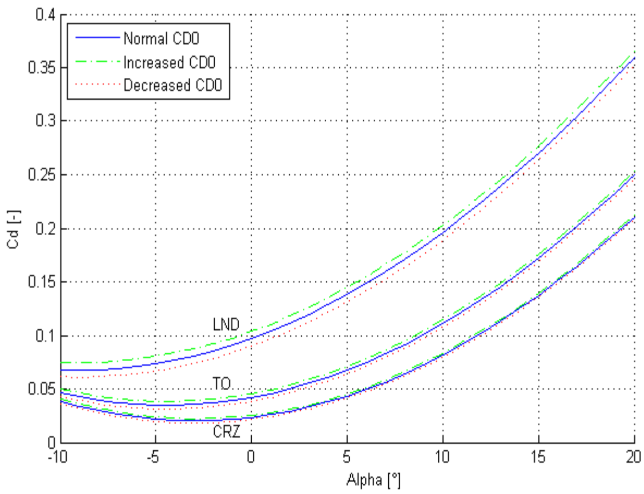

Figure 7-2: Sensitivity of C_{D_0} on $C_{D,Tot}$

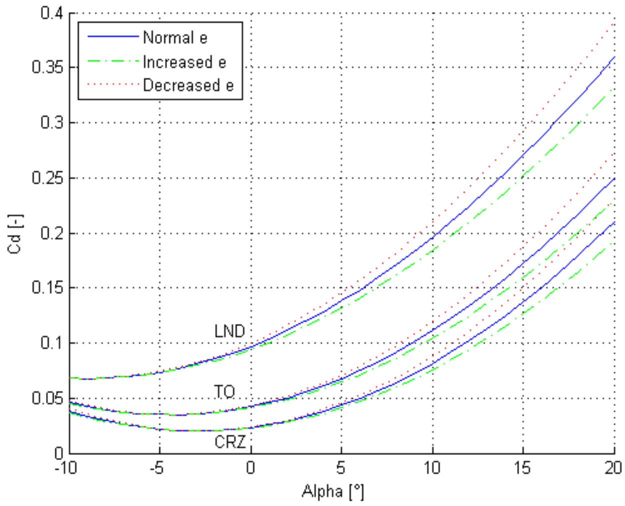

Figure 7-3: Sensitivity of e on $C_{D,Tot}$

7.4 Mission Results

Table 7-4 lists the sensitivity of various parameters on the mission performance of the reciprocating engine. Three different parameters are examined, including: the total drag coefficient (±10%), specific fuel consumption (±5%) and user-specified propeller efficiency (±0.05). Section 7.1 already concluded that minor modifications dimensions had no notable effect on the mission performance, see Table 7-2. The drag coefficient on the other hand has a more significant effect. The total endurance increases/decreases with approximately 1.1% to 1.4% if C_D decreases/increases, influencing all mission phases. The SFC has the largest influence, up to ±5%. It should however be noted that only the cruise phase is affected by modifications to the specific fuel consumption. The user-specified efficiency influences mainly the cruise and descent phase. An increase/decrease of 0.3% to 1.1% on total endurance is examined. The range characterizes only a minor sensitivity, except for the specific fuel consumption. It can therefore be concluded that the mission results only have a limited sensitivity to minor modifications to the drag coefficient and user-specified propeller efficiency. The specific fuel consumption however has a more pronounced sensitivity. Future research is therefore required to confirm the fuel flow data of the reciprocating engine.

Table 7-4: Sensitivity Analysis on the Mission Performance

	Climb [h]	Cruise [h]	Descent [h]	Other [h]	Endurance Total [h]		Range [km]	
Baseline model	1.1	22.3	3.3	0.9	27.6		4438	
$+10\%\ C_D$	1.3	22.8	2.4	0.7	27.2	-1.4%	4400	-0.9%
$-10\%\ C_D$	1.0	21.7	4.1	1.1	27.9	1.1%	4464	0.6%
$+5\%$ SFC	1.1	21.0	3.3	0.9	26.3	-4.7%	4227	-4.8%
-5% SFC	1.1	23.7	3.3	0.9	29.0	5.1%	4670	5.2%
$+0.05\ \eta$	1.0	22.0	3.7	1.0	27.7	0.3%	4448	0.2%
$-0.05\ \eta$	1.2	22.5	2.8	0.8	27.3	-1.1%	4409	0.7%

Part III - Redesign Phase

8
UAV Redesign

The results of Section 6.5 indicate a performance gain for the 60 kW - TL 4 (TIT = 1250 K, Pr = 8 and η = +2%) MGT. This performance gain can be extended if the airframe is optimized for the MGT. The lower engine weight and fuel weight (to perform the same mission as the reciprocating engine) result in a lower MTOW. The payload remains unaltered. The reduction in MTOW lowers the component weight and required fuel weight which in turn reduces the MTOW again. This process is iterated until the weight reduction convergences and the increase in performance gain is no longer significant. Section 8.1 outlines the redesign phase of the UAV platform. The results of each design iteration are given in Section 8.2. An overview of the new mission performance can be found in 0.

8.1 Platform Modifications

The first step of the redesign phase is to simulate the mission with a lower MTOW as a result of the engine weight reduction. The required endurance is set equal to the endurance of the baseline UAV with the reciprocating engine (27.6 hrs) to match mission requirements. The remaining fuel after the mission is removed, resulting in fuel weight reduction. The new MTOW is calculated using the reduced fuel, OEW and the payload weight. A weight breakdown analysis is carried out to optimize the airframe for the weight reduction by modifying the wing, fuselage and empennage design (see Section 8.1.1 to 8.1.3). This process is iterated and results in a scaled-down airframe with a lower MTOW. The resulting MTOW is corrected by the error margin of the weight breakdown analysis. Next, the dimensions of the modified airframe are implemented in Tornado and the flight performance program. The lower MTOW and scaled-down airframe result in a reduction of fuel consumption. The remaining fuel after the mission can again be removed and the entire process can be repeated. An overview of the redesign process is depicted in Figure 8-1. A number of redesign loops is performed until the fuel weight reduction is no longer significant.

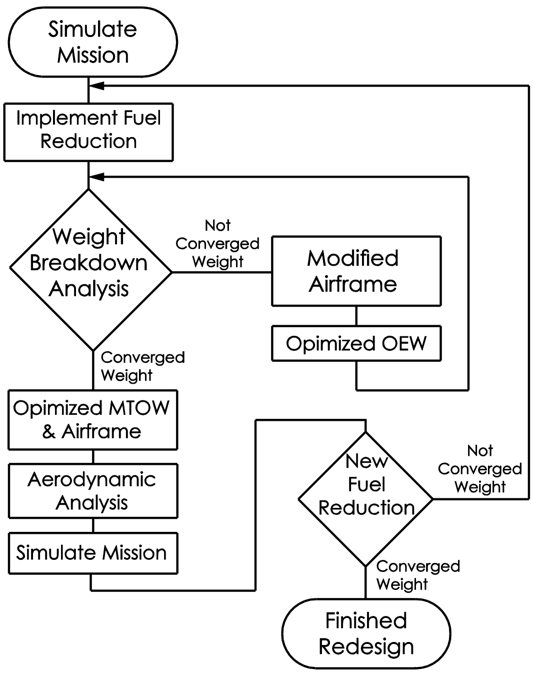

Figure 8-1: Redesign Process

8.1.1 Wing Design

Only the size of the wing is reduced; the wing architecture remains unaltered during the redesign. The wing loading of the original UAV serves as a starting point for the redesign of the wing planform. The same wing loading is used for the redesign and in combination with a lower MTOW results in a smaller wing area. The wing span is obtained from the aspect ratio which is kept constant during the redesign procedure. The distribution between the unswept and swept wing section is also kept constant.

8.1.2 Fuselage Design

Raymer **[23]** relates the airframe length to the MTOW, see equation 8-1. The constants a and c depend on the aircraft configuration and are therefore revised to be applicable for MALE and HALE UAVs ($a = 0.656$ and $c = 0.466$) **[29]**. The revised equation has an error margin of 7% for various existing UAVs **[29].** The error margin of the baseline UAV is below 3% and is therefore neglected. The fuselage and boom length is calculated by multiplying l_{AF} with a fraction based on the baseline UAV, see equation 8-2. The change in fuselage length is applied to the straight fuselage section, see Figure 5-3.

$$l_{AF} = a(W_{TO})^c \quad \textbf{8-1}$$
$$l_{Fus} = 0.7 \cdot l_{AF} \; and \; l_{Booms} = 0.55 \cdot l_{AF} \quad \textbf{8-2}$$

The width and height of the fuselage remain constant during the redesign in order to house the gimbaled antenna and payload. Both engine types require a gearbox, canceling out the possible drag reduction caused by a reduced frontal area of the MGT compared to the reciprocating engine.

8.1.3 Empennage Design

The empennage design consists out of the horizontal and vertical tail design. Their primary function is to provide stability and controllability in longitudinal and directional direction. The horizontal and vertical tail volume coefficients are used for the conceptual redesign, see equation 8-3 and 8-4. References use values of 0.75 and 0.06, respectively **[28]**. This is in line with the tail volume coefficient of the Harfang EADS ($c_{HT} = 0.84$ and $c_{VT} = 0.05$). The coefficients are used to calculate the tail surface areas. New span, root and tip chords are calculated using the aspect ratio of the baseline UAV. Please note that the surface area of the vertical tail needs to be divided by a factor of two due to the twin tail configuration.

$$c_{HT} = \frac{l_t}{c_{mean}} \frac{S_{HT}}{S_W} \quad \textbf{8-3}$$
$$c_{VT} = \frac{l_v}{b} \frac{S_{VT}}{S_W} \quad \textbf{8-4}$$

The moment tail arm (l_t or l_v) is the distance between the wing aerodynamic center and the horizontal/vertical tail aerodynamic center. An approximation of the distance is required since it depends on the chord root of the tail surfaces. This distance is adjusted until it converges.

8.2 Result Redesign Loops

A number of iterations are required to determine the optimized MTOW and airframe dimensions. The initial MTOW of the 60 kW MGT is 1200.3 kg, with an endurance of 28.7 hrs, see Section 6.1 and 6.5 respectively. A mission simulation is performed with a reduced endurance, matching the endurance of the reciprocating engine. The remaining fuel after this mission simulation is 11 kg and can be removed from the total fuel weight. The engine weight reduction and lower fuel weight result in a new MTOW of 1189.3 kg. The fuel weight is 332 kg and the OEW equals 607.3 kg. The airframe dimensions are optimized for this MTOW according to the redesign process outlined in Section 8.1.1 through 8.1.3. A weight breakdown analysis determines the new component weights. The optimized MTOW is corrected by the error margin of the weight breakdown analysis. This process is iterated until the optimized MTOW converges to a certain value. The detailed results of each redesign loop are listed in Appendix I - Results Redesign Loops. These include the results of the different WERs used to determine the average components weights.

The corrected MTOW after the first redesign loop is 1083.8 kg, using an error margin of 0.19%. The OEW is equal to 501.8 kg. The new airframe dimensions are given in Table 8-1. A new mission simulation with the optimized airframe results in a remaining fuel weight of 21 kg. This can again be removed from the design to start the second redesign loop.

Table 8-1: New Dimensions for Redesign Loop 1

Wing		Fuselage		Horizontal Tail		Vertical Tail	
New Dimension	Reduction	New Dimension	Reduction	New Dimension	Reduction	New Dimension	Reduction
$b = 15.46\ m$	6.3%	$l_{Fus} = 5.25\ m$	10.1%	$b_{HT} = 2.79\ m$	10%	$b_{VT} = 1.59\ m$	12.6%
$S_w = 11.76\ m^2$	13.3%	$l_{Boom} = 4.13\ m$	9.4%	$c_{r,HT} = 0.66\ m$	13.2%	$c_{r,VT} = 0.79\ m$	13.2%
$c_r = 0.93\ m$	7.0%					$c_{mean,VT} = 0.62$	15.9%
$c_{mean} = 0.74$	15.9%						

The second redesign loop starts with an MTOW of 1062.8 kg, fuel weight = 311 kg and OEW = 501.8 kg. The corrected MTOW, after correcting the optimized MTOW with an error margin of 0.16%, is 1042.6 kg, OEW = 481.6 kg. The new optimized airframe dimensions of the second redesign loop are listed in Table 8-2. The reductions are related to the results of the first redesign loop. The aerodynamic model is updated before the mission simulation. The result of the mission simulation gives a fuel weight reduction of 8 kg. Although the modifications to the airframe begin to become negligible, the fuel weight saving is still significant to start a third redesign loop.

Table 8-2: New Dimensions for Redesign Loop 2

Wing		Fuselage		Horizontal Tail		Vertical Tail	
New Dimension	Reduction	New Dimension	Reduction	New Dimension	Reduction	New Dimension	Reduction
$b = 15.16\ m$	1.9%	$l_{Fus} = 5.16\ m$	1.7%	$b_{HT} = 2.74\ m$	1.8%	$b_{VT} = 1.56\ m$	1.9%
$S_w = 11.31\ m^2$	3.8%	$l_{Boom} = 4.05\ m$	1.9%	$c_{r,HT} = 0.64\ m$	3.0%	$c_{r,VT} = 0.78\ m$	1.3%
$c_r = 0.91\ m$	2.2%					$c_{mean,VT} = 0.62$	1.6%
$c_{mean} = 0.73$	1.4%						

The MTOW of the third redesign loop is 1034.6 kg, fuel weight = 303 kg and OEW = 481.6 kg. The airframe can again be optimized for the new MTOW. The corrected MTOW (error margin = 0.14%) is 1012.7 kg, the OEW is equal to 473.6 kg. The new airframe dimensions of the third redesign loop are given in Table 8-3. All reductions, which are related to the dimensions of the second redesign loop, are below 2% and are therefore almost marginal. However the mission simulation identifies a possible weight saving of 3 kg which requires a fourth redesign loop.

Table 8-3: New Dimensions for Redesign Loop 3

Wing		Fuselage		Horizontal Tail		Vertical Tail	
New Dimension	Reduction	New Dimension	Reduction	New Dimension	Reduction	New Dimension	Reduction
$b = 15.04\ m$	0.8%	$l_{Fus} = 5.12\ m$	0.8%	$b_{HT} = 2.72\ m$	0.7%	$b_{VT} = 1.54\ m$	1.3%
$S_w = 11.14\ m^2$	1.5%	$l_{Boom} = 4.02\ m$	0.7%	$c_{r,HT} = 0.64\ m$	0%	$c_{r,VT} = 0.77\ m$	1.3%
$c_r = 0.91\ m$	0%					$c_{mean,VT} = 0.60$	1.6%
$c_{mean} = 0.72$	1.4%						

The fourth redesign loop starts with an MTOW of 1023.6 kg and has an OEW of 473.6 kg (fuel weight 300 kg). An error margin of 0.16% is used to determine the corrected MTOW of 1021.2 kg, OEW = 471.2 kg. The results of the optimized airframe are given in Table 8-4. The mission simulation gives a possible weight saving of 0.6 kg. This minor weight saving, in combination with the marginal dimension modifications, makes a fifth redesign loop superfluous. It is therefore decided to finalize the redesign after the fourth redesign loop.

Table 8-4: New Dimensions for Redesign Loop 4

Wing		Fuselage		Horizontal Tail		Vertical Tail	
New Dimension	Reduction	New Dimension	Reduction	New Dimension	Reduction	New Dimension	Reduction
$b = 15\ m$	0.3%	$l_{Fus} = 5.11\ m$	0.2%	$b_{HT} = 2.71\ m$	0.4%	$b_{VT} = 1.54\ m$	0%
$S_w = 11.09\ m^2$	0.4%	$l_{Boom} = 4.01\ m$	0.2%	$c_{r,HT} = 0.64\ m$	0%	$c = 0.77\ m$	0%
$c_r = 0.90\ m$	1.1%					$c_{mean,VT} = 0.60$	0%
$c_{mean} = 0.72$	0%						

The new MTOW which is optimized for a 60 kW MGT is 1021.2 kg, which is a reduction of 18.3% compared to the baseline UAV with a reciprocating engine. The fuel weight reduction is 12.5% (fuel weight = 300 kg). The OEW is equal to 471.2 kg, a reduction of 28.3%. The modifications of the airframe dimensions compared to the baseline model are summarized in Table 8-5.

Table 8-5: Dimension Comparison of Redesign to Baseline UAV

Wing		Fuselage		Horizontal Tail		Vertical Tail	
b	9.1%	l_{Fus}	12.5%	b_{HT}	12.6%	b_{VT}	15.4%
S_w	18.2%	l_{Boom}	12.1%	$c_{r,HT}$	12.3%	$c_{r,VT}$	15.4%
c_r	10.0%					c_{mean}	24.1%
c_{mean}	18.2%						

Figure 8-2 through Figure 8-5 give the average component weights of each redesign loop. These figures indicate a component weight convergence after the fourth redesign loop, confirming the redundancy of a fifth redesign loop. The average MTOW of each redesign loop is given in Figure 8-6.

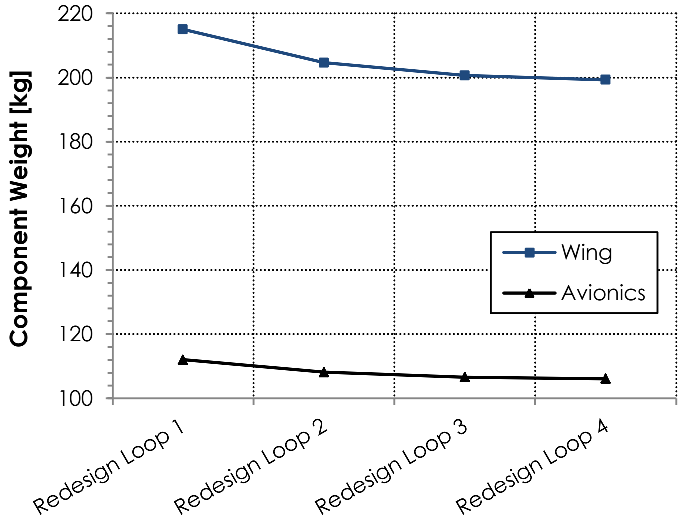

Figure 8-2: Average Weight of Wing and Avionics for Redesign Loops

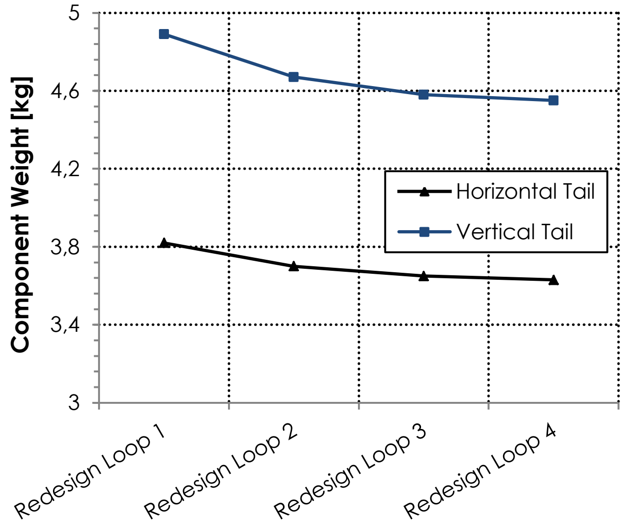

Figure 8-3: Average Weight of Horizontal and Vertical Tail for Redesign Loops

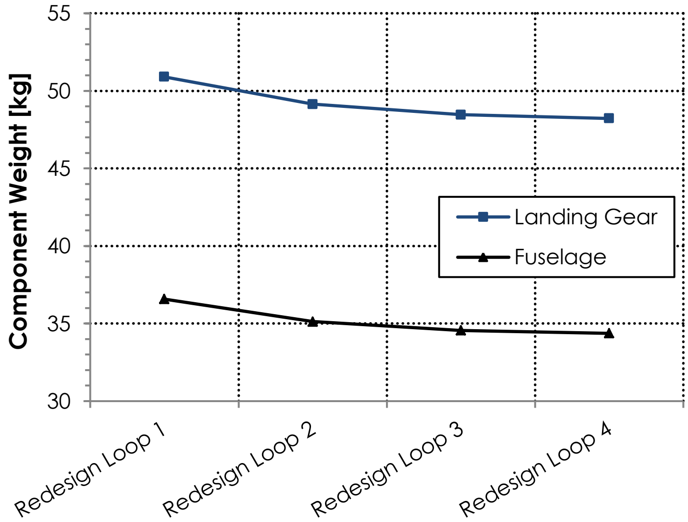

Figure 8-4: Average Weight of Landing Gear and Fuselage for Redesign Loops

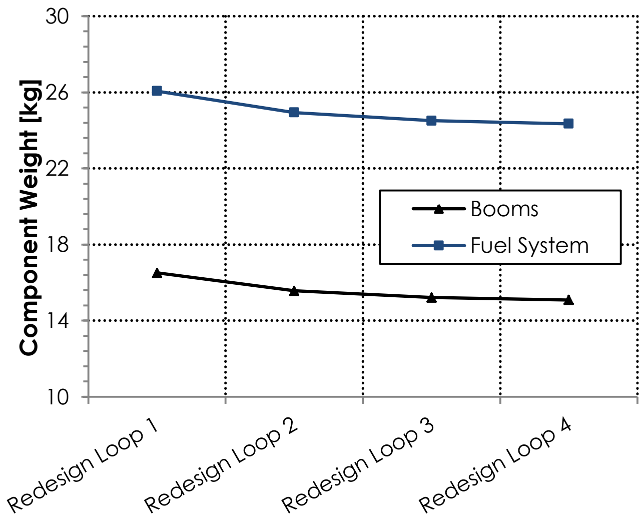

Figure 8-5: Average Weight of Booms and Fuel System for Redesign Loops

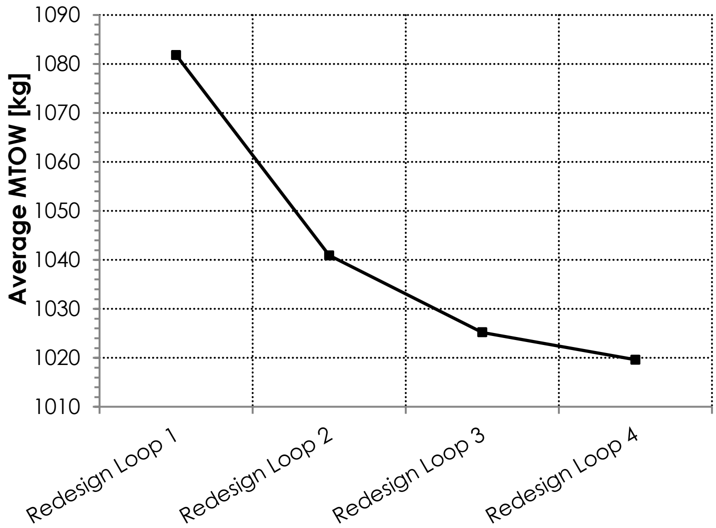

Figure 8-6: Average MTOW for Redesign Loops

8.3 Mission Performance

The mission endurance and range results for the baseline UAV with the reciprocating engine and the redesign with the 60 kW MGT - TL 4 are given in Table 8-6. The redesign UAV indicates a decrease in cruise endurance, range and fuel consumption while the descent endurance, range and fuel consumption increases. The endurance of the redesign remains unaltered compared to the reciprocating engine. The range of the redesign is reduced by 19 km, while the fuel is reduced by 43 kg.

Table 8-6: Mission Endurance, Range and Fuel Use of Baseline and Redesign UAV

	Baseline UAV			Redesign UAV		
Mission Phase	Endurance [h]	Range [km]	Fuel Consumption	Endurance [h]	Range [km]	Fuel Consumption
Climb	1.1	154	5.3%	1.1	169	6.8%
Cruise	22.3	3724	83.9%	21	3506	75.2%
Descent	3.3	446	8.1%	4.6	631	14.2%
Other	0.9	114	2.7%	0.9	113	3.8%
Total	27.6	4438	343 kg	27.6	4419	300 kg

Figure 8-7 lists the difference in mission and take-off height profiles of the baseline UAV and redesign, confirming the results of Table 8-6. The redesigned UAV is able to climb-out at a higher rate of climb during the take-off. The redesign is also able to obtain a higher climb rate during the first climb phase, until an altitude of 3700 m is reached (Figure 8-8). The baseline UAV outperforms the redesign from this altitude onwards in terms of rate of climb. The descent rate is higher for the baseline UAV for the entire descent maneuver, resulting in the shorter descent endurance compared to the redesign. The lift and drag forces and coefficients at take-off are given in Figure 8-9. Lift force and coefficient of the redesign are lower compared to the baseline UAV due to the scaled-down wing planform. The drag coefficient of the redesign on the other hand is higher due to the ground effect factor. This factor depends on the wingspan and increases as wingspan decreases, see equation 5-50. This cancels out the reduction in zero-lift drag coefficient, as a result of the smaller components, and the lift coefficient. The AoA, pitch and flight path angle during landing can be found in Figure 8-10. The AoA of the redesign is limited to α_{max}. The lift-off distance for the baseline UAV is 313 m, which is 27 m longer than the redesign ($s_{LOF} = 286\, m$). The redesign also requires a shorter landing distance ($s_{LND} = 1312\, m$) compared to the baseline UAV ($S_{LND} = 1420\, m$) as a result of the reduced gross weight.

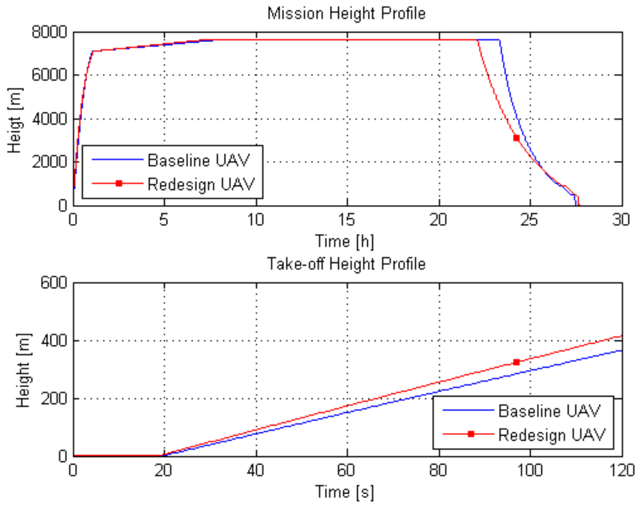

Figure 8-7: Mission and Take-Off Height Profile

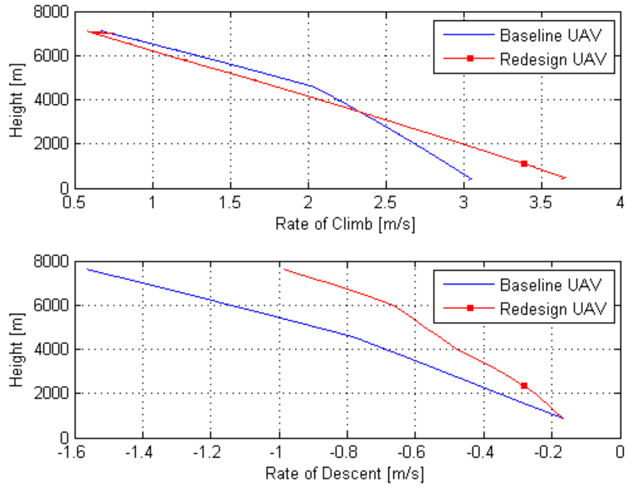

Figure 8-8: Rate of Climb and Descent

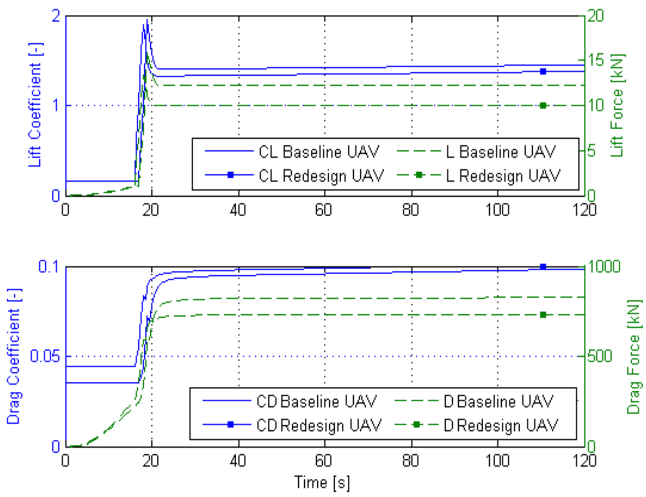

Figure 8-9: Take-Off - Lift and Drag Forces and Coefficients

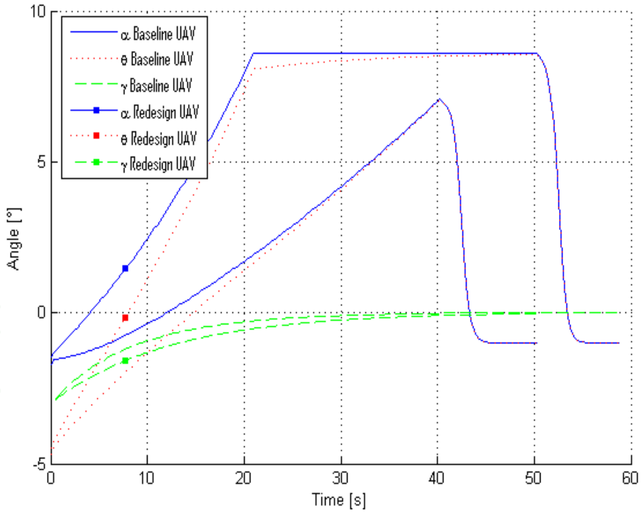

Figure 8-10: Landing - Angles

Part IV - Conclusions and Recommendations

9
Conclusions

The goal of this Master thesis was to explore the potential of civil UAVs powered by a micro gas turbine (MGT) propulsion system by analyzing the flight performance of an existing UAV and its propulsion system. The propulsion system was replaced by three different sizes of MGTs (86, 70 and 60 kW) to identify any performance gain. This was followed by a redesign to optimize the UAV platform for the new MGT propulsion system, increasing the possible performance gain.

The first step of this exploration study was to identify potential civil applications that could benefit from a MGT based propulsion system. Three application domains were defined; commercial, public safety and remote sensing applications. The range, endurance, altitude, velocity and VTOL/hover requirements of each application were determined in order to allocate a gas turbine type (turboshaft, turboprop or turbofan/turbojet) to each application. Some applications could be allocated to multiple turbine types, while most UAVs required a turboprop. The final step, in order to derive a suitable application for a UAV powered by an MGT, was to allocate the different applications with their preferred gas turbine type to the different UAV categories. A clear picture of all the civil applications together with their requirements, UAV type and propulsion system was the result. Existing UAV designs with a power range between 30 and 60 kW were analyzed in order to identify any relation between flight performance and UAV application. The selected power range only had limited previous research and differed significantly from the conventional gas turbines used to power manned aircraft. Out of the 813 UAV designs only 25 fitted within the power range each propelled by a reciprocating engine, confirming the need of the new research field. Unfortunately, no useful trends could be identified. Three promising applications were therefore selected, including the power and pipeline monitoring application which has the highest potential to be realized in the near future. The other two missions were a humanitarian application which delivers packages to remote areas and a public safety application (forest fire support). A requirement analysis concluded that all three selected applications had similar mission requirements and it was therefore decided to nominate one existing UAV which could perform all three applications.

The Harfang EADS was selected as baseline UAV and developed into a case study in combination with a mission profile. A software package was developed to numerically simulate the flight performance of the baseline UAV with the different engine types; and the optimized redesign. The mission performance was obtained by integrating point performance to path performance using Euler integration. The aerodynamic model of the baseline UAV was estimated using a combination of the vortex lattice method and the thin plate approximation to determine the lift and parasite drag coefficients. Total drag coefficient was determined using the drag polar equation in which the Oswald factor was estimated using an empirical formula. A weight breakdown analysis was used to determine the center of gravity of the UAV and the components weight of the UAV, by using weight estimation relationships of various authors to increase the accuracy. The un-weighted average of each component was added together and compared to the actual weight in order to verify the procedure. The error margin was 2.5% for the reciprocating engine and increased to 4.2% for the 60 kW MGT. Thrust and fuel consumption for the reciprocating engine were determined using data from the engine manufacturer, while thrust management tables from another Master thesis were used to model the different micro gas turbine sizes. The different gas turbine sizes that were developed, each had a number of technology levels. The take-off thrust reduced with decreasing turbine size, though increased with increasing technology level. Smaller turbine sizes could result in an underpowered UAV since the 60 kW turbine already produces 350 to 250 N less thrust at take-off, compared to the reciprocating engine. The fuel consumption of the reciprocating engine is 50% to 25% more efficient than the MGT depending on the turbine size. Also during climb thrust can be increased if the MGT technology level increases. The highest technology level does however result in the highest fuel consumption for each turbine size. The total range and endurance of the MGT can be increased if the turbine size is reduced and technology level is increased. The 60 kW MGT with a technology level of 4 (turbine inlet temperature of 1250 K and pressure ratio of 8 with a 2% efficiency increase) creates a performance gain in total range (+3%) and endurance (+4%). All other MGTs result in a lower range and endurance compared to the reciprocating engine. The climb endurance confirms the possibility of an underperforming propulsion system if the turbine size is reduced even more, since the 70 and 60 kW turbine already require 4 to 6 times as long to reach the desired cruising altitude at the lowest technology level. The mission endurance of the baseline UAV with the reciprocating engine gives however an overestimation of 2.7 hrs or 11%, partially the result of inaccuracies in the model and also due to uncertainties about the performance data of the manufacturer. A sensitivity analysis was performed to examine the influence of some of the assumed values. It was concluded that the uncertainty in the UAV dimensions could be neglected, since they had no notable effect on the mission performance. Increasing the critical Reynolds number had a significant effect on the zero-lift drag while decreasing the critical Reynolds number had a less significant effect. The influence of the total drag coefficient $(\pm 10\%)$ on the total endurance was approximately 1 to 1.5%. Modifications to the specific fuel consumption had a more pronounced effect up to 5%. The user-specified propeller efficiency showed a sensitivity of 1%.

The 60 kW MGT with a technology level of 4 was selected for the redesign. This turbine had an engine weight reduction of 50 kg compared to the reciprocating engine and could also fly for 1 h longer. This resulted in a lower MTOW for which the UAV platform could be optimized. No modifications to the UAV configuration were made in order to highlight the performance gain of the MGT. The wing, fuselage and empennage were redesigned. A total of four design iterations were required after which the results converged. This resulted in an optimized redesign with an MTOW of 1021.3 kg; a reduction of 18.3% compared to the baseline UAV (1250 kg). The fuel weight reduced by 12.5% (from 343 kg to 300 kg), while still performing the same mission profile as the reciprocating engine. The reduction in wingspan was 9% and the fuselage length reduced by 12.5%. Mission performance indicated a reduction of cruise endurance, range and fuel consumption while the descent endurance, range and fuel consumption increased. The redesign has a lower rate of climb at altitudes above 3700m, while take-off and landing distances reduced.

This exploration study concludes that there is a performance gain possible if a reciprocating engine is replaced by an MGT. This performance gain can be transformed into a fuel weight reduction, proving the potential of civil UAVs powered by an MGT based propulsion system. Civil UAV applications could benefit from this technology, conceivably increasing the number of civil UAVs in operation.

10
Recommendations for Future Research

Having concluded the results of this Master thesis, a number of recommendations for future research are discussed. It should be noted that this Master thesis served as an exploration study investigating this new research field of UAVs powered by micro gas turbines. Numerous research projects can therefore be developed following from this work.

- Both engine types perform the same mission profile. However, one can imagine that different optimum climb and descent procedures exist for each engine type. For example, climbing to a certain altitude with flaps set to take-off setting, followed by a level flight segment to gain airspeed to finally perform the climb maneuver to the desired cruising altitude. Fixed mission profiles could be replaced by optimized mission profiles depending on the engine type.
- The software package developed enables numerous mission simulations to be analyzed in combination with a coupling to GSP. This could become a powerful tool for analyzing different mission profiles of different UAV design, for example simulating low velocity and altitude missions.
- The criteria to obtain maximum endurance during the different mission phases are derived assuming constant power available curves. These curves are however an analytical approximation. The velocity corresponding with the maximum endurance can be derived from fuel flow as function of airspeed curves.
- The take-off and landing simulations can be extended by adding the ground effect to the lift coefficient. Also a more elaborate braking maneuver can be included by implementing the braking slip ratio.
- The accuracy of the aerodynamic model can be increased by performing CFD analysis and windtunnel tests. A more accurate determination of the critical Reynolds number of each component could however already provide some improvements with relatively small effort. A more extensive method to determine the Oswald factor will further aid the analysis. Multiple methods could be combined to obtain a more accurate estimation of the Oswald factor.
- The propeller model could be improved by using propeller maps instead of a user-specified propeller efficiency. An option can also be added to simulate other propeller types, including a variable pitch and constant speed propeller. The manufacturer of the reciprocating engine defines a constant speed propeller as most suitable for the reciprocating engine, while a variable pitch propeller also performs well but adds complexity during operation. The same propeller model is used to model MGT. The propeller should however be scaled-down as engine power output is reduced.
- The results of the propulsion analysis of the reciprocating engine were obtained from data provided by the manufacturer. This entailed some uncertainties, especially in the specific fuel consumption. This data can be validated by comparing it with actual performance data of the reciprocating engine installed on a static or flight test bed.
- Different turbine configurations can be developed including turboshafts and turbofans, hereby increasing the number of applications which could benefit from an MGT based propulsion system.

Bibliography

[Front Cover] *MQ-9 Reaper UAV.* n.d. [image online] Available at: http://freewidescreenwallpapers.blogspot.be/2008/07/mq-9-reaper-uav-1680-x-1050-widescreen.html [4 March 2015].
[1] Barnard, J., 2008. The Use of Unmanned Aircraft in Exploration and Production Activities. *23rd Bristol International UAV Systems Conference.* Bristol, 7 April 2008.
[2] Department of Defense (DoD), 2007. *Unmanned Systems Roadmap 2007 - 2032.* [Pdf] Available at: http://www.globalsecurity.org/intell/library/reports/2007/dod-unmanned-systems-roadmap_2007-2032.pdf [14 April 2014].
[3] Gertler, J., 2012. *U.S. Unmanned Aerial Systems.* [pdf] Congressional Research Service. Available at: http://fas.org/sgp/crs/natsec/R42136.pdf [23 April 2014].
[4] Austin, R., 2010. *Unmanned Aircraft Systems UAVs Design, Development and Deployment.* Chichester: John Wiley & Sons Ltd.
[5] Marcellan, A., 2015. *An Exploration into the Potential of Microturbine Based Propulsion Systems for Civil Unmanned Aerial Vehicles*. MSc. Delft University of Technology.
[6] Gundlach, J., 2012. *Designing Unmanned Aircraft Systems: A Comprehensive Approach*. Blacksburg: AIAA Education Series.
[7] Keane, J.F. and Carr, S.S., 2013. A Brief History of Early Unmanned Aircraft. *Johns Hopkins Apl Technical Digest,* [online] Available at: http://www.jhuapl.edu/techdigest/TD/td3203/32_03-Keane.pdf [15 September 2014].
[8] Allen, J. and Walsh, B., 2008. Enhanced Oil Spill Surveillance, Detection and Monitoring through the Applied Technology of Unmanned Air Systems. In: American Petroleum Institute, *International Oil Spill Conference.* Savannah, May 2008. Derry: Vermillion.
[9] Horcher, A. and Visser R.J.M., 2004. Unmanned Aerial Vehicles: Applications for Natural Resource Management and Monitoring. In: Council on Forest Engineering (COFE), *Machines and People, The Interface.* Hot Springs, 27-30 April 2004.
[10] De Fátima Bento, M., 2008. Unmanned Aerial Vehicles: An Overview. *Inside GNSS,* [online] Available at: http://www.insidegnss.com/auto/janfeb08-wp.pdf [27 March 2014].
[11] AIAA, 2013. *2013 - Worldwide UAV Roundup*, [pdf] Available at: http://www.aerospaceamerica.org/Documents/AerospaceAmerica-PDFs-2013/July-August-2013/2013_UAV%20Chart.pdf [25 March 2014].
[12] van Blyenburgh, P., 2010. *UAV: The Global Perspective with a Focus on Light UAS.* [Online] UVS-Tech 2010 Moscov. Available at: http://uvs-info.com/index.php?option=com_phocadownload&view=category&id=256:a-presentations&Itemid=381&limitstart=20 [22 April 2014].
[13] Clothier, R.A., et al., 2011. Definition of an airworthiness certification framework for civil unmanned aircraft systems. In: *Safety Science 49 (6).* July 2011. Kidlington: Elsevier Ltd.
[14] Utt, J., McCalmont, J. and Deschenes, M., 2005. Development of a Sense and Avoid System. In: AIAA, *Infotech@Aerospace Conference 2005.* Arlington, 26-29 September 2005.
[15] Finn, R.L. and Wright, D., 2012. Unmanned aircraft systems: Surveillance, ethics and privacy in civil applications. In: *Computer Law & Security Review.* London, 2012.
[16] Koldaev, A. V., 2007. Non-Military UAV Applications. *Aero India International Seminar - 2007 Edition.* Bangalore, February 2007.
[17] Mueller, T.J. and DeLaurier, J.D., 2003. Aerodynamics of Small Vehicles. *Annual Review Fluid Mechanics,* [Online] Vol. 35. Available through: Delft University of Technology [4 April 2014].
[18] Pines, D.J. and Bohorquez, F., 2006. Challenges Facing Future Micro-Air-Vehicle Development. *Journal of Aircraft*, [Online] Vol. 43, No. 2. Available through: Delft University of Technology [4 April 2014].
[19] McMasters, J. H., and Henderson, M. L., 1980. Low Speed Single Element Airfoil Synthesis. *Technical Soaring*, Vol. 6, No. 2.
[20] Baxter, D., and East, R., 1999. A Survey of Some Fundamental Issues in Micro-Air-Vehicle Design. In: *Proceedings of the 14th Bristol International Conference on UAV Systems*. Bristol: University of Bristol.
[21] Martinez-Val, R. and Hernandez, C., 1999. Preliminary Design of a Low Speed, Long Endurance Remote Piloted Vehicles (RPV) for Civil Applications. In: *Aircraft Design*, Vol. 2, No 2. Kidlington: Elsevier Ltd.
[22] Carmichael, B. H., 1981. Low Reynolds Number Airfoil Survey. Vol. I, NASA CR 165803.
[23] Raymer, D.P., 1992. *Aircraft Design: A Conceptual Approach.* Second Edition. Reston: AIAA.
[24] Roskam, J., 1985. *Airplane design. Part I: preliminary sizing of airplanes*. Ottawa: Roskam Aviation Engineering.
[25] Torenbeek, E., 1984. *Synthesis of Subsonic Airplane Design.* Delft: Delft University Press.
[26] Harmon, F.G., Frank, A.A and Chattot, J., 2006. Conceptual Design and Simulation of a Small Hybrid-Electric Unmanned Aerial Vehicle. *Journal of Aircraft*, [Online] Vol. 43, No. 5. Available through: Delft University of Technology [21 May 2014].

[27] Roling, P., Cooper, R. and Curran, R., 2008. International Design Synthesis Exercise 2006: Design of an Interceptor UAV. In: *Aerospace Science Meeting and Exhibit 2008.* Reno, 7-10 January 2008.
[28] Veerman, H.C.M., 2012. *Preliminary multi-mission UAS design.* Msc. Delft University of Technology. Available at: http://repository.tudelft.nl/view/ir/uuid%3A6762136d-5f8c-46a8-9ee5-18347c43fc0e/ [31 March 2014].
[29] Altman, A., 2000. *A Conceptual Design Methodology for Low Speed High Altitude Long Endurance Unmanned Aerial Vehicles*. Ph.D. Cranfield University. Available at: https://dspace.lib.cranfield.ac.uk/handle/1826/3998 [21 October 2014].
[30] Barnard Microsystems Limited, 2014. *UAV Design Guidelines.* [online] Available at: http://www.barnardmicrosystems.com/UAV/uav_design/guidelines.html [21 August 2014].
[31] Rodgers, C., 2001. Turbofan Design Options for Mini UAV's. In: AIAA, *37th AIAA/ASME/SAE/ASEE Joint Propulsion Conference and Exhibit.* Salt Lake City, 8-11 July 2001.
[32] Epstein, A.H., et al. 2000, Shirtbutton-sized gas turbines: the engineering challenges of micro high speed rotating machinery. In: *Proceedings of the 8th International Symposium on Transport Phenomena and Dynamics of Rotating Machinery*, Hawaii, 26–30 March 2000 [16 April 2014].
[33] Decuypere, R., 2005. Micro Turbines from the Standpoint of Potential Users. In: NATO Science and Technology Organization, *Micro Gas Turbines.* Neuilly-sur-Seine, December 2005.
[34] Van den Braembussche, R.A., 2005. Micro Gas Turbines - A Short Survey of Design Problems. In: NATO Science and Technology Organization, *Micro Gas Turbines.* Neuilly-sur-Seine, December 2005.
[35] Barnard, J., 2013. *The requirements for unmanned aircraft operating in oil, gas and mineral exploration and production*. [Pdf] AUVSI Unmanned Systems North America 2013 Conference. Available at: http://www.barnardmicrosystems.com/media/presentations/Barnard.Joseph.presentation%20at%20AUVSI%202013.pdf [21 March 2014].
[36] Airbus Defence & Space, 2013. *SIDM/Harfang*. [Pdf] Elancourt: Airbus Defence & Space. Available at: http://www.defenceandsecurity-airbusds.com/web/guest/harfang-pdf [29 July 2014].
[37] General Atomics Aeronautical, 2013. *MQ-1 Predator Persistent ISR and Strike.* [Pdf] Poway: General Atomics Aeronautical. Available at: http://www.ga-asi.com/products/aircraft/pdf/MQ-1_Predator.pdf [29 July 2014].
[38] Writer, S., 2011. *The South African Denel Dynamics Bateleur is an impressive looking UAV system.* [Online] Available at: http://www.militaryfactory.com/aircraft/detail.asp?aircraft_id=908 [29 July 2014].
[39] Ruigrok, G.J.J., 2009. *Elements of airplane performance.* Second Edition. Delft: VSSD.
[40] Gerard, W.H., 1998. Prediction of Sailplane Wing Weight for Preliminary Design. In: *Weight Engineering, A98-37633.* Spring.
[41] Yi, Z., Heping, W., 2006. A Study of Structure Weight Estimating for High Altitude Long Endurance (HALE) Unmanned Aerial Vehicle (UAV). *25th International Congress of The Aeronautical Sciences*, Hamburg, 3-8 September 2006.
[42] Howe, D., n.d., *Course Notes DAet 9317, 9218 and 9484.* Cranfield University.
[43] Palumbo, D.J., 2000. Unmanned Systems 2000 Proceedings. *UAVSI,* Orlando, 2000.
[44] Nicolai, L., 1984. *Fundamentals of Aircraft design.* Fairborn: E.P. Domicone Printing Services.
[45] Murua, J., Palacios, R. and Graham, J.M.R., 2012. Applications of the Unsteady Vortex-Lattice Method in Aircraft Aeroelasticity and Flight Dynamics. In: *Progress in Aerospace Sciences*, Vol. 55. Kidlington: Elsevier Ltd.
[46] Anderson, J.D., 2007. *Fundamentals of Aerodynamics, Fourth Edition*. New York: The McGraw-Hill Companies.
[47] Nicolai, L.M., 2000. *Estimating R/C Model Aerodynamics and Performance*. [Online] (June 2000) Available at: http://www.ebah.com.br/content/ABAAAAEeUAI/projeto-aerodinamico-aplicado-a-aeromodelos [26 January 2015].
[48] Gur, H. et al., 2009. Full Configuration Drag Estimation. *27th AIAA Applied Aerodynamics Conference,* San Antonio, 22-25 June 2009.
[49] Hoerner, S.F., 1965. *Fluid Dynamic Drag.* Bakersfield: Hoerner Fluid Dynamics.
[50] Shevell, R.S., 1989. *Fundamentals of Flight,* New Jersy: Prentice-Hall.
[51] Jobe, C.E., 1989. Prediction and Verification of Aerodynamic Drag, Part I: Prediction. In: *Progress in Astronautics and Aeronautics,* New York, 1989.
[52] Sadraey, M., 2009. *Aircraft Performance Analysis.* VDM Verlag Dr. Muller.
[53] Rotax Aircraft Engines, 2010. *Operators Manual for Rotax Engine Type 914 Series.* [Pdf]. Rotax Aircraft Engines. Available at: http://contrails.free.fr/fichiers2/914_owners_man_d05240.pdf [29 November 2014].
[54] Rotax Aircraft Engines, 2012. *Powerful Light Efficient*. [Pdf]. Rotax Aircraft Engines. Available at: http://www.rotax-owner.com/pdf/brochure-all.pdf [1 December 2014].
[55] NLR, n.d. *Gas Turbine Simulation Program*. [Online] Available at: http://www.gspteam.com/ [9 March 2015].
[56] Torenbeek, E., 1998. *Optimum Cruise Performance of Subsonic Transport Aircraft.* Delft: Delft University Press.

Part V - Appendices

A. UAV Design Configuration

A brief description of the UAV design configuration options is given with the advantages and disadvantages of each option, according to J. Gundlach **[6]**. The wing system, tail configuration, fuselage layout, engine integration and landing gear arrangement are discussed.

Wing System Configuration

A wing system configuration consists of all the lifting surfaces and pitch trim surfaces, since it is responsible for generating the appropriate amount of lift, pitch stability and control of the UAV. Most configurations have separate surfaces to perform these functions; a flying wing combines the functions resulting into only one horizontal surface. Other main configurations are the conventional, canard, tandem wing and the three surface configuration, illustrated in Figure A-1. Many other configurations are however possible but are not discussed into detail. The conventional configuration has a main wing and a smaller horizontal stabilizer or elevator located aft of the main wing to provide pitch stability and control. This is also the conventional configuration for manned aircraft and is therefore well understood and relatively simple to analyze. One of the advantages of splitting the lift generation, the longitudinal stability and control is that the main wing can be designed and optimized for lifting capabilities and aerodynamic efficiency without any longitudinal or control requirements. This means that the main wing can generate high lift coefficients. The main wing also experiences little influence of the horizontal tail which means that a conventional configuration can yield in high lift-to-drag ratios. The conventional configuration has a positive longitudinal static stability since the C.G. is located ahead of the neutral point. Careful analysis is however required to prevent a deep stall in which the horizontal tail is submerged into the wake of the main wing eliminating the chance of recovering the aircraft. This problem can be avoided if a canard configuration is used. A canard configuration also uses a smaller horizontal surface, called the canard, for longitudinal stability and control but this surface is located ahead of the main wing. The canard can therefore never be submerged into the wake of the main wing. The canard should however stall before the main wing in order to have a stable configuration. This results in a lower maximum lift coefficient for the main wing which also has to deal with the negative effects of the downwash generated by the canard. The aerodynamic performance of a canard configuration is therefore generally lower than a conventional configuration. One of the advantages regarding the canard configurations is that all horizontal surfaces generate positive lift; whereas with a conventional configuration only the main wing generates positive lift, since the horizontal tail produces negative lift for stability reasons. The fuselage packing can also be more efficiently distributed since the center of gravity is located on the moment arm between the two surfaces. Despite these advantages, canard configurations are rarely used for UAV design due to the aforementioned lower aerodynamic performance compared to a conventional configuration. A three-surface configuration has a canard, main wing and horizontal tail surface. This configuration combines the advantages of both configurations regarding the aerodynamic efficiency and center of gravity range. It does however increase the part count and control complexity, offsetting the potentially higher aerodynamic efficiency compared to a conventional configuration.

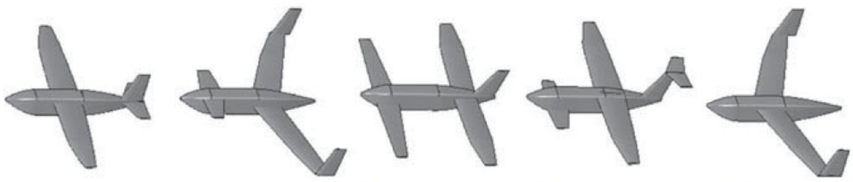

Figure A-1: Main Wing System Configurations [6]

A tandem wing configuration has two wings, one in front of the other, of similar dimensions. This configuration has a low aerodynamic efficiency since the aft wing is submerged into the downwash of the forward wing. This increases the induced drag component of the aft wing. This downwash also influences the stall behavior of the tandem wing configuration. The aft wing will stall first if two wings with similar characteristics are being used resulting in an unstable configuration. The design of the front wing needs to be altered to favor front-wing stall. The advantage of this configuration is that the center of gravity is located between the two wings. However, only a small amount of UAVs use this configuration. A final configuration discussed into here is the flying wing. This configuration combines the lift generation, longitudinal stability and control into one single surface creating a simple design. This configuration produces however less lift compared to a conventional configuration, requiring either a higher take-off and landing velocity or an increased surface area. The flying wing is therefore less suited for long endurance missions. A flying wing does not have the drag contributions of a horizontal tail or canard. The flying wing is the second most used configuration for UAVs after the conventional configuration. Other wing system configurations are non-planar wings, freewings and parafoils, but are not being discussed here due to the small application area.

Tail Configuration
A UAV can have multiple tail configurations, most of them are also used on manned aircraft. The selected configuration has generally little impact on the total UAV drag. This means that the selection can be based on other design criteria then aerodynamic efficiency. Often a distinction between a single-boom and twin-boom is made, see Figure A-2. The possible tail configurations of a single-boom are conventional, cruciform, T-tail, conventional inverted, H-tail, V-tail, inverted V and X-tail. The twin-boom variants are conventional, twin-boom H, twin-boom T and twin-boom inverted V. The inverted tail configurations have a limited rotation angle in order to prevent tail strikes and therefore require a longer landing gear or take-off length. The vertical tail can however be used to protect the propeller in case of a pusher engine configuration. The popular pusher engine configuration is also one of the reasons why UAVs use a twin-boom configuration. V-tails and X-tails have the advantage of combining the horizontal and vertical tail, thereby reducing the parts count. The tail configuration can also be beneficial for engine noise blocking.

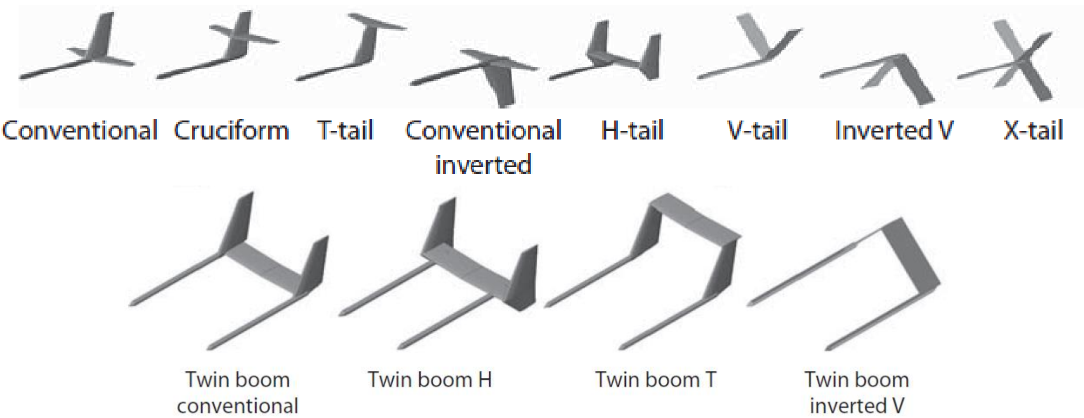

Figure A-2: Single-Boom and Twin-Boom Tail Configurations [6]

It is also possible to disconnect the vertical tail from the horizontal tail. This is often used in combination with a canard or flying wing configuration. The following options are presented in Figure A-3: single vertical, twin-boom vertical, winglet vertical, inverted winglet vertical and twin verticals on the fuselage. Winglets do not only serve as drag reduction devices but also as vertical stabilizers. The vertical tails of a UAV are also often designed to only cope with the crosswind load. They do not have to counteract the moment caused during one-engine out operations since most UAVs only have one engine located on the body symmetric axis. Vertical surfaces are ideal to house several antennas, eliminating the extra drag of installing a dedicated antenna surface.

Figure A-3: Vertical Stabilizer Configurations [6]

Fuselage Configuration

UAV fuselages are responsible for housing the payloads, avionics, energy sources, engine and the landing gear. They also connect the major elements of a UAV like the wings, empennage and landing gear to each other. Yet a fuselage only decreases the overall performance of the UAV. The negative impacts on the aerodynamics, stability and weight should be minimized as much as possible by designing a low drag and lightweight structure. Fortunately, the packing of a UAV fuselage can be much tighter since no humans need to be housed inside the fuselage. Therefore the fuselage can be shaped to minimize drag, attention should however be paid towards a proper cooling for the electronics. One can define a fuselage by giving a distribution of the width and height, and the cross-sectional shapes. Rectangular cross-sections are common because of their simplicity but sharp edges should be rounded as much as possible to lower the drag. Some UAV fuselages have a distinct bump at the front of the fuselage. This is necessary to house a gimbaled antenna used for satellite communications. The fuselage protects the antenna from the environmental conditions but should not block the transmitted signals.

Engine Integration

Most UAVs only use one engine located on the body symmetric axis providing a centerline thrust component. Wing mounted engines are therefore rarely used on UAVs which reduces the required vertical tail volume. Turbofan and turbojet engines are either buried inside the fuselage or mounted as podded engines on the fuselage, see Figure A-4. Podded engines are easy to install and maintain but increase the wetted area of the UAV and induce an increase in drag. Buried engines on the other hand do not create additional drag, or only by a small margin, but can be hard to reach. It can be beneficial to install the engine on the upper part of the fuselage to lower the noise and infrared signatures, since the fuselage acts as a blockage. Reciprocating, electrical and turboprop engines are installed as a tractor or pusher configuration. The propeller of a tractor configuration has a clean airflow resulting in a higher propeller efficiency and lower noise pollution. It also moves the center of gravity forward. A disadvantage of a tractor configuration is that the propeller can obstruct the forward viewing field of various optical equipment. Furthermore, the exhaust of a forward engine can interfere with sensitive payloads. Therefore, most UAVs use a pusher configuration to have a clear forward viewing field despite some negative effects on the propeller efficiency. The lower propeller efficiency is the result of the wake coming from the fuselage. An aft engine location makes the UAV tail heavy. The center of gravity can however be moved forward by using a shaft extension.

Figure A-4: Podded Turbofan or Turbojets Configurations [6]

Landing Gear Arrangement

There are numerous ways to launch and recover a UAV. A landing gear is considered to be the conventional launch and recovery method. It supports the UAV during take-off, landing and taxi but is however not mandatory. Due to their smaller size and weight, compared to manned aircraft, UAVs often do not have a landing gear and use other launch and recovery methods. The goal of the launch phase is to accelerate the UAV to an initial flight speed, called V_{LOF}, great enough to sustain a controlled flight. A higher acceleration reduces the take-off length but increases the loads endured by the UAV. The acceleration can either be provided by the engine, an external system or a combination of the two. UAVs with a MTOW above 450 kg use a landing gear since other methods become impractical or impossible. The smaller the scale the more launch and recovery methods become available. A UAV can be hand launched by an operator, but this method becomes impractical if the UAV weighs more than 10 kg or has a wingspan over 3 meters. Hand launches also require a certain skill and success rates can be low. Other possibilities are rail launched, rocket launched and air launched. During a rail launch the UAV is attached to a cart which is mounted on a rail. The cart is accelerated by pneumatic or hydraulic pressure. Rail launchers are used up to an MTOW of 225 kg. A rocket launch is used when no alternatives are possible or if the UAV requires a higher launch velocity. If this launch method is used, the UAV can be designed for cruise conditions. Target drones and supersonic UAVs often use this technique. An air launch consists of dropping a UAV from a flying manned aircraft and is also often used by target drones.

The recovery phase is generally more challenging than the launch phase. During the recovery phase the UAV has to be decelerated to rest, absorbing the energy of the forward motion. A means of dissipating that energy is required. Again several techniques exist. A UAV can make a belly landing or fly into a net. The risk of damaging the UAV by using these methods is however high. Net recovery becomes impractical above a MTOW of 450 kg. The risk of damaging the UAV can be lowered if a conventional landing gear is used, either in combination with wheel brakes, hook and cable or drogue parachute. Smaller UAVs can use a combination of an airbag and parachute. Some UAVs also enter a deep stall as recovery method.

B. Propulsion Types

The main propulsion systems which power UAVs are discussed according to J. Gundlach **[6]**. These include electric engines, reciprocating engines, gas turbines and other propulsion systems (hybrid engine, rocket propulsion, ornithopters, nuclear power, gilder aircraft).

Electric Engines

An electric engine requires a propeller to produce thrust. This means that it can only be used up to airspeeds around Mach 0.6. At higher airspeeds the propeller tip velocity becomes sonic, resulting in a detrimental performance decrease. There is however no drop in performance if the altitude is increased since an electric engine is a non-breathing system. They also have a lower acoustic and thermal signature compared to other propulsion systems enhancing the stealth capabilities of a UAV. The nearly constant torque produced by the electric engine reduces the structural loads on the propeller. This means that thinner and lighter blades can be used resulting in a more efficient propeller. The nearly constant torque also lowers the vibrations, this in combination with the low number of moving parts increases the time between engine overhaul. Furthermore, electric engines do not consume any liquids like fuel and lubricants and do not produce any emissions. Other advantages are the excellent starting and stopping characteristics and the ease to custom build the engine in order to suit the power requirements. The largest disadvantage of an electric engine is mainly related to the energy source. Batteries and solar panels have a lower energy density potential compared to fuel based systems like hydrogen and kerosene **[33]**. This means that more energy is contained in 1 kg of fuel than in a 1 kg weighing battery. Not only do fuel based systems have a higher energy density potential, they also have a power density advantage **[33]**. A longer period is needed to extract the energy from a battery than from a fuel based system. Batteries also lose energy over time due to their natural discharge behavior **[33]**. All these factors result in low endurance missions. The endurance of an electric powered UAV is usually around 0.5 to 3 hours. The limited endurance can however be solved by using fuel cells or solar panels as energy source. The fuel cell technology is however not matured enough to be used efficiently on civil UAVs. The electric engine is therefore ideal for small, low speed and endurance UAVs.

Reciprocating Engines

Reciprocating engines come in many forms. The most common are the two-stroke, four-stroke and rotary engines. A two-stroke engine has a power stroke at each revolution of the crankshaft whereas a four-stroke engine has its power stroke every other revolution. The rotary engine on the other hand has a smoother power delivery compared to the two and four-stroke engines, causing a minimum number of vibrations. Rotary engines also have a low mass to power ratio but require a reduction gearbox and high levels of cooling. This makes the weight of rotary engines comparable to that of a four-stroke engine. The lightest and cheapest of the three is the two-stroke engine but it has a higher specific fuel consumption due to the fact that intake gases are being contaminated by the exhaust gases, making it less efficient. A two-stroke engine uses 0.4 kg/kWh while a four-stroke engine uses 0.3-0.4 kg/kWh, full power will however increase the fuel consumption of both engine types. Since, a reciprocating engine is an air-breathing engine the performance decreases if the altitude increases. A turbocharger or super charger is needed to cope with the decreasing performance making the engine heavier, more complex and more expensive. Similar to an electric engine is the fact that a reciprocating engine also needs a propeller to convert the energy into a thrust force. This means that the aforementioned issues with flight velocities above Mach 0.6 also prevail for reciprocating engines. The endurance of these engine types depends on the size of the fuel tank but can be up to 30 hrs. Two-stroke engines are mostly used for the short range, smaller UAVs whereas the long range, larger aircraft use a four-stroke engine.

Gas Turbines
A turbine can come in four main forms: turboshaft, turboprop, turbofan and turbo jet. The turboshaft is used for UAVs which require VTOL/hover. A turboprop can be used, similar to the electric and reciprocating engine, up to flight speeds of Mach 0.6. Turbofan engines are used for higher flight speeds up to the low supersonic speeds. Turbojets become the most efficient propulsion system for the supersonic flight regime. Turbines have a nearly uniform power delivery and are more quiet than reciprocating engines. They also have low mass to power ratios and have minimal fuel consumption at maximum power. Some disadvantages compared to the electric and reciprocating engine are the significant lag in response and acquisition costs. They have however fewer moving parts which results in a long mean time between overhauls compared to reciprocating engines. The few moving parts and continuous combustion also cause minimal vibration increasing the reliability of the engine. Turbine engines are usually used for high altitude, fast flying, larger UAVs. The reason for the low number of UAVs powered by a turbine is caused by the fact that the lower power range turbines are not economical yet. The engines are simply not available for the smaller UAVs despite the advantages compared to the electric and reciprocating engines.

Other Propulsion Systems
Apart from the three aforementioned propulsion systems some other systems exist, the use of these systems is however limited. Some of them are not even being used to power UAVs and are only considered as concepts. In total five other propulsion systems will be briefly discussed, beginning with a hybrid engine. A hybrid engine is a combination of two propulsion systems. Any hybrid combination between each of the three aforementioned propulsion systems is possible, although mostly an electric engine is combined with a turbine or reciprocating engine. This means that the advantages of both propulsion systems are combined into one system. This comes with a weight penalty since two engines together with their own sub-systems have to be installed on the aircraft. A UAV could also be powered by rocket propulsion. This type of propulsion could however only be used for a relatively short amount of time. It is therefore mostly used during take-off to decrease the required take-off distance. Ornithopters which use the flapping motion of their wings as a propulsion system are becoming more popular to power the MAV UAVs. The design and analysis of such a system is however a technical challenge due to the complex kinematics and aerodynamics involved. Another propulsion system could be achieved by using nuclear power resulting in ultra-long endurance missions. This propulsion system comes however with many safety issues and ethical questions. The required shielding to block the radiation would also result in a heavy and bulky engine. Nuclear power has not yet been used to power UAVs although some concepts have been proposed in the past. A final propulsion system that is being discussed is a glider aircraft. Although gilders do not use an engine, one can argue that this type of aircraft converts its potential energy into kinetic energy by trading height into horizontal distance and speed.

C. Civil Application with Requirement Details

Application			Requirements: Range	Endurance	Altitude	Speed	VTOL/Hover	Type
Commercial	**Aerial photography**	Urban	Short	Short	Low	Low	Yes	MAV to CR
		Mapping	Medium to long	Medium to long	Medium to high	Low to medium	No	SR to HALE
	Agriculture	Crop monitoring and spraying	Short to medium	Short to medium	Low to medium	Low to medium	Yes	MAV to MR
		Herd monitoring and driving	Short to medium	Medium to long	Low	Low to medium	Yes	CR to SR
	Utility companies (gas, oil & electricity): Power and pipeline inspection		Medium to long	Medium to long	Low to medium	Low to medium	No	MR to LR
	Mining companies: Looking for minerals		Medium to long	Medium to long	Medium	Low to medium	No	MR to LR
	Courier service: Delivering packages		Short to long	Short to medium	Low to high	Low to high	Yes	MAV to EN
	Information services: News information and broadcasting		Short	Short	Low	Low	Yes	MAV to CR
	Telecommunications		Long	Long	High	Medium to high	No	EN to HALE
	Private security		Short	Short	Low	Low to medium	Yes	MAV to CR
Public Safety	**Coastguard**	SAR Coast and sealine monitoring	Long	Medium to long	Medium to high	Low to high	No	EN to HALE
	Police authorities	Security and incident surveillance	Short to medium	Short to medium	Low to medium	Low to medium	Yes	MAV to MR
	Emergency support	SAR Delivering emergency supplies	Short to long	Short to medium	Low to medium	Low to high	Yes	MAV to LR
	Fire service	Forest fire detection and damage assessment	Long	Medium to long	Medium to high	Low to medium	No	EN to HALE
		Forest fire fighting Communication	Short to medium	Short to medium	Low to medium	Low to medium	Yes	MAV to MR
	Lifeboat institutions: Incident investigation, guidance and control		Long	Medium to long	Medium to high	Low to high	No	EN to HALE
	Customs and excise: surveillance for illegal imports		Long	Medium to long	Medium to high	Low to high	No	EN to HALE
	Local authorities: disaster control		Short to medium	Short to medium	Low to medium	Low to medium	Yes	MAV to MR
	Traffic agencies: Monitoring and control of traffic		Short to medium	Short to medium	Low	Low	Yes	MAV to SR

	Application		Requirements					Type
			Range	Endurance	Altitude	Speed	VTOL/Hover	
Remote Sensing	**Conservation**: Pollution, land and wildlife monitoring		Long	Medium to long	Medium to high	Low to medium	No	EN to HALE
	Fisheries: Fisheries protection		Long	Medium to long	Medium to high	Medium to high	No	EN to HALE
	Meteorological services: Sampling and analysis of atmosphere		Long	Medium to long	Medium to high	Low to high	No	EN to HALE
	Survey	Geographical Geological	Long	Medium to long	High	Low to medium	No	EN to HALE
		archaeological	Short	Short	Low	Low	Yes	MAV to CR
	River Authorities: Water course and level monitoring		Medium to long	Medium to long	Low medium	Low to medium	No	MR to LR
	Atmospheric Satellite		Ultra long	Ultra long	High	High	No	HALE
	Ice reconnaissance		Medium to long	Medium to long	Low to medium	Medium to high	No	MR to LR

Requirement Legend

Range	Endurance	Altitude	Speed
Short: 0 - 70 km	Short: 0 - 3 hr.	Low: 0 - 3,000 m	Low: 0 - 100 km/h
Medium: 70 - 500 km	Medium: 3 - 12 hr.	Medium: 3,000 - 5,000 m	Medium: 100 - 350 km/h
Long: 500 - 20,000 km	Long: 12 - 48 hr.	High: 5,000 - 20,000 m	High: > 350 km/h
Ultra long: 20,000 - ∞*	Ultra long: 48 - ∞*		

(*Depending on the available technology)

D. Existing UAVs within the 30-60 kW Power Range

Country	Manufacturer	Designation	Status	Launch Method	Propulsion	Type	Endurance [hr.]	Range [km]	Ceiling [m]	Power [kW]	MTOW [kg]	Payload [kg]	Max Airspeed [km/h]	Cruise Speed [km/h]	Wing/ Rotor Span [m]
Austria	Schiebel Camcopter S-100	Camcopter S-100	In production		Reciprocating	VTOL	6	180	5500	41	200	50	222	185	3.4
	Diamond Aircraft	Diamond Hero	In development		Reciprocating		6.5			40		113			
India	Kadet Defense Systems	MSAT-500/NG	Deployed	Bungee catapult or pneumatic	Reciprocating	delta wing	1.75	10	5000	30	82				2.75
Israel	UVision Global Aero Syst	Butterfly	Under way		Reciprocating	Paraglider	4	115		48	450	230		55	
Italy	Selex Galileo Avionica	Falco	In production	Ground launched, catapult launched	Reciprocating	MALE TUAV	14	190	6500	48	420	70	216		7.2
Malaysia	CompositeTechn. Research	Aludra Mk 1	Deployed	Ground launched	Reciprocating	Fixed Wing	3	48	3658	37	200	25		220	6
Netherlands	High Eye B.V.	HEF150	Under way	Ground launched	Reciprocating	VTOL	7			41		50			3.15
Norway	CybAero	APID 60	Under way	Ground and ship launched	Reciprocating	VTOL	8	200		41	180	50	150	90	3.3
Pakistan	Satuma	Flamingo	Completed	Ground launched	Reciprocating	Fixed Wing	8	200	4267	45	245	35	130		7.32
Russia	Enics	E08	Under way	Catapult launched	Pulse Jet	Canard	0.5	70	3000	59	150		300	200	5
		E95M	Under way	Catapult launched	Pulse Jet	Fixed Wing	0.5	187	3000	59	75		300	200	2.9
	Kamov	Ka-137	Under way	Ground and ship launched	Reciprocating	VTOL	4	530	5000	50	280	80	175	145	5.3
Serbia	Military Technical Institute	Pegaz 101	In Development	Ground launched	Reciprocating	Fixed Wing	12	100	3000	32	230	40	200	150	6.34
Spain	INTA	Siva	Under way				6.5	150	4000	50	300	49	190	115	5.8
Sweden	CybAero	APID 55	Under way		Reciprocating	VTOL	6	50	3000	41	160	55	90	60	3.3
		Vantage	Under way		Reciprocating	VTOL	5		2400	31	173	16	185		2.77
	Saab defense	Skeldar V-200	In production			VTOL	5	150	4500	41	200	40	130		
Turkey	Turkish Aerospace Industries	Karayel	In production		Reciprocating	Fixed Wing	20		6858	52	500	70		148	10.5
UAE	ADCOM Military Industries	Yabhon RX	Under way	Catapult launched	Reciprocating	Fixed Wing	6		5500	37	160	50	240	204	5.8
		Yabhon-N	Under way	Catapult launched	Reciprocating	Flying Wing	3		6000	37	100	40	420	107	2.75
UK	Warrior (Aero-Marine Ltd.)	GULL 68 UXV	Under way	Ground or water launched	Reciprocating	Seaplane		2081		33	250	94	185		7.6
US	AAI	Shadow 600	completed		Reciprocating	Fixed Wing	14	322	1487	39	265	41	200	148	6.8
	Atair	LEAPP Type II	Under way	Ground launched	Reciprocating	Paraglider	34		5182	41	544	91			34
	Elbit Systems of America	Hermes 450	Deployed	Ground launched	Reciprocating	Fixed Wing	18	300	5486	39	550	180	176	130	10.5
	General Atomics Aeronautical Systems	I-GNAT ER/Sky Warrior	Deployed		Reciprocating	MALE	40	250	7620	48	520	91	192		10.75

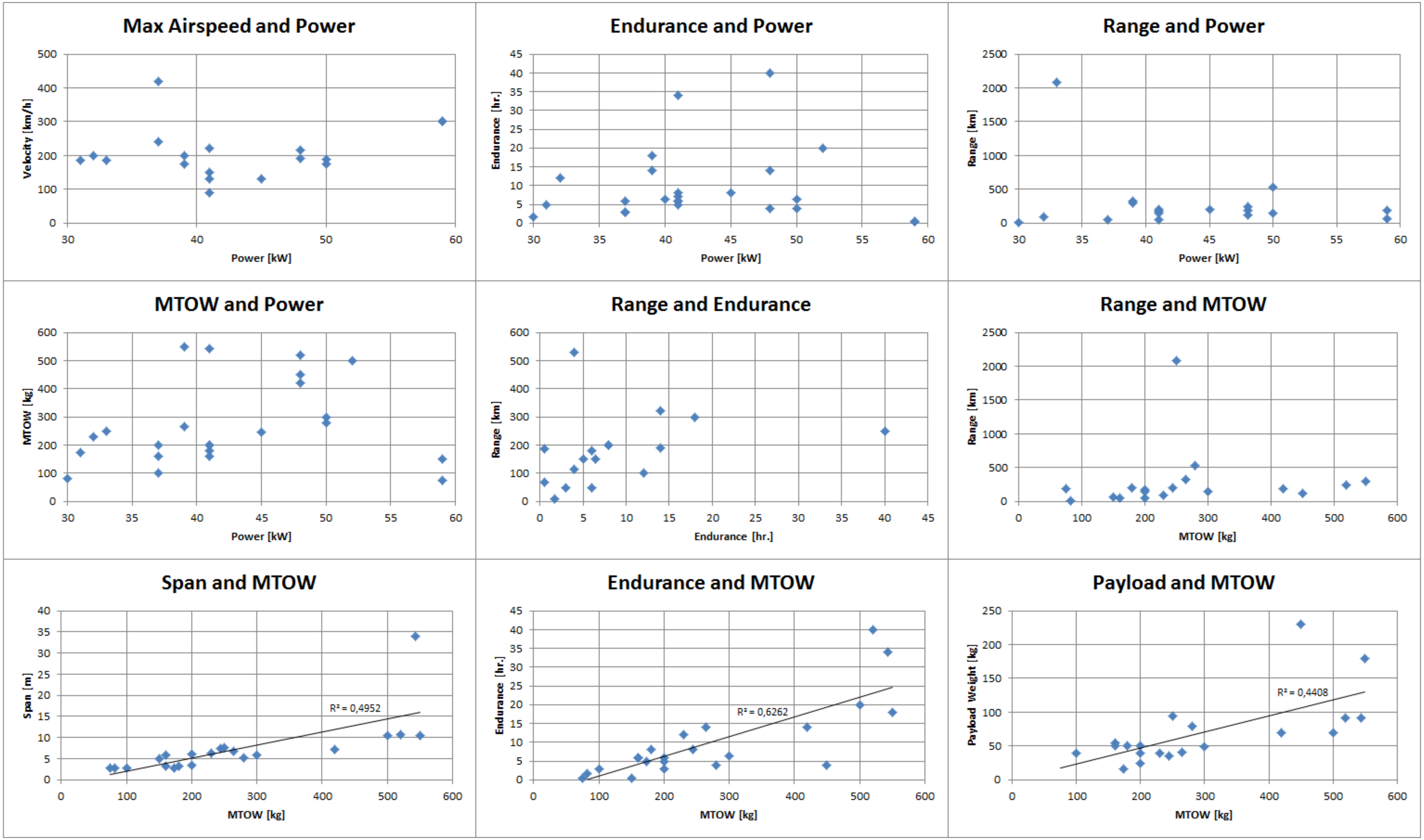
Max Airspeed and Power
Velocity [km/h]
Power [kW]
Endurance and Power
Endurance [hr.]
Power [kW]
Range and Power
Range [km]
Power [kW]
MTOW and Power
MTOW [kg]
Power [kW]
Range and Endurance
Range [km]
Endurance [hr.]
Range and MTOW
Range [km]
MTOW [kg]
Span and MTOW
Span [m]
R² = 0,4952
MTOW [kg]
Endurance and MTOW
Endurance [hr.]
R² = 0,6262
MTOW [kg]
Payload and MTOW
Payload Weight [kg]
R² = 0,4408
MTOW [kg]

E. C.G. Calculator Input

The required input for the C.G. calculation of the UAV is given in Table E-1.

$$K_{no} = 1 + \sqrt{\frac{b_{ref} \cdot \cos \Lambda_{1/2}}{b}}$$

Table E-1: C.G. Calculator Input

Parameter	Value	Description
n_{ult}	3.8	Ultimate load factor (light aircraft) [g]
M	0.18	Mach number (speed of sound = 340 m/s) [-]
V_{Des}	56.6	Design dive speed [m/s]
$V_{Eq,max}$	73.83	Equivalent velocity [kts]
ρ_{crz}	0.549	Density at cruise altitude (7620 ft) [kg/m³]
$W_{Wing,Guess}$	200	First guess of wing weight [kg]
$W_{Carried,Fus}$	300	Weight of fuel in wing [kg]
WA_{Emp}	2.44	Aerial weight of empennage [kg/m²]
b_{ref}	1.905	Reference span (fixed value from Torenbeek (6.25ft)) [m]
F_{MG}	1	Main gear on fuselage factor (1 = not on fuselage, 1.07 = on fuselage) [-]
F_{NG}	1.04	Nose gear on fuselage factor (1 = not on fuselage, 1.04 = on fuselage) [-]
F_{Press}	1	Pressurization factor (1 = unpressurized, 1.078 = pressurized) [-]
F_{VT}	1	Vertical tail on fuselage (1 = not on fuselage, 1.1 on fuselage) [-]
F_{Matl}	1	Material factor (1 = carbon fiber, 2 = fiberglass, 1 = metal, 2.187 = wood, 2 = unknown) [-]
K_{Inlet}	1.2	Air intake parameter (1 = nose intake, 1.05 = abdomen intake, 1.2 = back intake, 1.3 both side intake) [-]
K_{dwf}	1	Delta wing factor (1 = non delta wings) [-]
K_{Eng}	1	Engine index for wing mass estimation (0.95 = twin engine, 1 = else) [-]
K_{uc}	1	Landing gear index for wing mass estimation (0.95 = no LG in wing, 1 = LG at wing) [-]
K_{ST}	1	Stiffness factor adding extra weight for high subsonic A/C (1 = low subsonic A/C) [-]
K_b	1	Cantilever wing factor [-]
K_{HT}	1	Horizontal tail weight estimation (1 = fixed HT, 1.1 = all moving HT) [-]
F_{LG}	0.04	Landing gear mass fraction [-]
$F_{Fuel,Sys}$	0.692	Fuel system multiplication factor for MALE single engine [-]
$\#_{Eng}$	1	Number of engines

F. Tornado Input

Harfang EADS

Number of Wings	4	*Main wing, horizontal stabilizer and two vertical stabilizers*
Data regarding wing number 1	*Main wing*	
Semispanwise partitions for this wing	3	*Straight part, swept flap part, swept aileron part*
Data regarding partition number 1	*Straight part*	
Center of gravity x-coordinate	0.1107	
Center of gravity y-coordinate	0	*C.G. Measured from wing leading edge*
Center of gravity z-coordinate	0.074217	
Reference point x-coordinate	0	
Reference point y-coordinate	0	*System origin (at leading of c_r of main wing)*
Reference point z-coordinate	0	
Is the wing mirrored in the xz-plane	1	
Root chord	1	
Base chord airfoil	N641443.dat	*NACA 6414-43*
Number of panels chord wise	5	
Partition dihedral	0	
Number of panels semi-span wise	3	
Span of partition	1.55	
Taper ratio	1	
Tip chord airfoil	N641443.dat	*NACA 6414-43*
Quarter chord line sweep	0	
Outboard twist	0	
Mesh type	3	*Spanwise half cosine, chordwise half cosine*
Is partition flapped	1	*Trailing edge flap*
Flap chord in faction of local chord	0.18	
Number of chord wise panels on flap	2	
Do control surfaces deflect symmetrically	1	
Data regarding partition number 2	*Swept flap part*	
Partition dihedral	0	
Number of panels semi-span wise	6	
Span of partition	3.375	
Taper ratio	0.55	
Tip chord airfoil	N641443.dat	*NACA 6414-43*
Quarter chord sweep	1	
Outboard twist	0	
Mesh type	3	*Spanwise half cosine, chordwise half cosine*
Partition flapped	1	*Trailing edge flap*
Flapped chord in fraction of local chord	0.18	
Number of chord wise panels on flap	2	
Do control surfaces deflect symmetrically	1	
Data regarding partition number 3	*Swept aileron part*	
Partition dihedral	0	
Number of panels semi-span wise	6	
Span of partition	3.375	
Taper ratio	0.55	
Tip chord airfoil	N641443.dat	*NACA 6414-43*
Quarter chord sweep	1	
Outboard twist	0	
Mesh type	3	*Spanwise half cosine, chordwise half cosine*
Partition flapped	0	
Data regarding wing number 2	*Horizontal stabilizer*	
Number of semispanwise partitions of this wing	1	
Is the wing mirrored in the xz-plane	1	
Apex x-coordinate	4.56	*Aft of the reference point*
Apex y-coordinate	0	
Apex z-coordinate	0	

Root chord	0.73	
Base chord airfoil	naca0012.dat	*NACA 0012 (standard stabilizer airfoil)*
Number of panels chord wise	4	
Base chord twist	0	
Partition dihedral	0	
Number of panels semi-span wise	3	
Span of partition	1.55	
Taper ratio	1	
Tip chord airfoil	naca0012.dat	*NACA 0012 (standard stabilizer airfoil)*
Quarter chord line sweep	0	
Outboard twist	0	
Mesh type	3	*Spanwise half cosine, chordwise half cosine*
Is partition flapped	0	
Data regarding number 3	*Vertical stabilizer (Left)*	
Number of semispanwise partitions for this wing	1	
Is the wing mirrored in the xz-plane	0	
Apex x-coordinate	4.41	Aft of reference point: $4.57 - (tan\, 25 \cdot 0.36) = 4.41$ *(leading edge rudder equal to leading edge elevator)*
Apex y-coordinate	-1.55	*Left of the reference point (top view)*
Apex z-coordinate	-0.36	*Down of the reference point*
Root chord	0.91	
Base chord airfoil	naca0012.dat	*NACA 0012 (standard stabilizer airfoil)*
Number of panels chord wise	4	
Base chord twist	0	
Partition dihedral	75	*Toe-in*
Number of panels semi-span wise	3	
Span of partition	1.82	
Taper ratio	0.51	
Tip chord airfoil	naca0012.dat	*NACA 0012 (standard stabilizer airfoil)*
Quarter chord line sweep	25	
Outboard twist	0	
Mesh type	3	*Spanwise half cosine, chordwise half cosine*
Is partition flapped	0	
Data regarding wing number 4	*Vertical stabilizer (Right)*	
Number of semispanwise partitions for this wing	1	
Is the wing mirrored in the xz-plane	0	
Apex x-coordinate	4.41	Aft of reference point: $4.57 - (tan\, 25 \cdot 0.36) = 4.41$ *(leading edge rudder equal to leading edge elevator)*
Apex y-coordinate	1.55	*Right of the reference point (top view)*
Apex z-coordinate	-0.36	*Down of the reference point*
Root chord	0.91	
Base chord airfoil	naca0012.dat	*NACA 0012 (standard stabilizer airfoil)*
Number of panels chord wise	4	
Base chord twist	0	
Partition dihedral	105	*Toe -in*
Number of panels semi-span wise	3	
Span of partition	1.82	
Taper ratio	0.51	
Tip chord airfoil	naca0012.dat	*NACA 0012 (standard stabilizer airfoil)*
Quarter chord line sweep	25	
Outboard twist	0	
Mesh type	3	*Spanwise half cosine, chordwise half cosine*
Is partition flapped	0	

G. Flowcharts Mission Simulation

Different Matlab scripts are developed to simulate the mission performance. Flowcharts of each script are provided in Figure G-1 through Figure G-8. Please note that the descent and approach phase are modeled using the same Matlab script.

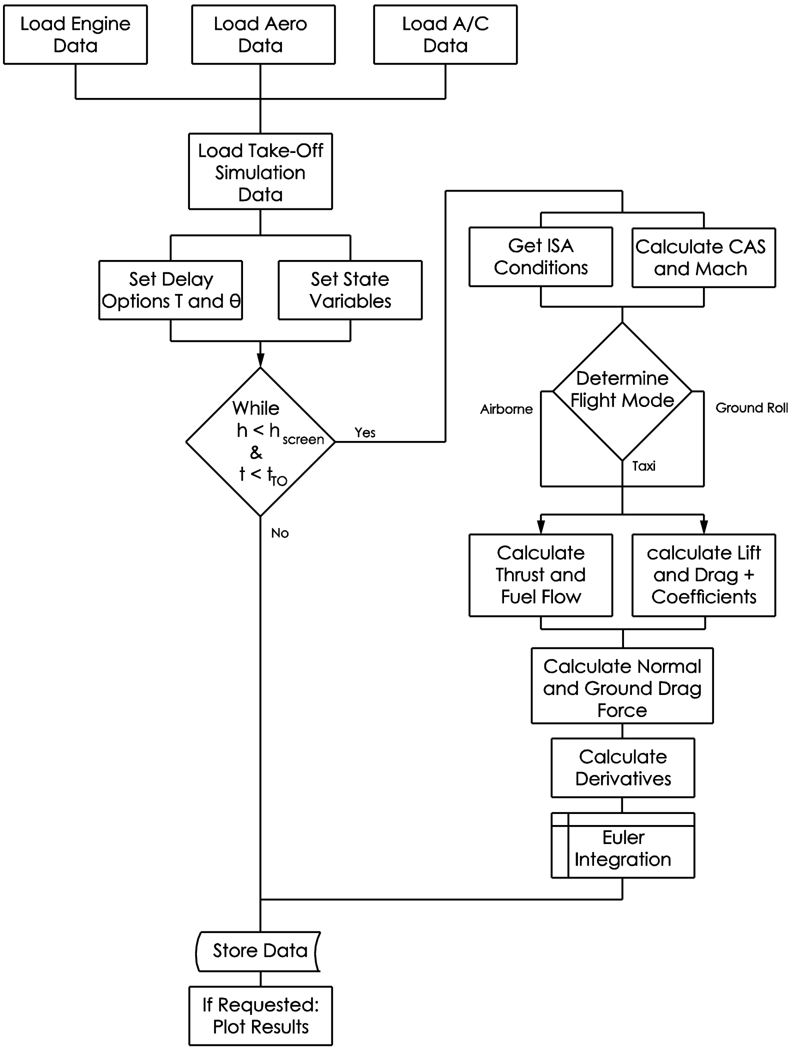

Figure G-1: Flowchart of Matlab Script to Model Take-Off Phase

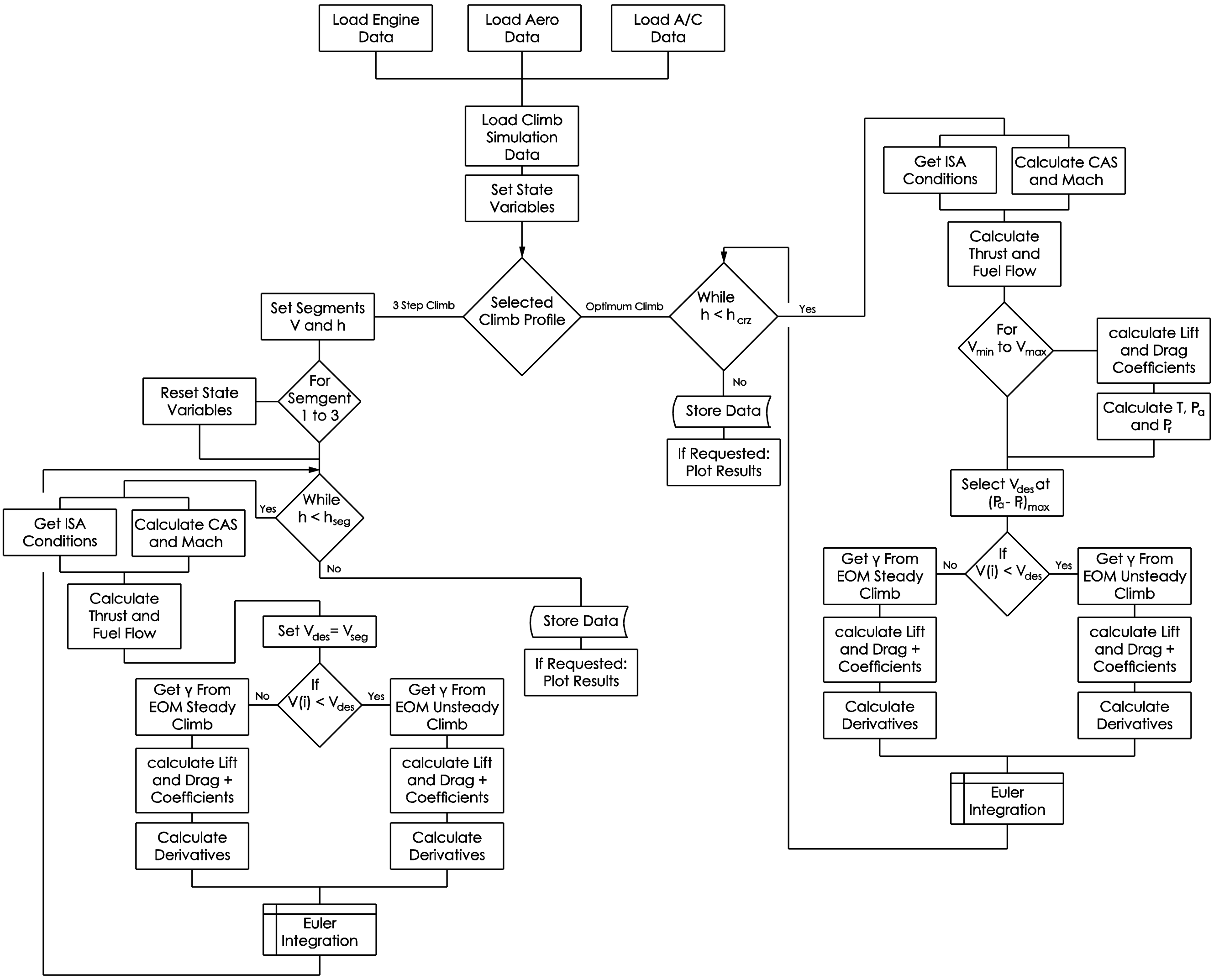

Figure G-2: Flowchart of Matlab script to Model Climb Phase

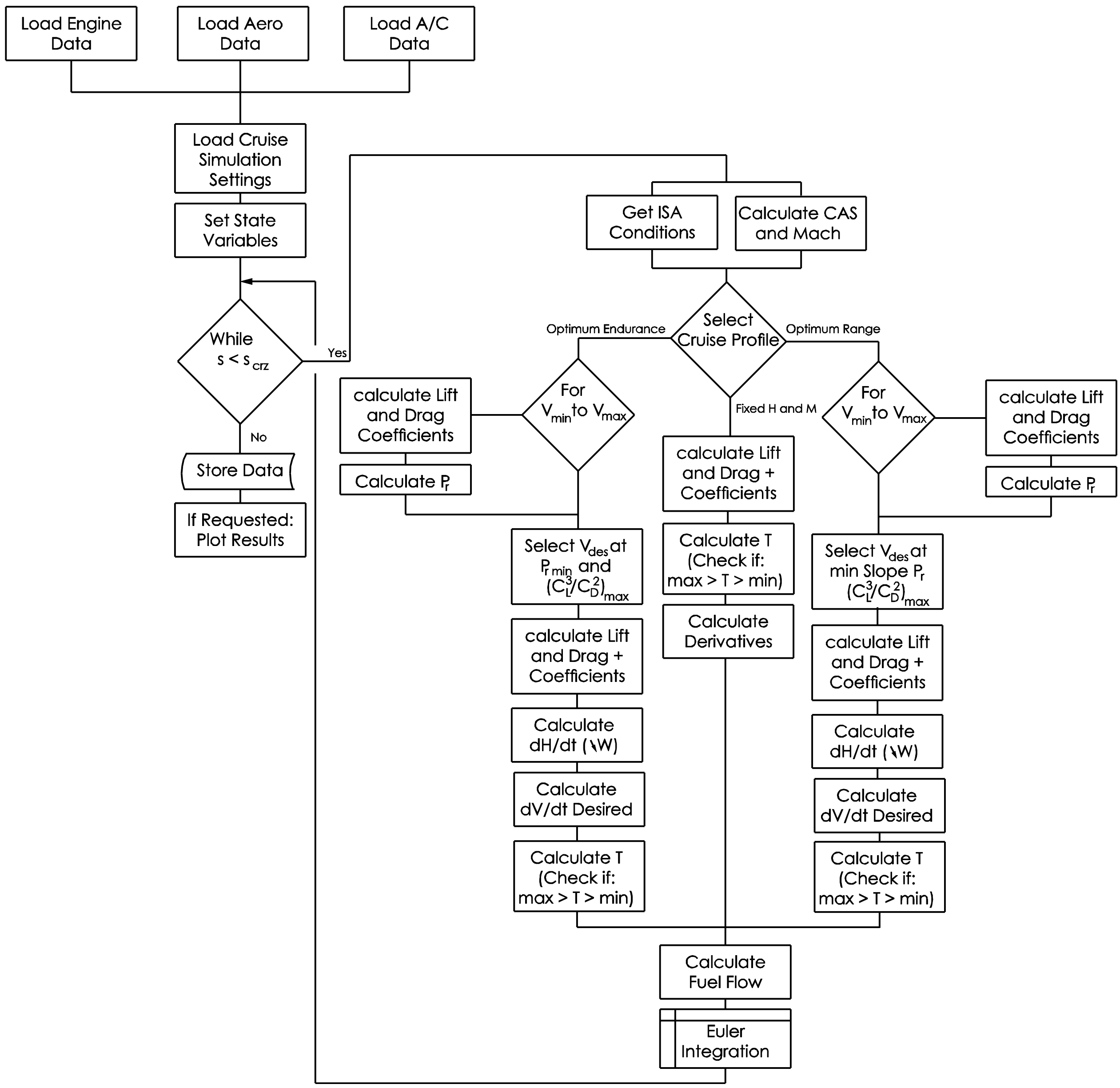

Figure G-3: Flowchart of Matlab Script to Model Cruise Phase

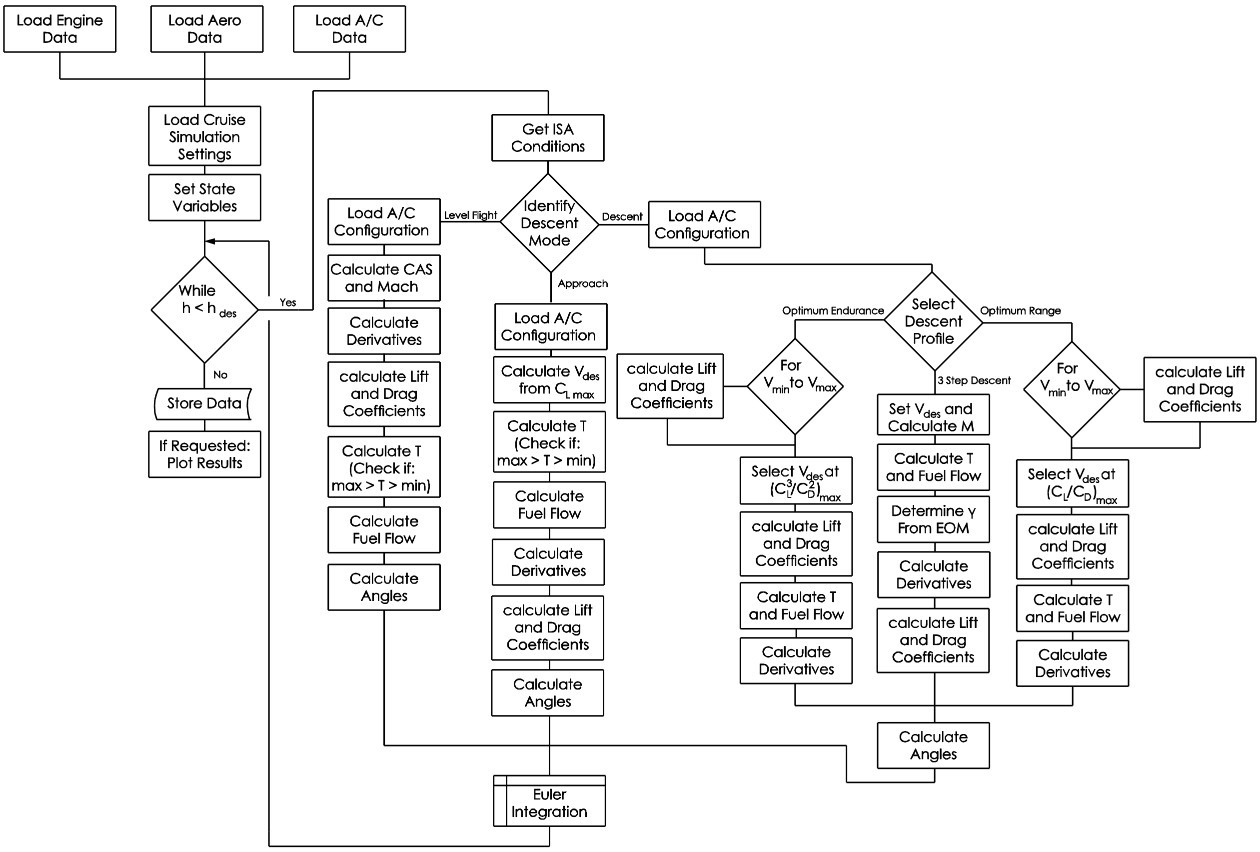

Figure G-4: Flowchart of Matlab Script to Model Descent and Approach Phase

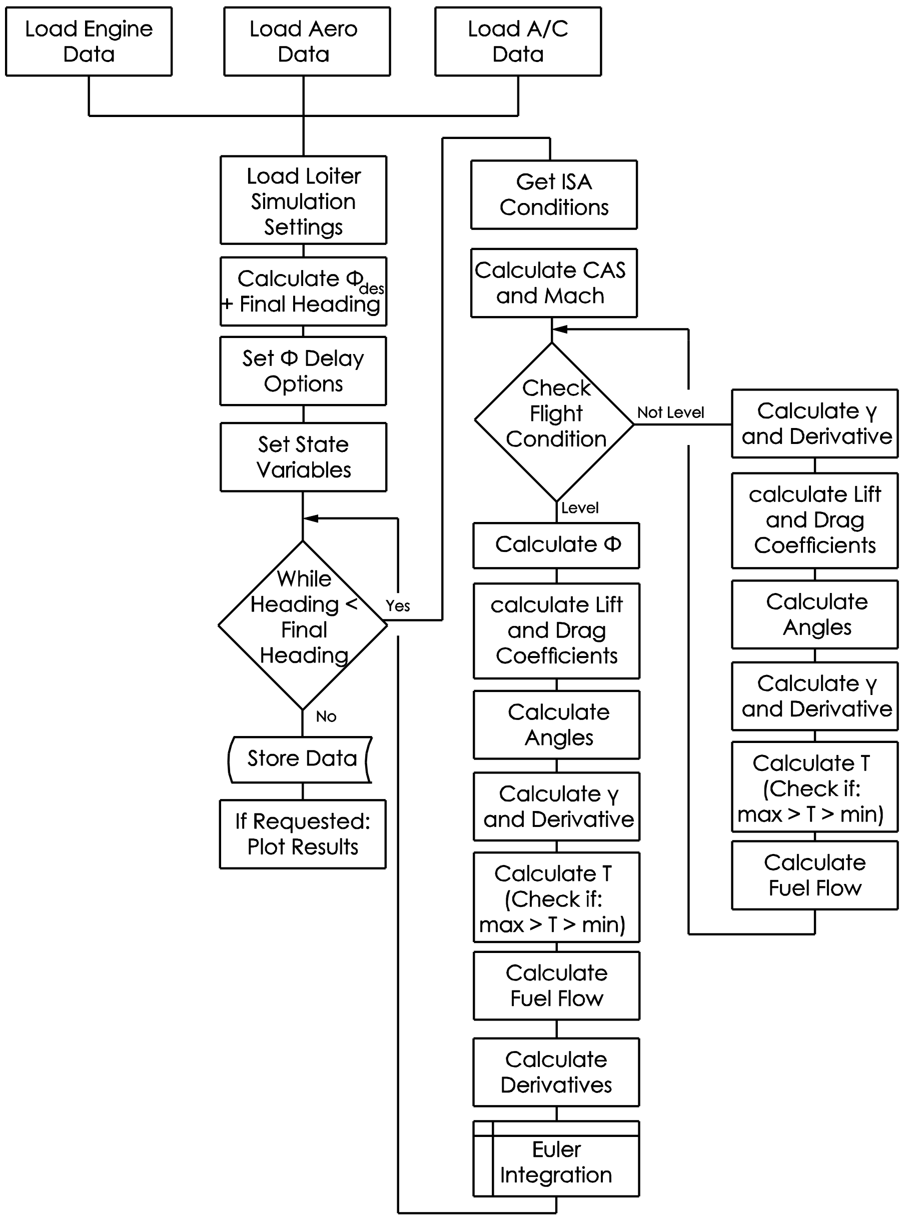

Figure G-5: Flowchart of Matlab Script to Model Loiter Phase

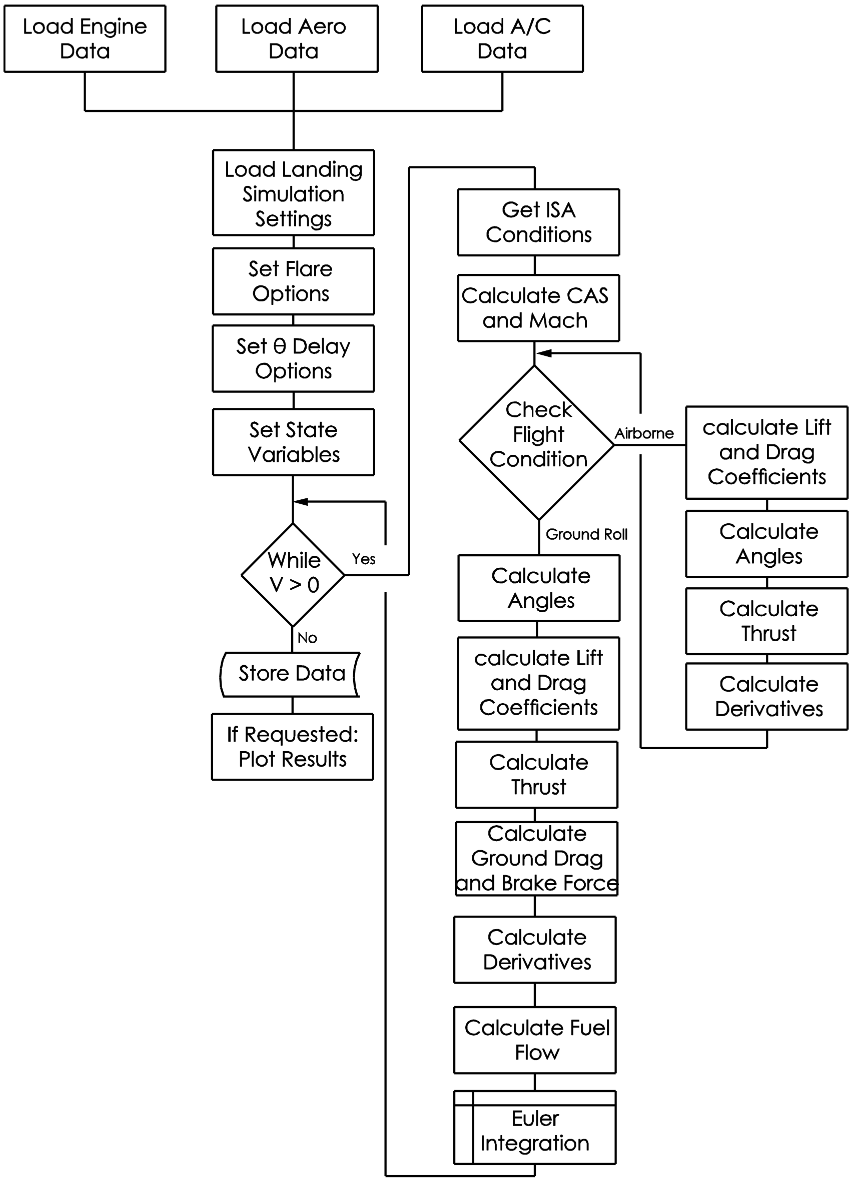

Figure G-6: Flowchart of Matlab Script to Model Landing Phase

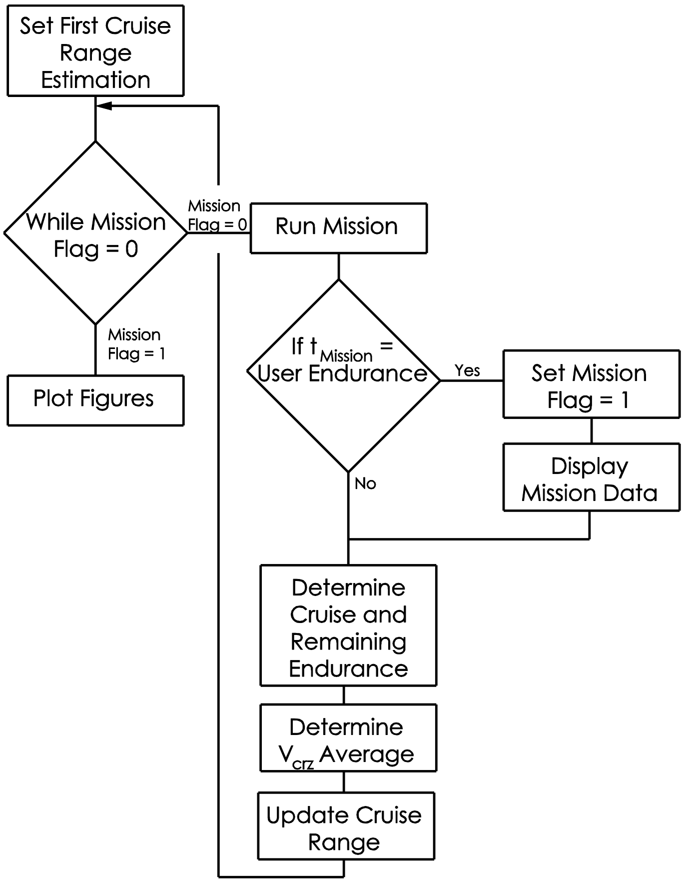

Figure G-7:Flowchart of Matlab Script to Model Fixed Endurance Mission

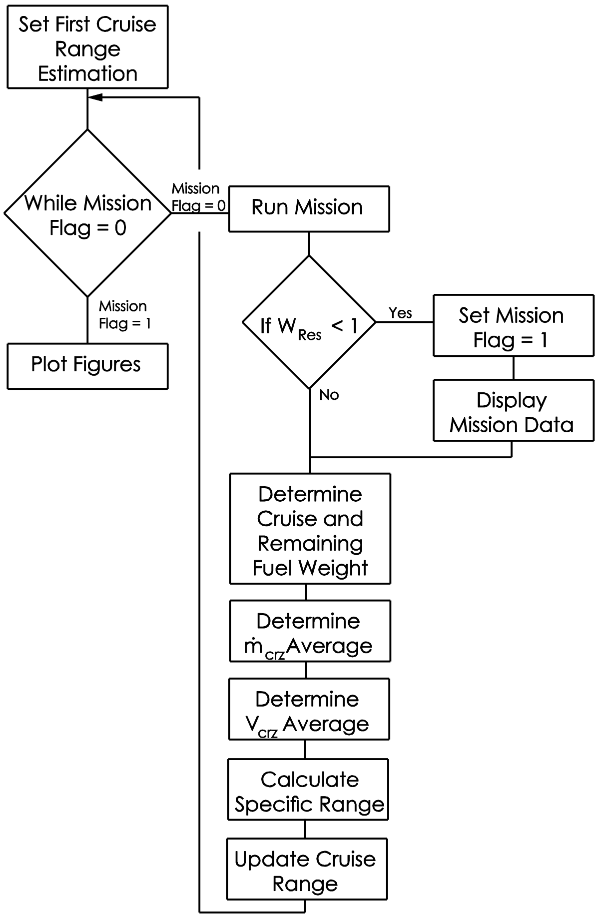

Figure G-8: Flowchart of Matlab Script to Model Fixed Fuel Use Mission

H. Weight Breakdown Analysis MGT

Table H-1: Results of Components WERs MGT

	MGT Size [kW]	Wing	Fuselage	Horizontal Tail	Vertical Tails	Booms	Landing Gear	Fuel System	Avionics
	86	252.02							
Gerard	70	250.91							
	60	250.03							
	86	154.78		~~21.57~~					114.89
Torenbeek	70	154.25		~~21.40~~					114.49
	60	153.83		~~21.26~~					114.17
	86	351.95	81.76				64.09		133.02
Yi	70	350.73	81.44				63.87		132.47
	60	349.75	81.18				63.69		132.03
	86		~~186740~~			23.48	48.37	26.635	
Gundlach	70		~~186740~~			23.47	48.17	26.635	
	60		~~186740~~			23.461	48.01	26.635	
	86		~~1157.2~~						
Raymer (Fighter attack)	70		~~1155.6~~						
	60		~~1154.2~~						
	86		15.44	3.39					
Raymer (GA)	70		15.43	3.38					
	60		15.42	3.38					
	86		32.37	4.57	7.35				
Howe (Single Engine)	70		32.37	4.57	7.35				
	60		32.37	4.56	7.35				
	86			5.52	6.08				
Palumbo	70			5.52	6.08				
	60			5.52	6.08				
	86			~~11.61~~					~~23.81~~
Roskam	70			~~11.61~~					~~23.75~~
	60			~~11.61~~					~~23.70~~
	86				~~22.66~~				
Nicolai/Anderson	70				~~22.63~~				
	60				~~22.60~~				
	86	252.91	43.19	4.49	6.72	23.48	56.23	26.64	123.96
Average	70	251.96	43.08	4.49	6.72	23.47	56.02	26.64	123.48
	60	251.20	42.99	4.49	6.72	23.46	56.85	26.64	123.10
	86	351.95	81.76	5.52	7.35	23.48	64.09	26.64	133.02
Maximum	70	350.73	81.44	5.52	7.35	23.47	63.87	26.64	132.47
	60	349.75	81.18	5.52	7.35	23.46	63.69	26.64	132.03
	86	154.78	15.44	6.08	6.08	23.48	48.37	26.64	114.89
Minimum	70	154.25	15.43	6.08	6.08	23.47	48.17	26.64	114.49
	60	153.83	15.42	6.08	6.08	23.46	48.01	26.64	114.17

I. Results Redesign Loops

Table I-1: Final Results of Weight Breakdown Analysis of First Redesign Loop

	Wing	Fuselage	Horizontal Tail	Vertical Tail	Booms	Landing Gear	Fuel System	Avionics
Gerard	216.52							
Torenbeek	128.7		~~17.56~~					104.85
Yi	299.76	68.36				58.46		
Gundlach		~~147260~~			16.51	43.35	26.06	119.22
Raymer (Fighter attack)		~~1001.5~~						
Raymer (GA)		13.77	2.68					
Howe (Single Engine)		27.61	4.31	5.15				
Palumbo			4.73	4.63				
Roskam			~~8.91~~					~~22.28~~
Nicolai/Anderson				~~18.69~~				
Average = 1081.8 kg	214.99	36.58	3.82	4.89	16.51	50.91	26.06	112.03

Table I-2: Final Results Weight Breakdown Analysis of Second Redesign Loop

	Wing	Fuselage	Horizontal Tail	Vertical Tail	Booms	Landing Gear	Fuel System	Avionics
Gerard	205.79							
Torenbeek	123.21		~~16.54~~					101.55
Yi	284.79	65.05				56.58		
Gundlach		**~~146260~~**			**15.57**	**41.70**	**24.94**	**114.68**
Raymer (Fighter attack)		~~970.31~~						
Raymer (GA)		13.45	2.54					
Howe (Single Engine)		26.87	4.25	4.89				
Palumbo			4.30	4.45				
Roskam			~~8.47~~					~~21.78~~
Nicolai/Anderson				~~18.00~~				
Average = 1040.9 kg	204.6	35.12	3.70	4.67	15.57	49.14	24.94	108.12

Table I-3: Final Results Weight Breakdown Analysis of Third Redesign Loop

	Wing	Fuselage	Horizontal Tail	Vertical Tail	Booms	Landing Gear	Fuel System	Avionics
Gerard	201.68							
Torenbeek	121.09		~~16.58~~					100.27
Yi	279.06	63.78				55.86		
Gundlach		~~145860~~			15.21	41.07	24.51	112.93
Raymer (Fighter attack)		~~958.19~~						
Raymer (GA)		13.32	2.49					
Howe (Single Engine)		26.58	4.22	4.79				
Palumbo			4.23	4.38				
Roskam			~~8.30~~					~~21.584~~
Nicolai/Anderson				~~17.74~~				
Average = 1025.2 kg	200.61	34.56	3.65	4.58	15.21	48.46	24.51	106.6

Table I-4: Final Results Weight Breakdown Analysis of Fourth Redesign Loop

	Wing	Fuselage	Horizontal Tail	Vertical Tail	Booms	Landing Gear	Fuel System	Avionics
Gerard	200.3							
Torenbeek	120.41		~~16.49~~					99.84
Yi	277.13	63.35				55.61		
Gundlach		~~145720~~			15.09	40.85	24.35	112.34
Raymer (Fighter attack)		~~954.09~~						
Raymer (GA)		13.28	2.47					
Howe (Single Engine)		26.48	4.21	4.75				
Palumbo			4.21	4.36				
Roskam			~~8.25~~					~~21.52~~
Nicolai/Anderson				~~17.65~~				
Average = 1019.6 kg	199.28	34.37	3.63	4.55	15.09	48.23	24.35	106.09